Elastic and Inelastic X-ray scattering studies of the low dimensional spin-1/2 quantum magnet TiOCl

by

Eric T. Abel

Submitted to the Department of Physics
in partial fulfillment of the requirements for the degree of

Doctor of Philosophy

at the

MASSACHUSETTS INSTITUTE OF TECHNOLOGY

May 2007

Author ....
Department of Physics
April 9, 2007

Certified by............................ ....
Young S. Lee
Associate Professor
Thesis Supervisor

Accepted by.............................. ....
Thomas J. Greytak
Chairman, Department Committee on Graduate Students

Elastic and Inelastic X-ray scattering studies of the low dimensional spin-1/2 quantum magnet TiOCl

by

Eric T. Abel

Submitted to the Department of Physics
on April 9, 2007, in partial fulfillment of the
requirements for the degree of
Doctor of Philosophy

Abstract

The ground state for a one dimensional spin 1/2 Heisenberg chain coupled to phonons is a dimerized singlet state known as a "spin-Peierls" state. Currently, the spin-Peierls state is realized in only a handful of known compounds. Even after decades of scientific scrutiny, there is an absence of direct measurements of the lattice dynamics associated with the transition.

In this work we present an extensive study of a new one dimensional spin-Peierls compound, TiOCl. The magnetic susceptibility strongly indicates a singlet ground state, with two apparent anomalies observed at T_{c_1}=65 K and T_{c_2}=92 K. Specific heat measurements have been performed and the associated entropy changes quantified. The 65 K transition exhibits a thermal hysteresis, indicative of a first order phase transition. A detailed synchrotron x-ray study of the structure reveals the appearance of superlattice peaks at (H,K±1/2,L) below 65 K. The intensity of the peaks drop very sharply above T_{c_1}, and a thermal hysteresis is observed which is consistent with a first order phase transition at 65 K. We find that the temperature region between 65 K and 92 K is characterized by a novel incommensurate state. The incommensurate reflections appear at $(\pm\Delta H, K + 1/2 \pm \Delta K, L)$. The temperature dependence of the intensity of the incommensurate peaks shows a more gradual onset, with no thermal hysteresis. The incommensurate wavevectors change continuously as a function of temperature and can be analyzed in terms of a mean field theory of phase shifted discommensurations. The observation of the third harmonics enabled a careful characterization of the underlying real space superstructure. We find that all of the observed scattering can be reproduced by a one dimensional long-wavelength modulation of a locally dimerized structure.

The lattice dynamics above T_{c_2}were characterized by inelastic x-ray scattering measurements. By analyzing the data in terms of a damped harmonic oscillator response function, we are able to extract the phonon frequency and damping for all observed modes. We find a longitudinal acoustic phonon branch whose damping increases for q-vectors close to the zone boundary, which is also associated with an apparent softening of the frequency. Both of these anharmonic effects increase as $T_{c_2}$is approached, and are consistent with a soft phonon description of the dimerization. The anomalous phonon damping and softening are then analyzed using the Cross & Fisher theory of spin-phonon interaction leading to a spin-Peierls transition. We find that the theory succeeds in describing the data for a narrow temperature range about T_{c2}, for q near the zone boundary. It does not account for the anharmonic effects observed at high temperatures. Our experimental analysis represents one of the most in-depth quantitative tests of the Cross & Fisher theory to date. In addition our results suggest that TiOCl is a particularly ideal realization of a spin-Peierls system.

Thesis Supervisor: Young S. Lee
Title: Associate Professor

Acknowledgments

Over the course of my Ph.D. thesis I have encountered numerous people who have helped me in some form or another. Whether it be understanding a concept in a problem set, or bouncing ideas off of them for analysis of my data, the input of these people has been invaluable. While there were countless others, I would especially like to highlight: Sami Amasha, Richard Ott, Kittiwit Matan, Joel Helton, Goran Gasparovic, Kenneth McClean and Pouyan Ghaemi. I must separate these people from those who were responsible for not only keeping the instruments up and running, but also provided valuable insight and guidance during the course of an experiment at the X-ray synchrotron. At the NSLS, John Hill was always available for help at any time of the day, and would even take time away from his family on weekends to come in and make sure all was going well. To this I must also add Ahmet Alatas and Harald Sinn of sector 3 at APS. Harald had a vast knowledge of inelastic x-ray scattering, which I tapped to run my experiment, and Ahmet would come in the middle of the night to insure that the beam hadn't dumped, keeping the experiment on track.

These are all people who helped me get through my Ph.D. scientifically, which is important, but now I would like to take a little time to acknowledge those who really got me through my five years here at M.I.T. First of all, I found a friend in the CMSE crystal lab scientist Fangcheng Chou, who not only taught me everything I know about crystal growth, but also had a knack for putting everything in perspective for me, clarifying many seemingly cloudy decisions. Anyone who knows will tell you that this degree was an uphill struggle for me personally from day one. Fang was one of those who helped carry me through some of the rough times.

I also must add my parents to the list of people who provided moral support through some of the difficult times I encountered over the course of my Ph.D.

Of course, I am forever indebted to my thesis advisor, Young Lee, who not only gave me the chance to come to M.I.T., but also gave me the means to stay by letting me leave. No this is not a contradiction...because my wife, Lien was unable to stay

in Boston, I nearly settled for a Master's Degree to follow her to Oregon, but Young presented me with an alternative which would allow me to acquire a Ph.D. without being 3000 miles from my family. Lien and I are equally grateful that Young was generous enough to give me this opportunity.

This brings me to my wife Lien who not only endured two years of separation while I was in Germany for my Master's, but she also waited patiently for 3 years while I finished up my academics at M.I.T., nine months of which she was pregnant with our son Kiyan. Upon returning to Oregon, Lien was very patient caring for Kiyan while I spent long hours both night and day working on my thesis. At this point I must also acknowledge Lien's sisters and especially her mother for all of the help they provided caring for the children so that I could work on my thesis. In addition, they would care for the children when I would leave town to go to M.I.T. or one of the national labs. I can honestly say that if it weren't for them, I would not have a completed thesis at this time.

Finally, I wanted to acknowledge my son Kiyan and daughter Quinlyn. Kiyan is two and Quinlyn is five months, and both of them have had to compromise time with their daddy because of this thesis. That is perhaps the most difficult aspect of my Ph.D. But now, I've made it, and I will have more time to spend with you and your mommy. Lien, Kiyan, Quinlyn, I dedicate this thesis to all of you, and want you to know that you to know how much it means to me that you supported me through the entire process.

Eric Abel

Contents

1 Introduction and Motivation **25**

1.1 Spin-Peierls basics . . . 29

1.1.1 1D Spin Chains . . . 30

1.1.2 Spin-Peierls Gap . . . 32

1.2 Experimental Realization of the Spin-Peierls State . . . 33

1.3 $CuGeO_3$ As a Spin-Peierls System . . . 34

1.4 TiOCl, A Promising New Spin-Peierls Candidate . . . 36

1.5 Thesis Overview . . . 39

2 Experimental Details **41**

2.1 X-ray Sources . . . 41

2.1.1 History Of X-ray Sources . . . 41

2.1.2 Classical Theory of Synchrotron Radiation . . . 42

2.1.3 Bending Magnets . . . 48

2.1.4 Insertion Devices . . . 51

2.2 Beam Line Components . . . 53

2.2.1 Monochromator . . . 55

2.2.2 Beam Focusing . . . 56

2.2.3 Single Crystal Diffractometer . . . 58

2.2.4 X-ray Detectors . . . 60

2.3 Single Crystal Diffraction . . . 61

2.3.1 Reciprocal Space . . . 62

2.3.2 Atomic Form Factor . . . 64

2.3.3 Bravais and General Lattice 66
2.4 X-ray Scattering Intensity 68
2.4.1 Polarization Factor 68
2.4.2 Lorentz Factor 70
2.4.3 Debye Waller Factor 71
2.4.4 Crystal Mosaic 73
2.4.5 Absorption 73
2.4.6 Multiple Scattering 74
2.4.7 Summary 76
2.5 X-ray Powder Diffraction 77
2.6 Inelastic X-ray Scattering 80
2.7 SQUID Magnetometer 83
2.8 Heat Capacity 86

3 Spin-Peierls in TiOCl **89**
3.1 Sample Growth and Characterization 89
3.1.1 Powder Samples 89
3.1.2 Single Crystal Samples 94
3.1.3 Optimization of Vapor Transport Growth 97
3.1.4 Crystal Growth the “Hard Way” 99
3.2 Thermodynamic Characterization 102
3.3 Study of Low Temperature Distortions using Elastic X-ray Scattering 106
3.3.1 Lattice Distortions and Superstructures 107
3.3.2 Commensurate Superlattice Peaks 118
3.3.3 Incommensurate Superlattice Peaks 121
3.3.4 Modelling of the Incommensurate Modulation 126
3.3.5 Harmonics 130
3.4 Inelastic X-ray Study of the Lattice Dynamics 135
3.4.1 Basic Concepts of Lattice Vibrations 135
3.4.2 Lattice Dynamical Calculations in the Harmonic Approximation 143

3.4.3 Structural Phase Transitions 147

3.4.4 Cross-Fisher Polarizability 152

3.4.5 Lattice Dynamics in TiOCl 154

3.4.6 Spin-Phonon Coupling in TiOCl 167

3.5 Conclusions 173

List of Figures

1-1 Cubic lattice with ferromagnetic (a) and antiferromagnetic (b) spin order. 26

1-2 Spins on a lattice can lower their energy by pairing up into singlets. This results in a chain of dimerized atoms. 29

1-3 a) A 1-D AF chain with a $\Delta S = 1$ excitation. The red lines indicate domain walls, which can be separated by any arbitrary distance with no energy cost. b) Numerically calculated spinon continuum with 256 k-points following the numerical recipe in [1][2]. c) Spinon continuum observed in $SrCuO_3$ with neutrons [3]. 30

1-4 a) TiOCl crystal structure with unit cell. b) Ti^{3+} octahedron formed with 4 O^{2-} and 2 Cl^- ions. The octahedral z-axis is aligned parallel to a, with the x,y axes rotated 45^o from a,b axes. c) Projection of Ti^{3+} buckle square lattice projected onto the a-b plane. The Ti^{3+} t_{2g} orbitals drawn are the ones which form the 1-D chains along the b-direction. 37

1-5 Illustration of the d-orbital electron density distribution, shown along with an octahedral $TiCl_6$ molecule for orientation reference. The energy diagram on the right shows the splitting of the degenerate d-levels in an octahedral environment into t_{2g} and e_g. 38

2-1 Geometry for potential of a charge moving along arbitrary trajectory at velocity v. 43

2-2 Angular distribution of power radiated from a charge moving perpendicular to the acceleration in the rest frame (a) and in the moving frame (b). 45

2-3 Shape of x-ray brilliance as a function of the frequency scaled by the characteristic synchrotron frequency ω_c. The exact numerical expression is [35] $1.327 \times 10^{13} x^2 K^2_{2/3}(x/2)$, where $K^2_{2/3}$ is a modified Bessel Function of the second kind. 48

2-4 Schematic of a storage ring bending magnet. The "ring" actually consists of straight sections connected by bent sections where the bending magnets are located. The tangential tubes guide the radiated x-rays to the experimental setup. 49

2-5 Schematic of the electron path and radiated power in a wiggler (a) and an undulator (b). In an undulator the oscillations are smaller thus more of the radiation cones overlap resulting in a narrower divergence of the forward radiation. The arrows indicate the magnet polarity. . . 50

2-6 Plot comparing the brilliance curves from various sources. Bending magnets are clearly labeled, and undulator sources are labeled with Uλ_u (taken from [38]). 52

2-7 Schematic diagram showing the important components of a typical synchrotron single crystal x-ray diffraction experiment. 54

2-8 Diagram showing the refraction of x-rays passing from air with refractive index, $n = 1$, into a metal with $n < 1$. 57

2-9 Typical synchrotron x-ray scattering diffractometer. 59

2-10 Schematic of Bragg scattering in a periodic array of atoms. 61

2-11 Diagram showing x-rays incident on two atoms separated by $\vec{R}$. . . . 62

2-12 Cromer-Mann atomic form factor $f^0(Q)$ for Ti, O, and Cl. 66

2-13 A general lattice consisting of a Bravais lattice with unit vectors a_i and a basis with unit vectors τ_i. 67

2-14 Polarized x-rays incident on a single electron. The electron oscillates with the electric field and as a result emits light polarized parallel to the incident beam. 69

2-15 The scattering vectors k_i, k_f, and Q form the scattering triangle. For a given energy, there is a solid angle of 4π into which the scattering can occur, as illustrated by the 2D projection of the Ewald sphere in figure a). Figure b) illustrates the smearing effect of the finite crystal size on the reciprocal lattice points, as well as the broadening of the Ewald sphere due to slight non-monochromicity of the beam. Also illustrated is the difference in path length for a reciprocal lattice point through the Ewald sphere for scans along two different $\vec{Q}$ directions. 70

2-16 Visualization of multiple scattering using Bragg planes (a), and the Ewald construction (b). The vectors $\vec{k_i}$, and $\vec{k_f}$ are the incident and final vectors which satisfy the scattering condition $\vec{Q}$. However, photons can also be scattered into $\vec{k_i'}$ with momentum transfer $\vec{Q}'$ which also satisfies the scattering condition, since $\vec{Q}'$ falls on the Ewald sphere. This process will be detected at $\vec{k_f}$ if $\vec{Q}'$ and $\vec{Q}'' \equiv \vec{Q} - \vec{Q}'$ are allowed reflections. 74

2-17 Renniger plot in a small range of Energy and Azimuth for LSCO at the forbidden (0 3 0) reflection. The plot in the lower panel corresponds to a measurement of the scattering intensity along the red line drawn on the Renniger plot. The small energy difference is due to slightly different lattice parameters used in the calculation and experiment. . 75

2-18 a) Reciprocal space map of scattering due to 3 misaligned single crystals. b) Simulated Debye-Scherrer rings for TiOCl. c) Scattering geometry schematic showing the fraction of crystals aligned within a range $d2\theta$ of the scattering angle. 77

2-19 Inelastic x-ray scattering diffractometer at sector 3 of the Advanced Light Source at Argonne National Laboratory. The angles and distances are not to scale. Unique features of this instrument are the in-line monochromator and focusing analyzer. The inset shows a Ge-111 crystal deflecting the beam to lower 2θ angles allowing access to higher Bragg angles. Without the crystal the maximum 2θ is $\sim 18^o$. The crystal allows a maximum of $\sim 30^o$. 80

2-20 a)Schematic of a Josephson junction. The macroscopic wavefunction tunnels from one superconductor to the other through the insulator with a phase shift, $\delta = \phi_2 - \phi_1$. b) A Meissner loop with two Josephson junctions with a flux Φ passing through the middle. A constant bias current I is applied through each junction. If $\Phi = 0$, then the phases through each branch of the loop are equal and $V = 0$. As Φ is increased, the voltage at V will oscillate as a a function of applied flux with a period $\Phi_0 = hc/e$. 85

2-21 Quantum Design MPMS magnetic moment measurement. Sample is translated through the solenoid pickup coil which is connected to the SQUID circuit. Plotted is a measured response to the translation (filled circles) with its theoretical fit (line). 85

2-22 Quantum Design heat capacity puck. The sample is attached to the white platform using a thermally conducting grease. Under the platform are the heater and thermometer for the calorimeter. The puck is then inserted into a socket of the PPMS which connects it to the system circuitry and temperature control. 86

3-1 TiOCl powder diffraction pattern measured on a rotating anode diffractometer. The sloping background in a) is an experimental artifact, and has therefore been subtracted in b) for better comparison with the calculated diffraction. The arrows indicate measured peaks which do not occur in the calculated pattern. 90

3-2 Plot of DC susceptibility measured on $\sim$ 50mg of TiOCl powder with highlighted characteristic magnetic signatures (according to Seidel et. al. [4]). The applied field, H, and sample mass have been divided out to convert measured magnetic moment to magnetic susceptibility. . . 91

3-3 DC Susceptibility with low temperature (T < 50 K) region fitted to curie law, $\chi(T) = \frac{c}{T} + \chi_0$. 93

3-4 Sealed quartz tube with TiOCl single crystals on one side and powder residue on the other. This was one of the more successful growths in terms of crystal quality and size. 94

3-5 TiOCl single crystal viewed under an optical microscope with back-lighting. This was the biggest crystal from all of the growth attempts (extracted from the tube pictured in figure 3-4). It is $\sim 100 \times 50mm$ across, and $\sim 50\mu m$ thick. On average the crystals were rectangular having dimensions $\sim 30mm \times 40mm \times 40\mu m$ along a,b,c respectively. 95

3-6 Powder diffraction measured at the NSLS beamline X7A. The inset shows the raw data which has a weakly 2θ dependent baseline which has been subtracted for better comparison with the calculated pattern. The arrow highlights a small impurity peak. Compared to the diffraction pattern in figure 3-1, this diffraction pattern has far better signal to background, and a larger range in Q. Taking these into consideration, one can concluded that the single crystal structure and stoichiometry are nearly ideal. 96

3-7 Glass lathe for making TiOCl single crystal growth chambers. The chucks of the lathe are hollow stainless steel tubes which also serve as the pulleys. Both chucks are coupled to the motor by bands which turn around a long rod. This design allows the translation of one of the chucks while keeping both turning at the same rate. The glass tube can be any arbitrary length and the hollow chuck design allows for a vacuum tube to be connected through a swivel joint to the end of the tube. 98

3-8 Apparatus to aid in assembling ~1000 co-aligned single crystals for neutron scattering experiment. The alignment procedure is discussed in detail in the text. Below is a wiring diagram for the electronics. The sole purpose of the circuit is to provide the proper voltage to the source of the diode, and as well provide a variable voltage to the laser, which was a pen laser modified to be plugged into a DC power source. 100

3-9 Assembled crystal mosaic along with a characteristic rocking curve measured on a triple axis neutron spectrometer showing an angular spread of 3^o, slightly larger than the 2^o desired. 102

3-10 a) Sample mount configuration for anisotropy measurements. The stack of co-aligned samples is squeezed between two thin strips cut from a plastic drinking straw. The strips are then spot welded on either side of the crystal stack to hold them in place. The entire assembly is then spot-welded to the inside of a drinking straw. This allowed for a small-uniform background. b) The susceptibility measured along the a,b,c directions. The curie tail has been fitted and then the temperature dependent part subtracted out. Clearly, the data look practically identical, with only a small temperature independent offset, most likely due to crystal field anisotropy. 103

3-11 a) Magnetic susceptibility upon warming and cooling after the subtraction of a small curie tail. The signature sharp drops at T_{c2}=92 K and T_{c_1} = 66 K (cooling) are clearly present. The quantity $d(\chi T)/dT$ (b) which is proportional to C_p/T, which has peaks corresponding to C_p (c), indicating a magnetic contribution to the total change in entropy at these temperatures. 105

3-12 Plot of the thermal expansion for each lattice constant in TiOCl. The structural details are discussed in section 1.4. 107

3-13 Comparison of various real space monatomic lattices with corresponding reciprocal lattices. The size of the reciprocal lattice point is proportional to the relative intensity (as calculated using equation 2.39). a) A 2D rectangular lattice with a 2 atom basis, R_1=(0,0), R_2=(0.5,0.5). In this case the unit cell is bi-layered in both a,b directions, therefore only h,k with h+k=2n are allowed. b) Unit cell preserving lattice distortion, R_1=(0,0), R_2=(0.6,0.5). The main allowed Bragg peaks remain but in addition, some of the forbidden peaks become allowed, albeit with much smaller intensity. c)Unit cell doubling distortion. The doubled unit cell now has a 4 atom basis: R_1=(0,0),R_2=(0.5,0), R_3=(0.2,0.5),R_4=(0.8,0.5). The allowed peaks in the undistorted lattice are the most intense for the doubled unit cell reciprocal lattice. However, new sets of points have filled in the h+1/2 positions, consistent with the doubling along h in real space. 109

3-14 Schematic representations of various lattice modulations, along with the corresponding exact numerical diffraction pattern (direct structure factor calculation, i.e. no expansions). In the atomic chains, the atomic color is representative of the displacement magnitude, red=δ, blue=$-\delta$. In the third displacement pattern the stationary atom separating the domains is known as a soliton [5]. The upper plots for the sine and square waves show the diffraction from a modulation which is an integer multiple of the unit cell and is therefore commensurate. Note that the intensities are plotted on the same scale but the modulation amplitude for the square wave is nearly a factor of ten less than that of the sine wave. In the lower frame of the sine modulation, the wavelength is simply an incommensurate multiple of the unit cell. For the square wave, an incommensurate modulation is difficult to interpret, since by definition a square wave is discrete, and therefore must always be commensurate. By choosing an odd number the wavelength, $\lambda = 9$, the modulation is a mixture of 4,5 for $\lambda/2$ lengths. 112

3-15 Red curve is a sinusoidal modulation along with a soliton modulation. The soliton width Γ is defined along with the soliton separation given by π/q, where q is the position of the observed satellite peak in reciprocal space. 115

3-16 Schematic drawing of the model lattice used to fit the measured peak intensities. The supercell has dimensions (A,B,C)=(a,2b,c). The adjustable fitting parameters were the dimerization magnitude, δ, and a relative translation of neighboring chains, τ. 118

3-17 Longitudinal (a) and transverse (b) scans through (0 2.5 0) the commensurate position along with the temperature dependence of the integrated intensity (c), which exhibits a thermal hysteresis with a width comparable to that of the magnetic susceptibility (c inset). The line through the data in c) is a guide to the eye. 120

3-18 Long scans along H showing the incommensurate and commensurate peaks present at different temperatures. The commesurate scan has been offset from zero for clarity. The incommensurate scan is at a K of 2.492. 121

3-19 Temperature dependence of fitted peak parameters for commensurate and incommensurate temperature regions. The incommensurate intensity in figure a is fit to a power law $(T-T_c)^{\beta}$. The FWHM quoted in figure b, is that along the H direction. Along K, the peak remained resolution limited. The inset of figure c shows the parameter δ, which is the change in wavelength of the incommensurate modulation along with the exact theoretical model of McMillan ([6]). 124

3-20 Mesh scans showing the temperature evolution from incommensurate to commensurate. The scale is a log scale, so much of the width is most likely due to low intensity diffuse scattering. 125

3-21 Mesh scan showing the first and third harmonics on the $-\Delta K$ side of the commensurate position. No third harmonics were observed on the $+\Delta K$ side (see text). The table contains the positions and relative intensities of each of the observed peaks. The peaks are numbered from right to left and top to bottom. 126

3-22 Cartoon showing that the boundary between two anti-phase domains in a dimerized lattice is a single undimerized atom, known as a soliton. The soliton spacing gives the incommensurate wavevector. 127

3-23 The commensurate state can be modelled by a sine wave with the extrema centered on the atomic positions (a). To get a splitting about the commmensurate position along the b-direction, the wavelength of the sine wave can be made slightly different from 2 (b). The asymmetry results from phase shifting the modulation of one chain with respect to its neighbor (c). Finally, one diagonal of the incommensurate diffraction pattern in 3-21 can be obtained by phase shifting the modulation of each unit cell along the a direction. The overall phase shift increases with increasing a. Here the atomic positions are defined as (x,y) = (ma,nb). 128

3-24 Fully modelled incommensurate diffraction along with a schematic of the atomic positions which generate the pattern. The solitons are highlighted in yellow, and the shading highlights the anti-phase domains which occur across the diagonal boundary. The atomic shifts have been exaggerated for illustration purposes. The parameters which give this pattern are discussed in the text. 129

3-25 Comparison of the commensurate peak with first and third incommensurate harmonics (figures a,b), and (figure c) the ratio I3/I1 as a function of the incommensuration, ΔQ, with a fit line to the expected behavior for a soliton with width $\Gamma = 8$Å. 132

3-26 Cartoon illustrating that a simple rectangular lattice has no problem dimerizing, whereas a staggered lattice, like TiOCl, cannot satsify equal atomic spacing for every atom for a given dimer length. This gives rise to a frustration of the lattice energy. 133

3-27 a) Example of a coupled harmonic oscillator: mass 1, is connected to a wall by spring 1, and to mass 2 by spring 2. Mass 2 is connected to a wall by spring 3, and to mass 1 by spring 2. The masses of are m_1 and m_2 respectively. In b)-e), the masses and spring constants have been set to be equal. Figures b),c) show the longitudinal normal modes, and d),e) show the transverse normal modes. 137

3-28 a) Example in figure 3-27 extended to a linear chain of N atoms. b) Energy dispersion for equal masses and spring constants. This "acoustic" dispersion is characterized by a linear slope at $q = 0$. c) Energy dispersion curves from equation 3.40, with $k_2 = 1.5k_1$. There are now two branches, one acoustic and one which does not disperse to $\omega = 0$ for $q = 0$. This upper mode is known as the "optical" mode. Notice that the periodicity of the dispersion has changed by a factor of 2, due to the doubling of the periodic unit on the chain (as indicated by a'). 140

3-29 Buckingham $V(r) = Ae^{\frac{r}{\rho}} - \frac{C}{r^6}$, and Lennard-Jones (6-12): $V(r) = \frac{A}{r^6} - \frac{B}{r^12}$. The various curves show different ratios of A/C ($\rho = 0.1$) for Buckingham, and A/B for Lennard-Jones. As each of these ratios increases, the potential becomes more repulsive. 144

3-30 The Pseudopotential approximates the high energy, quickly oscillating core wavefunction with a slowly varying wavefunction, which is orthogonal to the core states, resulting in a weak enough potential to allow calculation using nearly free electron states. The cut-off radius, is a distance above which the pseudopotential and real potential match. . 145

3-31 Plot of damped harmonic oscillator response function for a) underdamped, b) strongly damped, and c) overdamped cases 149

3-32 Raw IXS data measured along the (0 K 0) direction as a function of $q = (02 - \xi 0)$ for T = 80 K, T = 100 K, T=300 K. The 100 K datasets at q=0.05 and q=0.1 have been scaled by the indicated factors, and a constant offset has been added to the data for clarity. The lines are fits to equation 3.56 convoluted with the resolution function (see text). 157

3-33 Illustration of how passing a resolution function with finite width in Q through a sloped dispersion curve will broaden the observed peak in energy. For the sector 3 beamline the rectangular resolution function shown is a good estimate (see text). 158

3-34 Fitted peak center and width for the data in figure 3-32. The solid lines are phonon dispersions with the allowed vibrational symmetry for scattering in the (0 K 0) direction calculated using a shell model (see 3.4.1). The dashed line is a guide to the eye. 160

3-35 Diagram showing the atomic motions associated with the two acoustic mode vibrations calculated to be present along the (0 K 0) direction. 162

3-36 Plot of the dynamic structure factor for all of the observed modes. The peak positions and intensities were extracted from the shell model calculation. 163

3-37 a)Energy scans measured at Q=(0,1.5,0) for different temperatures. The acoustic mode shows a clear softening, and as a result becomes overdamped. The plot in b) is the temperature dependence of T/I, a value proportional to ω_0^2 for the overdamped mode with a line draw through the 100 K, 150 K points indicating a T_c of 88.5 K (see text). The temperature dependence of ω_0^2/Γ, a parameter independent of T/I which also tends to zero around 100 K. This implies that the spin-Peierls transition occurs at 92 K, rather than 65 K, consistent with our model of the incommensurately modulated dimer pairs. 165

3-38 Eigenvector of the zone boundary acoustic mode. At the zone boundary, the b and c acoustic modes are degenerate, meaning there is an infinite number of linear combinations of the b and c polarizations. This is illustrated by showing half of the atoms with one polarization and half with the orthogonal polarization. However since it is a zone boundary mode, the center of mass of the vibration has to be the shared edge of two neighboring unit cells. Therefore, the atom in one unit cell must vibrate completely out of phase with its counterpart in the neighboring unit cell. 166

3-39 Survey of the dependence of $\Pi_{CF}(q, \omega)$ on the various parameters. All panels are comparing $\sqrt{-\Re[\Pi]}$ with $\Im[\Pi]/\omega$, which from equation 3.63 is equivalent to comparing the width with the shift from Ω_0. Panel a),b) contain the real and imaginary parts of $\Pi_{CF}(\omega)$ at different g values, for q=0.5, and T=300K. Panels c),d) compare the temperature dependence for two different values of g. Finally, e),f) show the dependence of $\Pi(q)$ on J. 168

3-40 Raw data and fits to eq. at different temperatures. An offset has been added for clarity. 170

3-41 a) Fitted values for the harmonic frequency of the longitudinal acoustic mode as a function of q at $T = 100K$ and $T = 300K$, along with the harmonic dispersion expected from the shell model calculation. b) The ratio of the fitted g to g calculated using equation 3.73 (see text). The value of Ω_0 used was the 300 K, q=0.5 value from panel a). c) Plot of ω_0 values deduced from Ω_0 using equation 3.72), along with the expected ω_0 using g fixed at the value given by equation 3.73. The line through the deduced ω_0 points is a fit to A$\sqrt{T - T_c}$ help quantify T_c. The fitted result is $T_c = 98K$. 171

List of Tables

3.1 Parameters used in shell model calculation of the phonon dispersion curves in figure 3-32 161

3.2 Spin-Peierls critical temperature T_c, J, and spin-phonon coupling α for various spin-Peierls materials (from reference [29]) along with the new values for TiOCl 174

1 Introduction and Motivation

While the study of spin interactions in solid state materials is a well established science, real interest in understanding microscopic origins of collective spin behavior took a major upturn in recent decades in an attempt to better understand magnetic properties of high temperature superconductors. An area of real interest which remains speculative are the lower dimensional spin-1/2 lattice structures, where the effects of quantum fluctuations on static long range order for T=0 is an open theoretical question[7]. To gain a little insight into the origin of this uncertainty, we can perform a few simple calculations. A Hamiltonian which accounts for the spin degrees of freedom is the Heisenberg Hamiltonian

$$H = J \sum_{\langle i,j \rangle} \vec{S}_i \cdot \vec{S}_j, \tag{1.1}$$

where the sum is over nearest neighbor pairs, labelled by i, j. As a first step to finding the ground state, it is useful to first calculate the ground state energy. This is most easily done by rewriting $\vec{S}_i \cdot \vec{S}_j$ in terms of the total nearest neighbor spin,

$$\vec{S}_i \cdot \vec{S}_j = \sum_{\langle i,j \rangle} \frac{1}{2} \left(\left(\vec{S}_i + \vec{S}_j \right)^2 - \hat{S}_i^2 - \hat{S}_j^2 \right). \tag{1.2}$$

If S_i, and S_j each have spin s, with total spin S, then the energy of 1.1 is

$$E_{ij} = J \left[\frac{1}{2} S(S+1) - s\,(s+1) \right]. \tag{1.3}$$

Starting with expression 1.3, we can clearly see two different cases for magnetic ground states, for different signs of J. If $J < 0$, or $J = -|J|$, then the minimum occurs when the two spins are parallel making the total spin $S = 2s$, and $E = -|J|s^2$.

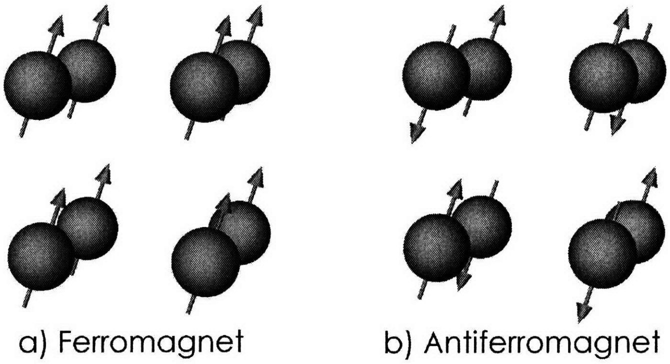
a) Ferromagnet b) Antiferromagnet

Figure 1-1: Cubic lattice with ferromagnetic (a) and antiferromagnetic (b) spin order.

If we now generalize this to N spins on a lattice, we see that the ground state is one in which all spins are aligned parallel to each other. Such a state is known as a *ferromagnetic* state (figure 1-1a). Of course, this state can only be allowed if it is an eigenstate of the Hamiltonian, so to check, it is convenient to expand the dot product, and rewrite the the operators S_x, S_y in terms of raising and lowering operators

$$\hat{S}_x = \frac{1}{2}\left(\hat{S}_+ + \hat{S}_-\right), \quad \hat{S}_y = \frac{1}{2i}\left(\hat{S}_+ - \hat{S}_-\right).$$

Then equation 1.1 becomes

$$\hat{H} = J\sum_{\langle i,j\rangle} \hat{S}_i^z\hat{S}_j^z + \frac{1}{2}\left(\hat{S}_i^+\hat{S}_j^- + \hat{S}_i^-\hat{S}_j^+\right). \tag{1.4}$$

Recalling that $S_+|\uparrow\rangle = 0$, and applying H to the state $|\uparrow\uparrow\uparrow ...\rangle$,

$$\begin{aligned}
\hat{H}|\uparrow\uparrow\uparrow ...\rangle &= J\sum_{\langle i,j\rangle} \hat{S}_i^z\hat{S}_j^z|\uparrow\uparrow\uparrow ...\rangle + \frac{1}{2}\left(\hat{S}_i^+\hat{S}_j^-|\uparrow\uparrow\uparrow ...\rangle + \hat{S}_i^-\hat{S}_j^+|\uparrow\uparrow\uparrow ...\rangle\right) \\
&= J\sum_{\langle i,j\rangle} \hat{S}_i^z\hat{S}_j^z|\uparrow\uparrow\uparrow ...\rangle \\
&= J\sum_{\langle i,j\rangle} s^2|\uparrow\uparrow\uparrow ...\rangle.
\end{aligned}$$

It can therefore be concluded that the the ferromagnetic ground state is indeed an eigenstate of $\hat{H}$, with ground state energy JNS^2.

The case for $J > 0$ turns out to be a bit more elusive. Following along the same lines as for the ferromagnet, we begin by minimizing the energy. In this case, the minimum energy occurs when $\vec{S}_i$ is anti-parallel to $\vec{S}_j$ for a total spin of 0, or singlet state, with an energy of $E_{ij} = -JS(S+1)$. Because the spins are anti-aligned, this state is known as an *antiferromagnet.*

One proposed ground state for the antiferromagnetic Heiesenberg Hamiltonian is a periodic arrangement of oppositely aligned spins. Such a state can be constructed out of inter-penetrating anti-parallel ferromagnetic sub-lattices (figure 1-1b). Just as with the ferromagnet, we can apply the Heisenberg Hamiltonian to calculate the ground state energy.

$$\begin{aligned}
\hat{H}|...\downarrow\uparrow\downarrow...\rangle &= J\sum_{\langle i,j\rangle}\hat{S}_i^z\hat{S}_j^z|...\downarrow\uparrow\downarrow...\rangle + \frac{1}{2}\left(\hat{S}_i^+\hat{S}_j^-|...\downarrow\uparrow\downarrow...\rangle + \hat{S}_i^-\hat{S}_j^+|...\downarrow\uparrow\downarrow...\rangle\right)\\
&= J\sum_{\langle i,j\rangle}\hat{S}_i^z\hat{S}_j^z|...\downarrow\uparrow\downarrow...\rangle + \frac{1}{2}\left(\hat{S}_i^+\hat{S}_j^-|...\downarrow\uparrow\downarrow...\rangle\right)\\
&= J\sum_{\langle i,j\rangle}s^2|...\downarrow\uparrow\downarrow...\rangle + |...\uparrow\downarrow\downarrow...\rangle,
\end{aligned}$$

therefore the Neél energy is $E = -JNs^2$. It turns out that a better estimate for the ground state energy can be obtained by considering a state of non-interacting singlets. For N spins, there will be $N/2$ singlets, each having energy $-Js(s+1)$, resulting in a total energy of

$$E_{singlet} = -\frac{N}{2}Js(s+1) = -JNs^2 + \frac{N}{2}\left(Js^2 - Js\right) \tag{1.5}$$

From this we can see that the singlet energy is only lower for $s < 1$.

Going back to the Neél state, we see that the S_z term gives an energy of $-JNs^2$, but the $S^{\pm}S^{\mp}$ operators change the state, therefore the Neél state is not an eigenstate of the Heisenberg Hamiltonian. If we compare this energy with the $-JNs(s+1)$, we see that the Neél energy only differs from the ground state energy by an amount $-JNs$, which must come from the raising and lowering operators. From this it can be concluded that the ground state is primarily Neél ordered with fluctuations of the spin direction. An estimate for the influence of fluctuations on the ordered Neél state can be obtained by comparing the ratio of the ground state energy correction term (Js) to the Neél energy ($-Js^2$),

$$\frac{dE}{E_{\text{Neél}}} \sim \frac{Js}{Js^2} = \frac{1}{s}. \tag{1.6}$$

So for large s, the Neél state very nearly estimates the ground state, but for small s, the energy correction due to fluctuations becomes significant. This makes the $s = 1/2$ case especially interesting, since it has the largest deviation from Neél order. In a more rigorous derivation of equation 1.6, we would have considered the number of nearest neighbors as well. For a spin with coordination number, n, the result in 1.6 becomes

$$\frac{dE}{E_{\text{Neél}}} \sim \frac{1}{ns}, \tag{1.7}$$

which implies that the influence of fluctuations becomes increasingly important with decreased coordination number. From this we would then expect that the system where fluctuations play the most significant role is the one dimensional $s = 1/2$ system, where $s = 1/2$ and $n = 1$ both maximize . This has some very interesting consequences, which combined with its attractive theoretical simplicity makes one dimensional magnetism a rich field for the study of quantum magnetism.

The exact ground state for the 1-D $s = 1/2$ Heisenberg chain was derived exactly by Hans Bethe in 1931[8]. He found that the 1D ground state is a complicated superposition state, which does not order down to $T = 0K$. Later, in 1938, Lamek Hulthén found the ground state energy to be $E = -.43JN$[9]. Earlier we found that the uniform Neél energy could be lowered by deforming it into a system of non-interacting singlets. In an analogous manner, one must therefore wonder if a lower energy state exists for a deformeable Bethe state. It turns out that a uniform 1-D chain can lower its energy by pairing up into dimers creating a chain of alternating bonds. For spins on a lattice this leads to a deformation of the chain at some finite temperature. The transition from the uniform chain to dimerized chain driven by nearest neighbor spin interaction is known as a *spin-Peierls* transistion.

a) Uniform 1-D lattice

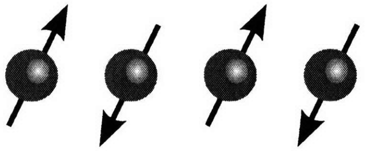

b) Dimerized 1-D lattice

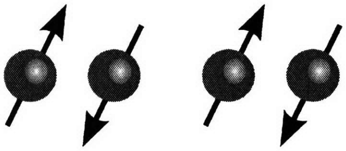

Figure 1-2: Spins on a lattice can lower their energy by pairing up into singlets. This results in a chain of dimerized atoms.

1.1 Spin-Peierls basics

The name for the spin-Peierls state is derived from the regular Peierls state for a 1-D metal with a half-filled band. A small lattice distortion results in a splitting of the band about the Fermi energy thus lowering the electron energy. If the gain in electron energy is greater than the cost in lattice energy, the lattice dimerizes. In a sense the spin-Peierls transition shares a lot of similar concepts with the metallic peierls system. Basically the driving force behind the distortion is the tendency for neighboring spins to form singlet pairs. If the energy gained by forming a singlet is greater than the energy lost due to distorting the lattice, a spin-Peierls transition occurs. For the case of the metallic Peierls transition, this energy gain could be understood by a gap formation about the Fermi level. An analogous gap occurs in a spin-Peierls transition, but to understand this gap requires a little background in 1D Heisenberg chains.

1.1.1 1D Spin Chains

In one dimension the Heisenberg Hamiltonian (eq. 1.1) simplifies to

$$\hat{H} = J\sum_i \vec{S}_i \cdot \vec{S}_{i+1} = J\sum_i S_i^z S_{i+2}^z + \frac{1}{2}\left(S_i^+ S_{i+1}^- + S_i^- S_{i+1}^+\right). \tag{1.8}$$

In 1, we explored the FM and AFM ground states of the Heisenberg Hamiltonian. To understand the spin-Peierls state, we have to discuss the excitation spectrum in the 1D Heisenberg chain. As one would expect, the easy case is the FM, where the elementary excitation is a $\Delta S = 1$ spin flip,

$$\begin{array}{cc} \text{Ground State} & \text{Excited State} \\ |\uparrow\uparrow\uparrow \ldots\rangle & \rightarrow |\uparrow\downarrow\uparrow \ldots\rangle, \end{array}$$

known as a *magnon*. It can be shown that a magnon disperses as $1-\cos(q)$ [1], where q is the Brillouin Zone momentum transfer. Not surprisingly, the AFM picture isn't quite as simple, since there is no static long range order due to quantum fluctuations. Like the magnon, the first excited state for a 1D AFM chain is a $\Delta S = 1$ excitation, which is visualized for a 1-D Neél lattice in figure 1-3. The red lines in indicate a domain

---

[1] See for example reference [10]

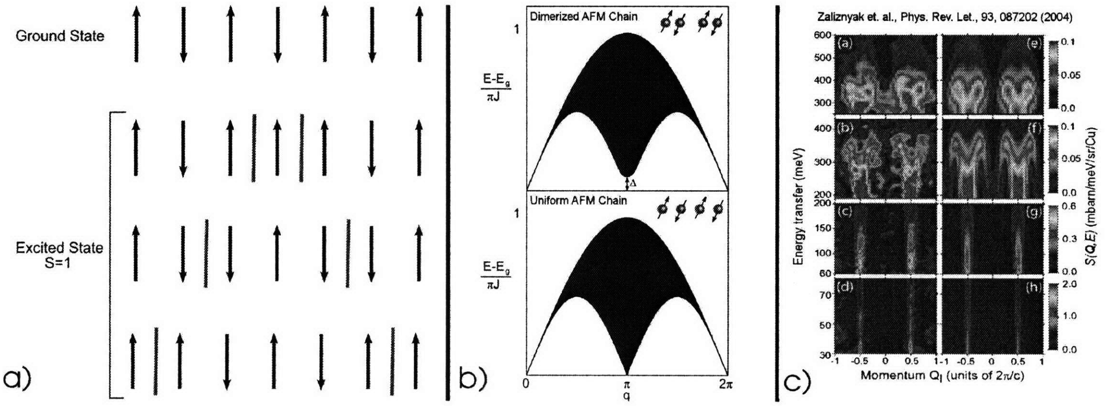

Figure 1-3: a) A 1-D AF chain with a $\Delta S = 1$ excitation. The red lines indicate domain walls, which can be separated by any arbitrary distance with no energy cost. b) Numerically calculated spinon continuum with 256 k-points following the numerical recipe in [1][2]. c) Spinon continuum observed in $SrCuO_3$ with neutrons [3].

wall between otherwise ordered segments of chain. Each domain wall corresponds to has a total spin $\Delta S = 1/2$ associated with it. Therefore, in order to have a $\Delta S = 1$ excitation the domain walls always come in pairs. Since the energy is the same for any arbitrary separation of domain wall, they are decoupled and can be effectively treated as independent spin-1/2 quasi-particles, known as *spinons*. The spinon is regarded as the elementary excitation of the 1D AF Heisenberg chain, which is only excited in pairs non-interacting pairs. In 1962 Cloizeaux and Pearson in 1962 worked out the energy dispersion for a single spinon excitation and found[11].

$$E_{CP}(q) = \frac{\pi J}{2} |\sin(\pi q)|, \tag{1.9}$$

where q is the momentum transfer reduced to the first BZ in reciprocal lattice units. Note the argument πq corresponds to a two unitcell periodicity in real space, which reflects the presence of Neél order even though the ground state is known to be disordered[12]. Since spinons are excited in pairs, the energy of both spinons must be accounted for. The value of interest is the total energy $E(q)$ of a two spinon excitation, with $q = q_1 + q_2$ being the sum of the individual spinon momentum transfers q_1, q_2. The absolute lowest energy mode is when both spinons are long-wavelength modes at $q = 0$. For q away from zero, the lowest energy can be obtained by lifting the energy of only one spinon (i.e. give the spinon a small q), keeping keeping the other at at zero, therefore we would expect a lower bound on the energy throughout the Brillouin zone to have the form of a single spinon dispersion, given by 1.9. The same procedure can be performed keeping one spinon fixed at a small q_1 giving $E_{CP}(q_1)$, then at $2\delta E$, and so forth. The maximum energy configuration is when both spinons have wavevector $q' = \pi/2$ (2 unitcell wavelength), for a total $q = 2q' = \pi$. We therefore expect that the value of the maximum will occur at $q = \pi$, and be equal to $E_{tot} = 2E_{CP}(q_1 = q_2 = \pi/2) = \pi J$, Generally speaking, for any q, we would expect that the maximum energy occurs when both spinons have equal values of

$q_1 = q_2 = q/2$. Therefore the upper bound of excitations as a function of q should be

$$E_{upper}(q) = 2E_{CP}(q_1 = q_2 = q/2) = \pi J|\sin(\pi q/2)|. \tag{1.10}$$

This in fact is the exact form for the upper bound for the two spinon excitation determined first approximately by [13], then exactly by [14]. In between equations 1.10 and 1.9 is a continuum of two spinon excitation states. This has been experimentally verified by neutron scattering. A recent example of a neutron scattering spectrum from the nearly ideal 1D Heisenberg system $SrSuO_2$ is shown in figure 1-3c. Unlike the lowest excited state, the highest excited state has the periodicity of the lattice, reflecting the deviation from the Neél ordered state due to fluctuations.

1.1.2 Spin-Peierls Gap

In the beginning of this section, the spin-Peierls instability was motivated by drawing an analogy to the metallic Peierls instability. At the time, we lacked the background to draw the connection, but with the introduction of the spinon continuum, we can now discuss the spin-Peierls transition in a parallel manner to the Peierls instability. From equation 1.9, the lower bound of the continuum extents to E=0 at the zone boundary (q=1/2). Therefore, analogous to the Peierls instability, the system can gain energy by dimerizing, resulting in the formation of a gap to short wavelength excitations at the zone boundary.

On the one hand the spin energy favors dimerizing the lattice, but the lattice energy tries to maintain a uniform spacing. In order for a spin-Peierls transition to occur, the gain in spin energy has to exceed the cost in lattice energy. For a distortion of magnitude δ, mean field theory predicts the gain in spin energy to be proportional to $\delta^{4/3}$[15]. In the harmonic approximation the dimerization requires an energy $\sim \delta^2$. Therefore the total change in energy is

$$E \sim \delta^2 - \delta^{4/3}, \tag{1.11}$$

which for $\delta << 1$ favors the spin-Peierls transition. Therefore we expect the $T = 0$ state for *any* 1D $s = 1/2$ Heisenberg system to be a dimerized chain. In the next section, the experimental realization of spin-Peierls transitions will be discussed.

1.2 Experimental Realization of the Spin-Peierls State

In the previous section the physics of a 1D spin-1/2 Heisenberg chain was discussed, and we saw that the lowest energy state is a dimerized lattice, or spin-Peierls state. In practice, there are maybe a dozen spin-Peierls systems, even though about a hundred materials have been labelled as "1D". So roughly 10% of "1D" systems have a spin-Peierls ground state, which means that the other 90% are not strictly 1D. Typically in these cases some inter-chain interaction induces higher dimensional order at a finite temperature. Two examples where a nice spinon continuum is observed are $KCuF_3$, which becomes a 3D AFM at 39 K[16], and $SrCuO_2$ which orders at T=3 K[17].

The spin Peierls transition was first observed in 1977 in the organic compound TTF-$CuS_4C_4(CF_3)_4$ (or TTF-CuBDT) by Dave Moncton and his collaborators[18]. The transition temperature was 11 K with pretransitional fluctuations up to 225 K, as measured by diffuse x-ray scattering. The magnetic dimensionality of the system was previously determined by fitting the susceptibility to the Bonner-Fisher theory for a 1D $s = 1/2$ Heisenberg chain [19]. Moncton *et. al.* observed a lattice dimerization at the temperature at which the susceptibility deviated from the Bonner-Fisher curve. Following this spin-Peierls transitions were observed in a handful of additional organic compounds. Due to the crystal size, the experiments which could be performed was limited, therefore many predicted spin-Peierls properties were left to speculation.

The lattice dimerization due to electron singlet pairing was first predicted by H. McConnell and R. Lynden-Bell in 1961[20]. The first systematic theory of spin-Peierls was presented by E. Pytte in 1974. The theory tried to parallel the Peierls theory for a lattice instability in 1D metals. Pytte treated the phonons and spin (fermion) system in a mean-field approximation. For the phonons, this can be physical for low energy modes, but the mean-field treatment of the spin system is expected to be a poor approximation in 1D, which is known to be a fluctuating ground state[21]. Despite this the Pytte theory did yield an estimate for the transition temperature (T_{sp}), the spin-Peierls gap (Δ) and the dimerization amplitude (δ).

The results on TTFCuBDT by Moncton *et. al.* prompted an improvement upon the Pytte theory by M. C. Cross and D. Fisher where the linear response of the spin system was calculated using time-dependent second order perturbation theory[22]. As a result, Cross and Fisher (CF) were able to make predictions about the lattice dynamics leading up to the spin-Peierls transition. They predicted a mode softening induced by the spin-phonon coupling. Unfortunately, quantitative measurements of this proved challenging, since the spin-Peierls materials at time were too small for neutron scattering studies, and the information provided by diffuse x-ray scattering was difficult to interpret.

Spin-Peierls physics experienced a revitalized interest in the early nineties when an apparent spin-Peierls transition was observed in the *inorganic* compound $CuGeO_3$. Since it was possible to grow large single crystals, for the first time detailed neutron studies were available. In the next section some of the the key experimental findings of $CuGeO_3$ will be summarized, and the "spin-Peierls" transition discussed.

1.3 $CuGeO_3$ As a Spin-Peierls System

The spin-Peierls transition in $CuGeO_3$ was first observed in the magnetic susceptibility by M. Hase *et. al.* in 1993[23]. They found a nearly isotropic drop to almost zero at $T = 14K$, which they concluded was due to a spin-Peierls transition. However, in contrast to the organic compounds the high temperature susceptibility for $CuGeO_3$ did not fit well to the Bonner-Fisher theory, which was attributed to either next nearest neighbor interaction or weak inter-chain coupling.

Later, neutron studies verified the lattice dimerization, and well as a gap of 2.3 meV below 14 K[24] [25]. The spin coupling constant, J was measured to be 10.4 meV in the chain and about 1meV and 0.1 meV perpendicular to the chain. Initial neutron exhaustive neutron studies found no sign of a soft phonon mode above T_{sp}[25][26][27]. In a later study two modes were found which *harden* as the transition temperature is approached[28].

This inconsistency with the theory of Cross and Fisher, lead to speculation as to the its validity[29]. Then in 1998, a more detailed theoretical study of the CF response function revealed an energy regime where the spin-Peierls phonon increased upon approaching the transition[15]. This lead to a classification of spin-Peierls transition types into adiabatic and anti-adiabatic. The anti-adiabatic regime was defined by the ratio

$$\frac{\Omega_0}{T_{SP}} > 2.2, \tag{1.12}$$

where Ω_0 is the bare harmonic phonon frequency. The two phonons in $CuGeO_3$ believed to be driving the transition have energies 151 K and 317 K[28]. The spin-Peierls transition temperature is 14.1 K making Ω_0/T_{SP} 10.7 and 22.5, which according to relation 1.12 are well in the anti-adiabatic regime. This was really the first indication that relative energy scales of the frequency and the spin-Peierls temperature had significance. Subsequent theoretical spin-Peierls work seems to substantiate this[30][31][29][32].

The lack of a phonon softening, the slight anisotropy of the susceptibility, the significant inter-chain coupling, the next-nearest neighbor interaction all lead one to wonder how ideal $CuGeO_3$ is as a realization of a spin-Peierls state. As a result, in the 3 decades since its formulation, the CF theory of a soft-mode spin-Peierls transition has not directly been put to the test.

Due to the small crystal size of the organic compounds and the non-ideality of $CuGeO_3$, the theory of spin-Peierls transition is anything but an open-and-shut case. Fortunately, a new compound has been recently discovered, which exhibits nearly ideal 1D characteristics, and has a magnetic susceptibility signature which bares a striking resemblance to that of the organic spin-Peierls compounds. This work summarizes a detailed, systematic study of the 1-D physics in the compound TiOCl.

1.4 TiOCl, A Promising New Spin-Peierls Candidate

TiOCl crystallizes into a structure with an orthorhombic unit cell having Pmmn symmetry. The Ti^{3+} and O^{2-} ions bind strongly to form Ti-O planes which are separated by weakly bound Cl^{-}, creating a quasi 2-dimensional structure (figure 1-4a). The atomic electronic configuration for Ti is $[Ar]\,3d^2 4s^2$, which ionizes to Ti^{3+} in TiOCl resulting in the new $3d^1$ configuration. In other words,, the 3d orbital contains a single electron, which in the scope of magnetism means that the Ti^{3+} ions form a spin 1/2 quasi-2D lattice (figure 1-4c). Recall from chemistry that there are five d-orbitals, the electronic density distributions of which are shown in figure 1-5. The energy levels of all five orbitals are degenerate for a free ion, but in a crystal, this degeneracy is lifted depending on the ligand bonding geometry. In TiOCl, Ti^{3+} forms a distorted octahedron with the neighboring Cl^- and O^{2-} ions (figure 1-4b). In a perfect octahedron molecule, like $TiCl_6$, shown in the upper left corner of figure 1-5, the $d_{x^2-y^2}$ and d_{z^2} point directly toward each of the six ligands, whereas the d_{xy},d_{yz}, and d_{xz} orbitals are rotated 45^o with respect to the octahedral axes, so they point away from the ligands. This results in a splitting of the d-orbital energy into the higher energy e_g ($d_{x^2-y^2}$ and d_{z^2}), and the lower energy t_{2g} (d_{xy}, d_{yz}, d_{xz}) orbitals (figure 1-5, right side). For the $3d^1$ electronic configuration the electron occupies one of the triply degenerate t_{2g} orbitals.

The above description in terms of the energy levels of free atoms is complicated slightly in a crystal. The energy level are smeared out into dispersive bands, the occupation of which is given by the chemical potential, or Fermi level, which is the energy of the highest occupied band. For an octahedron embedded in a crystal, the bands associated with the d-orbitals split into the t_{2g} and e_g bands. In the case of d^1, the Fermi level intersects the t_{2g}bands. Therefore a band structure calculation is required to determine the orbital occupancy. In 2003, Seidel, et. al. performed a Density Functional Theory (DFT) band structure calculation using the Local Density Approximation (LDA) for exchange model for TiOCl [4]. They found that indeed the

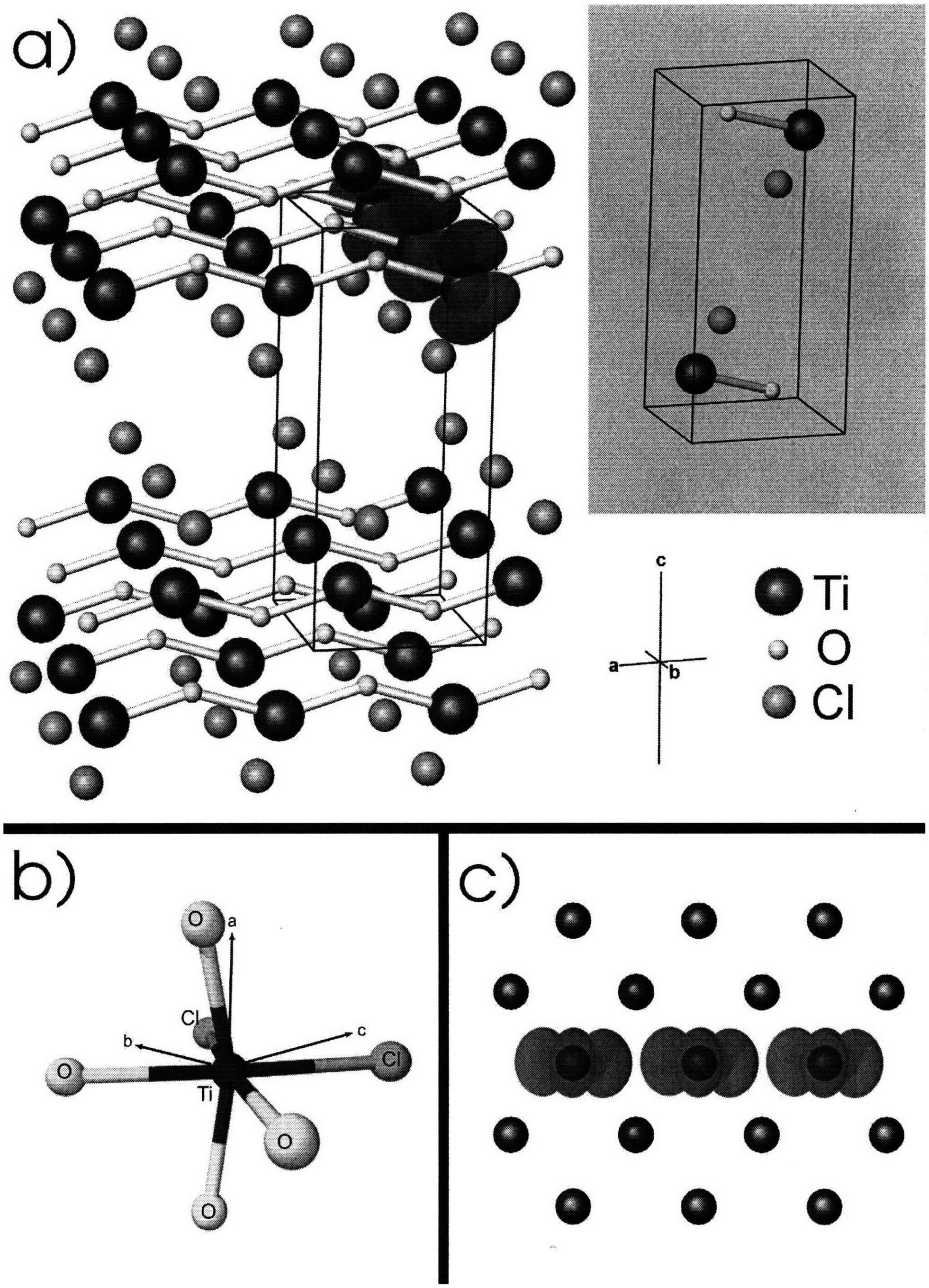

Figure 1-4: a) TiOCl crystal structure with unit cell. b) Ti^{3+} octahedron formed with 4 O^{2-} and 2 Cl^{-} ions. The octahedral z-axis is aligned parallel to a, with the x,y axes rotated 45^o from a,b axes. c) Projection of Ti^{3+} buckle square lattice projected onto the a-b plane. The Ti^{3+} t_{2g} orbitals drawn are the ones which form the 1-D chains along the b-direction.

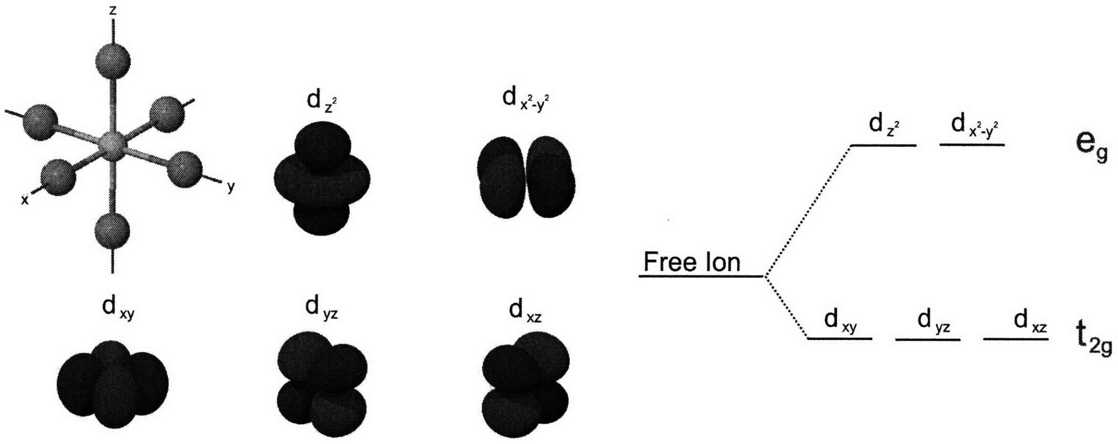

Figure 1-5: Illustration of the d-orbital electron density distribution, shown along with an octahedral $TiCl_6$ molecule for orientation reference. The energy diagram on the right shows the splitting of the degenerate d-levels in an octahedral environment into t_{2g} and e_g.

octahedral environment resulted in the expected band splitting into e_g and t_{2g}, and that the t_{2g} bands are right at the Fermi level. This is problematic, however, since the having a partially filled band would imply that TiOCl is metallic, when experimentally TiOCl was believed to be an insulator, therefore additional interactions were necessary to get the correct band structure. This required modifying the LDA exchange to account for the on-site repulsion which favors one electron (spin) per site. In other words, double occupation of a site costs energy, therefore each spin is localized by the presence of the neighboring spins. This is accounted for by adding an extra potential U, known as the LDA+U exchange correlation. Seidel et. al. LDA+U predicts a splitting of the t_{2g} orbitals about the Fermi level. They then hypothesized that the most likely occupied orbital after the splitting was the d_{xy}, which in TiOCl forms linear chains along the b-direction (see figure 1-4c). This hypothesis was later verified by Angle Resolved PhotoEmission Spectroscopy (ARPES) [33], thus confirming the one dimensionality of TiOCl.

With new understanding of TiOCl as a quasi-1D system, Seidel et. al. turned to the magnetic susceptibility to test whether or not the system exhibited spin-1/2 Heisenberg chain magnetization, by comparing the measured susceptibility to the theory of Bonner and Fisher[34]. Indeed the agreement of the fit at higher temperatures, with only J as an adjustable parameter, was striking. The J determined from the Bonner-Fisher fit was $J = 660K$. On the low temperature end, the susceptibility dropped below the Bonner-Fisher curve at about $T = 150\ K$, followed by a kink at $T = 92\ K$ then finally a sharp drop to zero at $T = 65\ K$. The hypothesis was that the initial drop from the Bonner-Fisher susceptibility was due to the opening of a spin-gap, followed by a *spin-Peierls* transition at $T = 65\ K$. No explanation was given for the 92 K kink.

1.5 Thesis Overview

The thesis begins with a discussion of the process used to grow single crystals of TiOCl used in all of the measurements presented in this study. It then proceeds to answer the questions raised by Seidel *et. al.*:

1. Is the drop in susceptibility isotropic (i.e. S=0 state)?
2. Is the transition at T_{c_1}=65 K a spin-Peierls transition?
3. What is the origin of the transition at T_{c_2}=92 K?

To answer the first question, the magnetic susceptibility as well as specific heat are characterized in detail. A thermal hysteresis at T_{c_1} strongly suggests a first order transition. To test question 2, the TiOCl samples were taken to a synchrotron x-ray source, where a lattice dimerization was observed at T_{c_1}, with a hysteresis similar to that observed in the susceptibility. We also discovered that a precursor to the dimerized lattice below 65 K, is an incommensurate modulation of dimers which first appears at 92 K, thus providing insight as to the nature of the T_{c_2} transition. Finally, we use the latest technological advances in x-ray instrumentation to measure the phonons in TiOCl with 2.2 meV resolution, and find that the longitudinal acoustic mode along the chain direction softens continuously becoming zero at T_{c_2}. However before discussing the data, I will give some general background on x-ray sources and scattering in order to facilitate a more in-depth understanding of our results.

2 Experimental Details

2.1 X-ray Sources

2.1.1 History Of X-ray Sources

The first x-ray diffraction pattern from a crystalline solid was observed in 1912 by Max von Laue et. al. for which von Laue won the Nobel Prize in 1914. In the days of von Laue, x-rays were generated by applying a voltage to a cathode causing it to emit electrons which were then accelerated toward an anode, resulting in Brehmsstrahlung x-ray radiation. However, the intensity was limited by the heat load in the metal. To improve on this, the metal was formed into a cylinder which was then rotated at high speeds, thus distributing the head load over a larger area. This form of x-ray generator, known appropriately as the rotating anode generator, remains a competitive compact source of x-rays for many modern applications, including fundamental scientific research. However, as the demands of research began approaching the limits of what a rotating anode could deliver, scientists began looking into different technologies to generate x-ray radiation.

The answer came to them from high energy physics, a field which requires the acceleration of charged particles to near speed of light velocities. One method employed was the use of synchrotrons, where particles were accelerated in a circular path. The electromagnetic radiation emitted by the accelerated charges had a spectrum which spanned the x-ray regime, with a brilliance far greater than the best rotating anode sources. [1] Unfortunately, synchrotrons used in high energy experiments weren't

---

[1] Brilliance is used to measure the merit of an x-ray source. It is defined as:

$$\frac{photons/sec.}{(beam\ collimation) \cdot (source\ area) \cdot (0.1\%\ bandwidth)} \tag{2.1}$$

optimized to generate x-ray radiation, thus prompting the construction of the first dedicated synchrotron x-ray sources. The main idea behind a synchrotron used as an x-ray source is to maintain a constant electron current which is confined to the ring by periodically spaced magnets, known as "bending magnets". As the electron beam passes through the magnetic field of the bending magnet, it changes direction, and emits radiation. The synchrotron is optimized so that the peak of the radiation spectrum is in the x-ray regime. The details of the radiation from a bending magnet will be discussed in detail in section 2.1.3.

With the construction of synchrotron storage rings using a bending magnet for an x-ray source resulted in orders of magnitude better brilliance than the best rotating anode sources. Just as laboratory source technology improved, so has synchrotron source technology. Modern synchrotrons generate almost $10^1$2 times better brilliance than x-ray sources in the days of von Laue[35]. Such high intensity sources have spawned the innovation of countless quantitative techniques involving x-ray radiation. All of the data presented in section 3.3 were measured using synchrotron x-rays. Of these, the data presented in section 3.4.5 were measured using a technique which has only become possible in the last decade or so with the construction of the latest generation of synchrotron sources. Because of this I find it worth while to take a little time to understand the physics behind modern high brilliance x-ray sources.

2.1.2 Classical Theory of Synchrotron Radiation

The underlying concept to synchrotron x-ray generation is the physics of the power radiated from an electron accelerated by a central force, or a force perpendicular to the direction of travel. In this section I will cover the highlights of the derivation without going into too much mathematical detail. For a more rigorous treatment, the reader is advised to look in any book on advanced electrodynamics, such as [36]. Perhaps the best place to start is with the Liénard-Wiechert Potentials, which describe the

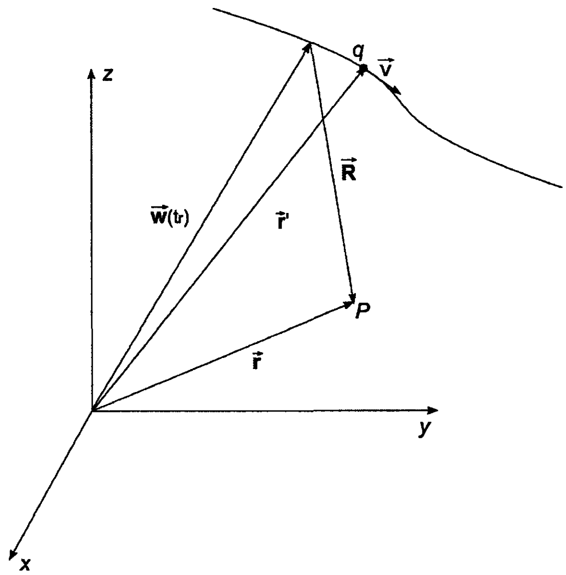

Figure 2-1: Geometry for potential of a charge moving along arbitrary trajectory at velocity v.

vector and scalar potentials of a point charge moving along an arbitrary path.

$$V(\vec{r},t) = \frac{1}{4\pi\epsilon_o} \frac{q}{R\left(1 - \frac{\hat{R}\cdot\vec{v}}{c}\right)} \tag{2.2}$$

$$\vec{A}(\vec{r},t) = \frac{\mu_o}{4\pi} \frac{q\vec{v}}{R\left(1 - \frac{\hat{R}\cdot\vec{v}}{c}\right)}. \tag{2.3}$$

The geometry and vector definitions are shown in figure 2-1. The basic idea is to calculate the scalar and vector potentials due to a point charge located at r' moving with velocity v, measured by an observer at point P. For simplicity, we will first consider the radiation in the rest frame of the charge. The information about the position of the charge propagates at the speed of light, c, so if the observer located at $\vec{r}$ measures the position of the charge $\vec{R}$, at time t, in reality this was the position of the charge at time $t - R/c$, when the charge was at position $\vec{w}(t_r \equiv t - R/c)$.

Using $\vec{E} = -\vec{\nabla}V - \frac{\partial \vec{A}}{\partial t}$ and $\vec{B} = \vec{\nabla} \times \vec{A}$, the electric and magnetic fields, $\vec{E}$ and $\vec{B}$ can be calculated from equations 2.2 and 2.3. The derivation is quite involved and will not be covered here. Again, the reader is directed to reference [36]. The result is:

$$\vec{E}\left(\vec{r},t\right) = \frac{q}{4\pi\epsilon_o}\frac{R}{\left(\vec{R}\cdot\vec{u}\right)^3}\left[\vec{u}\left(c^2-v^2\right)+\vec{R}\times\left(\vec{u}\times\vec{a}\right)\right] \tag{2.4}$$

$$\vec{B}\left(\vec{r},t\right) = \frac{1}{c}\hat{R}\times\vec{E}, \tag{2.5}$$

where the variable $\vec{u} = c\hat{R} - \vec{v}$ has been introduced to simplify the expression. The acceleration $\vec{a}$ enters in as a result of taking the gradient of $R = c(t - t_r)$. It can be shown that $\vec{\nabla}R = -c\vec{\nabla}_{t_r}$, which is then applied to the quantity $(\vec{R}\cdot\vec{v})$, resulting in the time derivative of the velocity. Quite a few steps have been skipped to bring us to the subject of interest, and that is the radiated power from the moving charge. The power can be obtained in the usual way by calculating the Poynting vector using equations 2.4 and 2.5

$$\vec{S} = \frac{1}{\mu_0}(\vec{E}\times\vec{B}) = \frac{1}{\mu_0 c}\left[\vec{E}\times\left(\hat{R}\times\vec{E}\right)\right] = \frac{1}{\mu_0}\left[\hat{R}E^2 - \vec{E}\left(\hat{R}\cdot\vec{E}\right)\right], \tag{2.6}$$

where the so-called BAC-CAB vector multiplication identity has been used to transform the triple cross-product in the second term. The total radiated power is then the integral of $\vec{S}$ over the surface of a sphere with radius R in the limit $R \to \infty$. The area of the sphere is proportional to R^2, thus only terms in $\vec{S}$ of order $1/R^n, n \leq 2$ will survive in the infinite R limit. Since $\vec{S}$ is proportional to E^2, only terms of $1/R$ in E will survive. From equation 2.4, it is clear that only the second term satisfies this. The implication is that acceleration of the point charge is necessary for electromagnetic radiation. The acceleration term in $\vec{E}$ can be rewritten using the BAC-CAB multiplication identity, giving

$$\vec{E_{\text{inf}}} = \frac{q}{4\pi\epsilon_0 c^2}\frac{1}{R}\left[\hat{R}\times\left(\hat{R}\times\vec{a}\right)\right] = \frac{q}{4\pi\epsilon_0 c^2}\frac{1}{R^2}\left[\hat{R}\left(\hat{R}\cdot\vec{a}\right)-\vec{a}\right]. \tag{2.7}$$

Using this result along with the fact that radiation fields are perpendicular to the

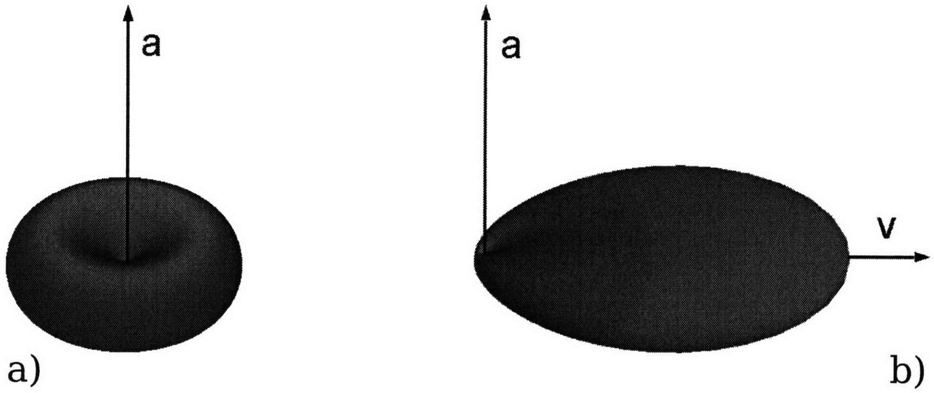

Figure 2-2: Angular distribution of power radiated from a charge moving perpendicular to the acceleration in the rest frame (a) and in the moving frame (b).

propagation direction, or $\vec{E} \cdot \hat{R} = 0$, equation 2.6 reduces to

$$\vec{S_{\text{inf}}} = \frac{1}{\mu_0 c} E_{\text{inf}}^2 \hat{R} = \frac{1}{\mu_0 c} \left(\frac{q}{4\pi\epsilon_0 c^2} \right)^2 \frac{1}{R^2} \left(a^2 - \left(\hat{R} \cdot \vec{a} \right)^2 \right) \hat{R} \tag{2.8}$$

If we define θ as the angle between $\vec{R}$ and $\vec{a}$, then it's easy to see that the angular distribution of $\vec{S}$ is

$$\vec{S} = \frac{q}{4\pi\epsilon_0 c^2} \frac{a^2 sin^2\theta}{R^2} \hat{R} \tag{2.9}$$

The power is radiated in a donut, with no power being emitted in the acceleration direction (see figure 2-2a). The total emitted power is obtained by integrating equation 2.9 over all angles. The result is:

$$P = \frac{1}{4\pi\epsilon_0} \frac{2}{3} \frac{e^2 a^2}{c^3}. \tag{2.10}$$

Up to now we have only dealt with the electron rest frame, which is moving at velocity v, relative to the laboratory frame. Without any calculation one would expect a "build-up" of electromagnetic radiation in the direction of travel resulting in a Doppler effect. It is possible to re-derive equation 2.9 taking into account the effects of Doppler shifts to obtain the fraction of power, dP, radiated into the solid angle $d\Omega$ [36]:

$$\frac{dP}{d\Omega} = \frac{1}{4\pi\epsilon_0}\frac{e^2a^2}{4\pi c^3}\frac{\left[(1-\beta\cos\theta)^2 - (1-\beta^2)\sin^2\theta\cos^2\phi\right]}{(1-\beta\cos\theta)^5}, \tag{2.11}$$

where $\beta = v/c$, a and v point along the x and z axes respectively, θ is the angle between $\vec{R}$ and $\vec{a}$, and ϕ is the azimuthal angle. Figure 2-2b shows the angular distribution in the moving reference frame. There is still no power radiated along the acceleration direction, but the radiation donut has been stretched out so that it is sharply peaked in the forward direction. For a synchrotron, the radiation sweeps around much like a locomotive headlight. The peak radiation, ($\theta = 0$) is proportional to $\sim \gamma^6$, and the angular spread (which is calculated by finding the angles at which the radiated power is zero) in the limit $\beta \approx 1$, is $\sim 1/\gamma$ where $\gamma = 1/\sqrt{1-\beta^2}$ is the Lorentz factor. The total radiated power, which can either be obtained by integrating equation 2.11 over all angles (not so easy), or by Lorentz-transforming equation 2.10, which is done by replacing the acceleration, a, by the relativistic centripetal acceleration, $\gamma^2 v^2/r_c$, where r_c is radius of the electron path through the bending magnet. After this substitution, the relativistic expression for the total radiated power is

$$P = \frac{1}{4\pi\epsilon_0}\frac{2}{3}\frac{e^2v^4}{c^3r_c^2}\gamma^4 \approx \frac{1}{4\pi\epsilon_0}\frac{2}{3}\frac{e^2c}{r_c^2}\gamma^4 = 4.61\times10^{-20}\left[W\cdot m^2\right]\frac{\gamma^4}{r_c^2}. \tag{2.12}$$

Another important property is the energy spectrum of the radiated photons. While a derivation of the synchrotron radiation spectrum is quite lengthy and beyond the scope of this thesis, a good intuitive understanding can be obtained by first examining the non-relativistic case. For an observer in the plane of orbit at a distance much greater than the orbit radius, the particle will simply appear to oscillate back and forth with a frequency

$$\omega_c = \frac{eB}{m_e}, \tag{2.13}$$

where e is the electron charge, B is the applied magnetic field strength and m_e is the electron rest mass. In the plane of the orbit, the particle appears to be oscillating along a straight line with a sinusoidal acceleration. Since the radiated power is proportional to the acceleration, we can obtain the frequency spectrum by Fourier transforming the time dependent acceleration. The Fourier transform of a harmonic function is simply a delta function centered about the oscillation frequency, therefore the radiation spectrum from a non-relativistic orbit is simply $\omega_c/2\pi$. To obtain the relativistic expression, we first calculate the radiated frequency in the rest frame of the electron. Since the field lines are in the lab frame, length contraction will have the effect of increasing the field line density by a factor of γ, therefore, the radiated frequency will be $\gamma eB/2\pi m_e$. If we now transform to the laboratory frame, the Doppler effect will increase the frequency by an additional factor of γ, therefore the expression for the frequency from an electron moving in a synchrotron orbit is

$$\omega_c = \frac{3}{2}\frac{eB}{2\pi m_e}\gamma^2. \tag{2.14}$$

The factor of 3/2 is a factor which comes in as a result of a more rigorous derivation, which will be discussed in the next paragraph. It is more convenient to group the fundamental constants in equation 2.14 and write it in terms of the electron energy via $E_e = \gamma m_e c^2$. In this form, the synchrotron frequency is [35]

$$\hbar\omega_c = 0.665 E_e^2[GeV]B[T] \tag{2.15}$$

It turns out that equations 2.14 and 2.15 do not correctly describe the synchrotron radiation spectrum. Because a cyclotron is accelerated at a single frequency, the radiation spectrum is a delta function at that centered at the cyclotron frequency. However, the picture for a highly relativistic particle isn't quite as simple. A good way to understand is to visualize being an observer in the orbit plane tangent to the electron path. Because of the beaming effect of the relativistic electron, the radiation will appear as a very short pulse as the "head light" passes by the observer. In order to construct a pulse from Fourier components requires a large sum over many frequencies, thus the cyclotron radiation is spread out and creates a frequency dependent distribution. The exact form of the synchrotron radiation spectrum re-

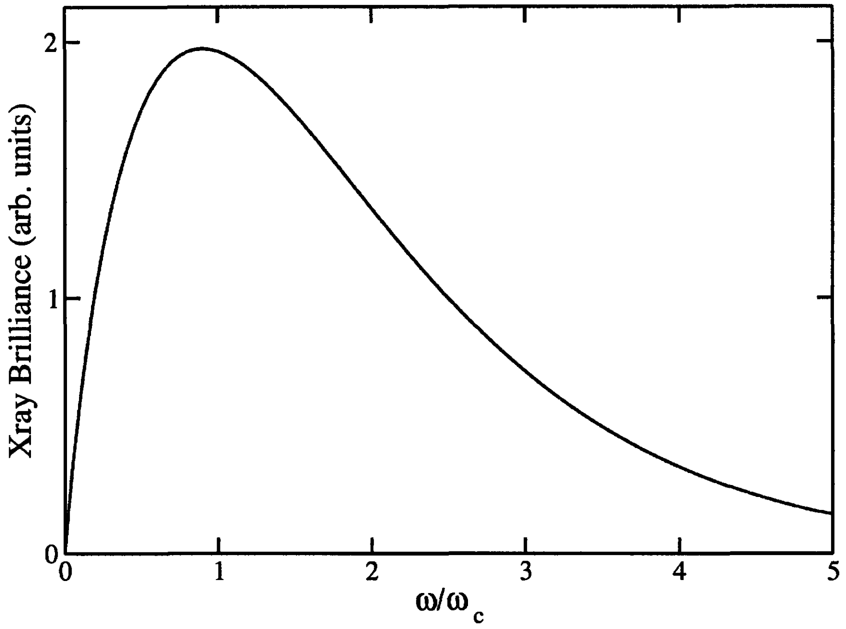

Figure 2-3: Shape of x-ray brilliance as a function of the frequency scaled by the characteristic synchrotron frequency ω_c. The exact numerical expression is [35] $1.327\times 10^{13}x^2K^2_{2/3}(x/2)$, where $K^2_{2/3}$ is a modified Bessel Function of the second kind.

quires calculating the Poynting flux using the Fourier transform of equation 2.7 in the relativistic limit. This is not an easy calculation, and doesn't help our intuition of synchrotron radiation much. An important result of this rigorous derivation is that the distribution is peaked around the characteristic synchrotron frequency ω_c given in equation 2.15. The spectrum is therefore often plotted as a function of $x = \omega/\omega_c$, shown in figure 2-3. In terms of x, the spectrum of figure 2-3 is a universal property of synchrotron radiation.

2.1.3 Bending Magnets

As mentioned earlier, the electron orbit is defined by a series of bending magnets placed around the storage ring. In the previous section we discussed how to calculate the angular distribution (equations 2.12, 2.11) and energy spectrum (equation 2.15) of the radiation emitted from the electrons as they pass through the bending magnet. These expressions can be used to to optimize a storage ring to emit photons in the x-ray regime with maximal brilliance. The important factor to maximize is γ, since both the peak intensity and angular divergence are optimal when γ is large. Therefore, a good synchrotron source is one in which the electron velocity is nearly the speed of light. To illustrate, we can insert some numbers from a real synchrotron into the expressions for the total power, angular distribution, and power spectrum to compare with the actual operating parameters. The National Synchrotron Light Source (NSLS), is a second generation synchrotron, with the bending magnet as the primary x-ray source. The operating parameters of the NSLS are freely available on the world wide web [37]. Each bending magnet is 2.7 m long, with a bending radius of 6.875 m. The electron energy is 2.8 GeV, which using $E \approx \gamma m_0 c^2$ for the relativistic energy [2], with $m_0 c^2 = 0.511\ MeV$ for an electron, we get $\gamma = 2800/.511 = 5480$. Using equation 2.11 the expected beam divergence would be $d\theta = 2/\gamma = 365\ \mu rad$ which is within the published range, $324 - 476\ \mu rad$.

The radiated power is a little trickier, since equation 2.12 gives the radiated power

---

[2] The quoted energy is actually the electron kinetic energy. The total relativistic energy is $E = kinetic\ energy + rest\ energy$, but since the electron rest energy is only 0.511 MeV, which is small compared to the 2.8 GeV, the total energy is approximately equal to the kinetic energy.

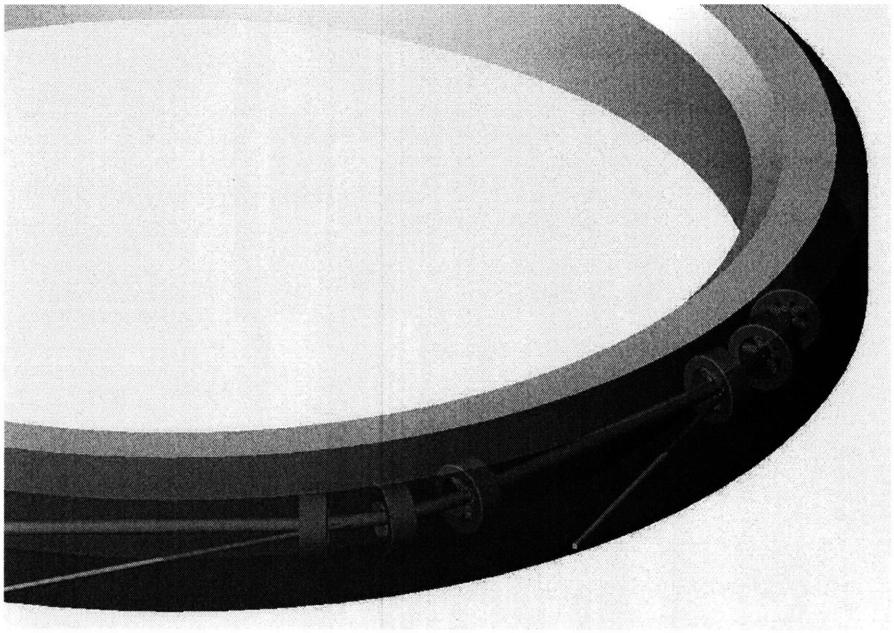

Figure 2-4: Schematic of a storage ring bending magnet. The "ring" actually consists of straight sections connected by bent sections where the bending magnets are located. The tangential tubes guide the radiated x-rays to the experimental setup.

per electron, which, using γ from above and $r_c = 6.875\ m$, is $8.798 \times 10^{-7}\ W/electron$. To calculate the total power radiated per bending magnet we need to find out the number of electrons which pass through the bending magnet in 1 second. This is simply the ring current times the time it takes for an electron to move the length of the bending magnet divided by the electron charge,

$$N_e = \frac{I}{e}\frac{dr}{r_s}T = \frac{0.25\,[A]}{1.6 \times 10^{-19}\,[C]}\frac{2.7\,[m]}{170.1\,[m]}5.672 \times 10^{-7}\,[s] = 1.407 \times 10^{11} electrons \tag{2.16}$$

where dr is the length of the bending magnet, r_s is the synchrotron radius, and T is the electron orbital period. Multiplying this result with the radiated power per electron yields 12.376 kW per bending magnet which compares to the published value of 12.375 kW.

Figure 2-4 shows a schematic drawing of a typical bending magnet light source setup. In this picture, the bending magnets are grouped in sets of three, which are separated by long, straight sections. The beam tubes stemming off tangentially at each magnet group serve to direct the radiation onto the beam optics which leading to the experimental setup. Various beamline components will be discussed in section 2.2.

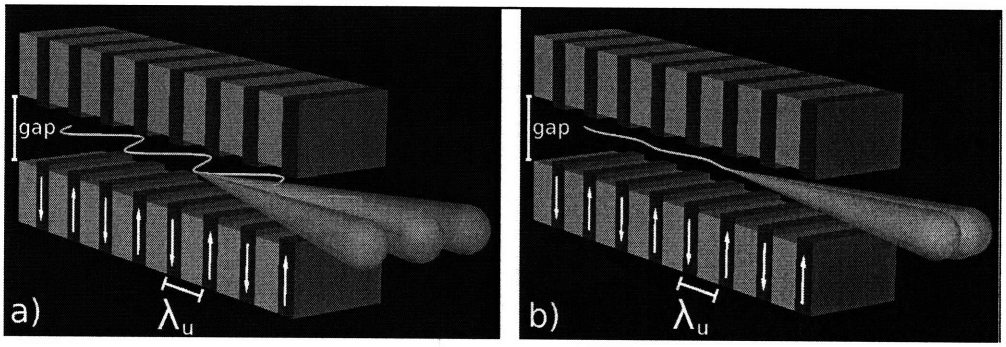

Figure 2-5: Schematic of the electron path and radiated power in a wiggler (a) and an undulator (b). In an undulator the oscillations are smaller thus more of the radiation cones overlap resulting in a narrower divergence of the forward radiation. The arrows indicate the magnet polarity.

2.1.4 Insertion Devices

The intensity from a bending magnet can be improved upon by placing several magnets of alternating polarity at equally spaced intervals along the electron path causing the electron to oscillate in a series of circular arcs, emitting radiation in a $1/\gamma$ cone as it passes around each arc (see figure 2-5). These so-called "insertion devices", are placed in the straight sections of the storage ring separating the bending magnets. The general type of insertion device, known as a wiggler, has a 2N enhancement of the emitted intensity, where N is the number of magnet poles. For a typical wiggler N is about 50, resulting in a factor of 100 enhancement of the intensity. To fully characterize the radiation from a wiggler, we need two additional parameters, the periodic spacing of the magnets, λ_u and the angular divergence of the radiation K/γ, where

$$K = \lambda_u e B_0 / 2\pi mc. \tag{2.17}$$

For a typical wiggler, K is about 20, so while there is a 2N intensity enhancement the angular divergence of the radiation is 20× that of a bending magnet. The K/γ divergence only applies to the oscillation plane. Perpendicular to the plane the divergence is still $\sim 1/\gamma$. This typically produces a long narrow beam at the sample position. This may or may not be optimal depending on the type of experiment and sample geometry. Typically, a small point like beam is desired, which can be achieved by focusing the beam in the oscillation plane.

The beam divergence in a wiggler is a result of superposing the $1/\gamma$ divergence cones from each bending magnet in the wiggler over a large divergence angle (figure 2-5a). If, however, the the magnets are spaced so that the electron undergoes small oscillations (on the scale of $1/\gamma$), that are in phase with the radiated photons, then there is a coherent addition of the electric field amplitudes, the square of which is proportional to the intensity. Because the oscillation amplitude is small, the radiation overlap from each magnet is much greater than for a general wiggler, resulting in a more collimated beam (figure 2-5b). These special types of wigglers form the class of insertion devices known as *undulators*. The angular divergence, α, of an undulator can be shown to be [35],

$$\alpha_{undulator} sim \frac{1}{\gamma\sqrt{N}} \sim \frac{1}{\sqrt{N}}\alpha_{bendingmagnet}. \tag{2.18}$$

Combining this with the additional N^2 gain in intensity results in a total $N^{5/2}$ gain in brilliance over bending magnet radiation. For an N of 50, the gain in brilliance is $\sim 1.7 \times 10^4$. Figure 2-6 compares the brilliance curves from different types of sources (taken from [38]). The undulator sources are labeled by Uλ_u. Comparing the APS U3.3cm with an APS bending magnet, we see a factor of $\sim 10^4$ better brilliance for the undulator, which is consistent with the estimate stated above. Because the coherent summing only works for one frequency determined by λ_u, undulators emit only a narrow band about the undulator frequency. This frequency can easily be estimated. For an observer on the undulator axis in a frame moving at the electron

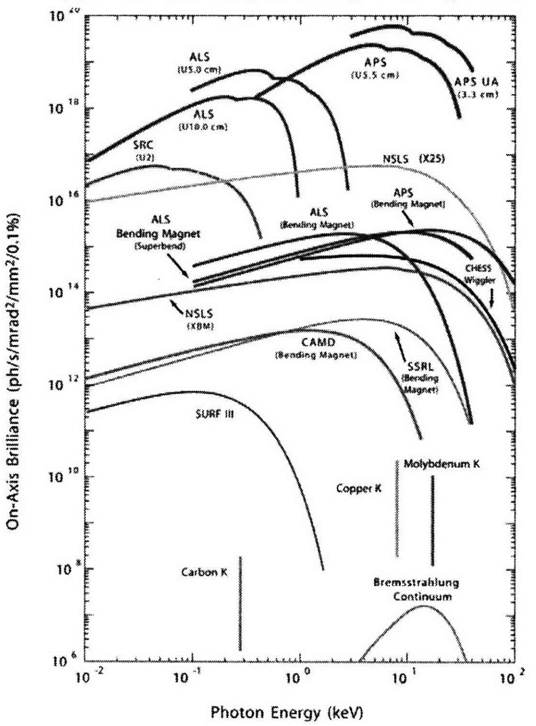
(http://www.aps.anl.gov/About/APS_Overview/Insertion_Devices/insertion_device2.html

Figure 2-6: Plot comparing the brilliance curves from various sources. Bending magnets are clearly labeled, and undulator sources are labeled with Uλ_u (taken from [38]).

velocity, $\sim c$, the electron appears to oscillate back and forth like a dipole. Since in this frame the undulator spacing, λ_u is length contracted, the oscillation frequency is $c\gamma/\lambda_u$. Just as in the example of the bending magnet, we gain an additional factor of $\gamma\sqrt{1+v/c} \approx 2\gamma$ due to the Doppler effect when we transform to the laboratory frame. Therefore the emitted photons have wavelength $\lambda_u/2\gamma^2$. To first order this is the correct wavelength, but a more detailed analysis will show that there are corrections [35]. The full expression for the emitted wavelength at small excursion angles θ and ψ on and off axis respectively is [39]

$$\lambda = \frac{\lambda_u}{2\gamma^2}\left[1 + \frac{K^2}{2} + \gamma^2\left(\theta^2 + \psi^2\right)\right] \tag{2.19}$$

Since K is proportional to B_o (equation 2.17), λ can be continuously varied by changing the gap between the poles (see figure 2-5).

Undulator physics is a stand-alone subject, with numerous capabilities for x-ray generation. In this work only the important details have been covered. For additional undulator applications, see reference [35], or search the web for "insertion devices" to access the many articles available. Currently the undulator is the most advanced source of hard x-rays available. While undulator radiation is spatially coherent, temporally, it is still incoherent. The next step in x-ray generation is the so-called Free Electron Laser (FEL), which are predicted to generate fully space and time coherent x-rays with a brilliance orders of magnitude greater than current undulator sources. Currently Stanford has a FEL operating in the far infrared. The reader is directed to http://www.stanford.edu/group/FEL/ for further details.

2.2 Beam Line Components

In section 2.1.2 the details of how to generate x-ray radiation from a synchrotron storage ring were discussed. Typically between the x-ray source and the sample being measured is about 30m or so of beamline filled with various components to optimize the beam at the sample position for the experiment at hand. Figure 2-7 highlights the

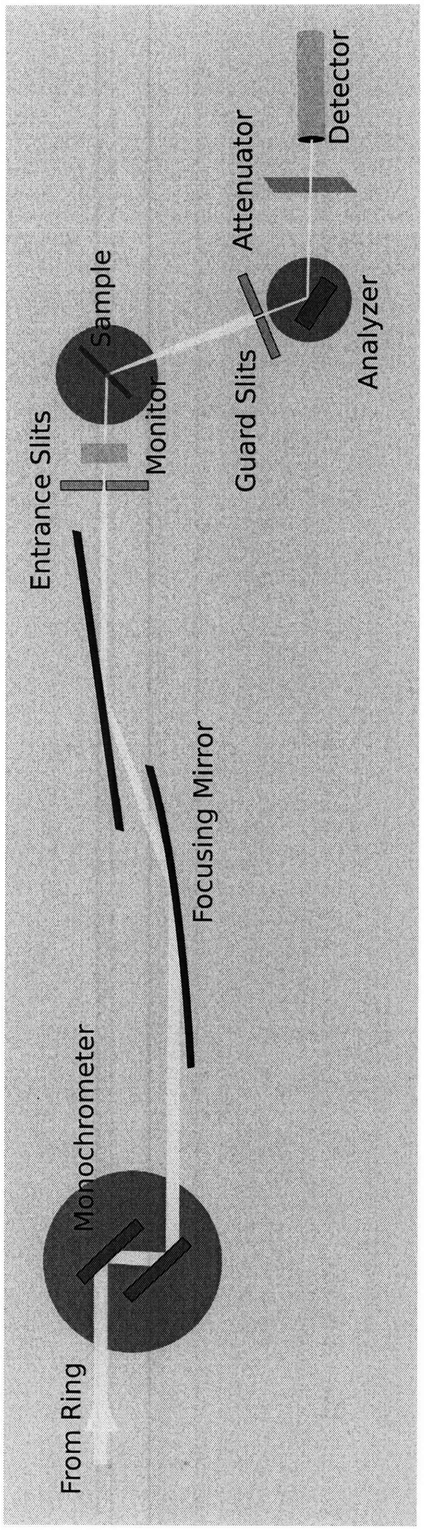

Figure 2-7: Schematic diagram showing the important components of a typical synchrotron single crystal x-ray diffraction experiment.

important components making up a beamline optimized for single crystal diffraction.

2.2.1 Monochromator

The bandwidth of radiation from a bending magnet or insertion device is quite broad, from the point of view of diffraction, where, in the ideal case, a single wavelength is desired. To achieve this requires the use of a monochromator. Typically in optics, diffraction gratings are used to monochromate beams. So too is the case for x-rays, but because of the wavelength, the best diffraction grating is a high quality single crystal. The type of material used in a monochromator depends on the application, but materials widely used due to their abundance and high quality are silicon, germanium, and diamond.

The energy resolution of a monochromator can be calculated by differentiating Bragg's Law (see section 2.3)

$$\delta\lambda = 2(\delta d \sin\theta + d\cos\theta\delta\theta). \tag{2.20}$$

Dividing both sides by $\lambda = 2d\sin\theta$,

$$\frac{\delta\lambda}{\lambda} \propto \frac{\delta E}{E} = \frac{\delta d}{d} + \delta\theta\cot\theta, \tag{2.21}$$

where E is the incident energy, δE is the energy resolution, δd is the deviation of the Bragg plane spacing about the average value d, θ is the scattering angle, and $\delta\theta$ is the angular acceptance. Since the manufacture of nearly perfect single crystal monochromators is possible ($\delta d/d < 10^{-7}$), the term which defines the energy resolution is the angular term $\delta\theta\cot\theta$. The angular acceptance $\delta\theta$ is typically that of the beam divergence, which for a bending magnet is $\sim$1 mrad, and for an undulator is $\sim 1\mu$rad. The function $\cot(\theta \rightarrow 0) \rightarrow \infty$, and $\cot(\theta = 90^o) = 0$, thus higher Bragg angles will achieve greater energy resolution. Typical values for $\frac{\delta E}{E}$ for a synchrotron monochromator are $10^{-4} - 10^{-4}$. meaning typical monochromatic beams have a bandwidth on the order of $\approx$ 1 eV. Monochromator design will be discussed in more detail in section

2.6, when we see how to achieve meV resolution.

2.2.2 Beam Focusing

The high intensity and fine Q-resolution of synchrotron x-rays requires as well high quality samples, as any imperfections will be detected. Because homogeneity is easier to maintain on small length scales, often the best x-ray crystals are tens of microns in dimension. Since the beam is between $1-2\ mm$, a lot of photons will not participate in scattering unless the beam is focused to nearly the sample size. In the visible regime this is done with lenses and parabolic mirrors. The same could be done with x-rays, but it isn't as straight forward. To understand why, we can examine the response of a metal to a rapidly oscillating electric field, like an incident light beam.

From classical electrodynamics in matter, metals should have high reflectivity, because they are good conductors. However, the basic assumption for this derivation is that the free charge dissipates "quickly", so that the divergence of the electric field has $\nabla \cdot \vec{E} = 0$. For an electric field oscillating with frequency ω, this means that the time scale, τ, for the free charge to dissipate is less than $1/\omega$. What happens however, when $1/\omega \leq \tau$? If this is the case, then the free electrons are "fixed" relative to the electric field, and the light will penetrate the metal with a certain refractive index, just as for non-conducting media. In a free electron gas, which is a good approximation for metals, the frequency characterizing the time scale for electron relaxation is the plasma frequency, ω_p, which is defined as [10]

$$\omega_p = \sqrt{\frac{ne^2}{\epsilon_0 m_e}}, \tag{2.22}$$

where n is the number of free electrons per unit volume, e is the electron charge, ϵ_0 is the permittivity of free space, and m_e is the electron mass. Most metals have plasma frequencies on the order of $\hbar\omega_p = 20\ eV$ [10]. Visible light has an energy of about 1 eV, which explains why most metals are good reflectors. X-rays have an energy on the order of keV, which is much greater than the plasma frequency, so they definitely fall in the "refractive regime". In this regime, the index of refraction $n(\omega)$ is given

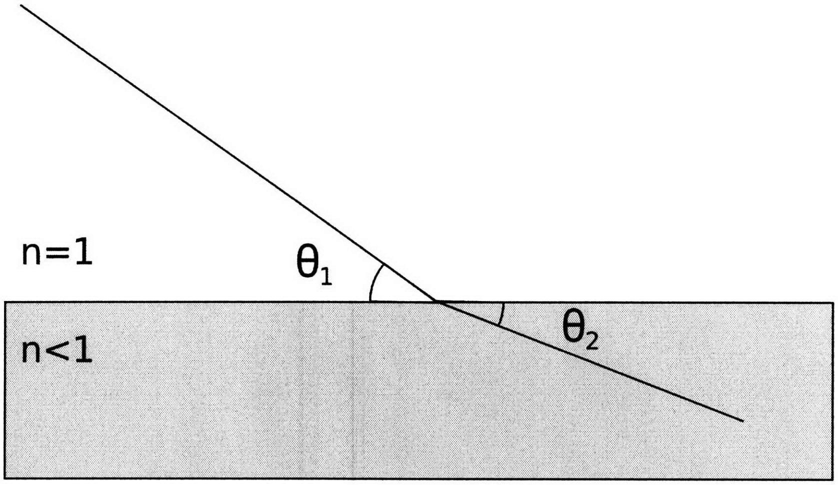

Figure 2-8: Diagram showing the refraction of x-rays passing from air with refractive index, $n = 1$, into a metal with $n < 1$.

by [36]

$$n(\omega) = \sqrt{1 - \left(\frac{\omega_p}{\omega}\right)^2}. \tag{2.23}$$

It is important to note that for $\omega > \omega_p$, $n(\omega)$, is less than 1. It is now possible to estimate the refraction in a typical metal for x-rays. In Aluminum, equation 2.22 gives, $\hbar\omega_p = 15.78\ eV$. Typically the x-ray energy used for single crystal diffraction is 4-40 keV, so we can take $\omega_p/\omega = .001$, which means $n(\omega) = .9999995$. Using Snell's law,

$$n_1 \cos\theta_1 = n_2 \cos\theta_2, \tag{2.24}$$

with θ as the angle from the interface, and refractive indices $n_1 = 1$ and $n_2 = n(\omega)$ for air and the metal respectively, we find that the light is only refracted by $\sim 10^{-5}$ degrees. Although it is possible to construct a lens which would focus x-rays, the focal length is too long to be feasible for use in a synchrotron beamline. Since the plasma frequency is proportional to the number of free electrons, it is possible to use a different metal like gold or lead, but these then attenuate the beam quite strongly.

A better method for focusing is to construct toroidal mirrors (to focus both vertically and horizontally) which use the less than unity refractive index to have almost 100% reflectance. This works because air has a refractive index of 1, thus the x-rays actually travel slower in air than in metal, meaning the refracted angle is less than the incident angle (see figure 2-8). When this happens it is possible to have an incident angle below which there are no longer any transmitted x-rays, resulting in total reflection. This is completely analogous to visible light passing from water or glass into air. This critical angle, θ_{cr} can be calculated by setting $\theta_2 = 0$ in equation 2.24.

Since we know the refraction is small for x-rays, we also know that the θ_{cr} will also be small, therefore we can Taylor expand $\cos\theta_{cr}$ to get $n_2 \approx 1 - \theta_{cr}^2/2$. If we also expand the right hand side of 2.23, we get $n \approx 1 - (\omega_p/\omega)^2/2$. Substituting this in for the approximate n_2, we get that

$$\theta_{cr} \approx \frac{\omega_p}{\omega} = 37.132 \left[eV \cdot \text{Å}^{3/2}\right] \frac{\sqrt{n}}{\hbar\omega} \tag{2.25}$$

For our aluminum example, θ_{cr} turns out to be $\sim .06^o$. To focus a 1 mm beam would require a mirror of about 1 m. Because of cost, it is desirable to have θ_{cr} as large as possible allowing shorter mirrors. Therefore focusing mirrors are most often coated in lead or gold to increase the index of refraction.

Typically the last component upstream of the diffractometer is a set of adjustable slits, which because of their position, are referred to as the "incident slits". The incident slits not only serve to cut out stray and divergent photons from the incoming beam, but also provide a reference for the beam position relative to the diffractometer. If any of the upstream optics moves, it is necessary only to steer the beam back through the incident slits to regain the proper alignment.

2.2.3 Single Crystal Diffractometer

As mentioned in the previous paragraph, the experimental apparatus typically follows immediately after the incident slits. Since we are discussing a beamline optimized for single crystal diffraction, it seems appropriate to discuss the basic design a nd operation of a single crystal diffractometer. A typical synchrotron x-ray diffractometer is shown in figure 2-9. There are four angles which can be controlled the scattering angle (2θ), two orthogonal tilting angles (θ,χ), and an additional rotation of the sample on top of the χ-axis, ϕ. These rotations are illustrated in figure 2-9. Diffractometers which have the capability of moving these four angles are called 4-circle diffractometers. The definitions of 2θ, θ, χ, and ϕ are somewhat arbitrary, but the convention used at most beamlines is that of Busing and Levy [40], whose published methods to calculate reciprocal space positions from the Eulerian angles listed above are standard in modern x-ray diffraction. The so-called "circles" of a diffractometer are controlled by precision stepping motors, with microradian resolution. The motors are then interfaced with a central computer which has some sort of software which interfaces with the motor controllers. The software used in this work, the use of which is widespread in the synchrotron x-ray community, is SPEC a product of *Certif Scientific Software.* In SPEC, it is possible to associate a set of Eulerian angles with two different reciprocal lattice points. From these two orientation vectors, the software can then calculated the angles required to reach any arbitrary point in reciprocal space. This is ideal for doing solid state physics experiments where all of the relevant theory is discussed in terms of reciprocal space. SPEC allows the operator to think

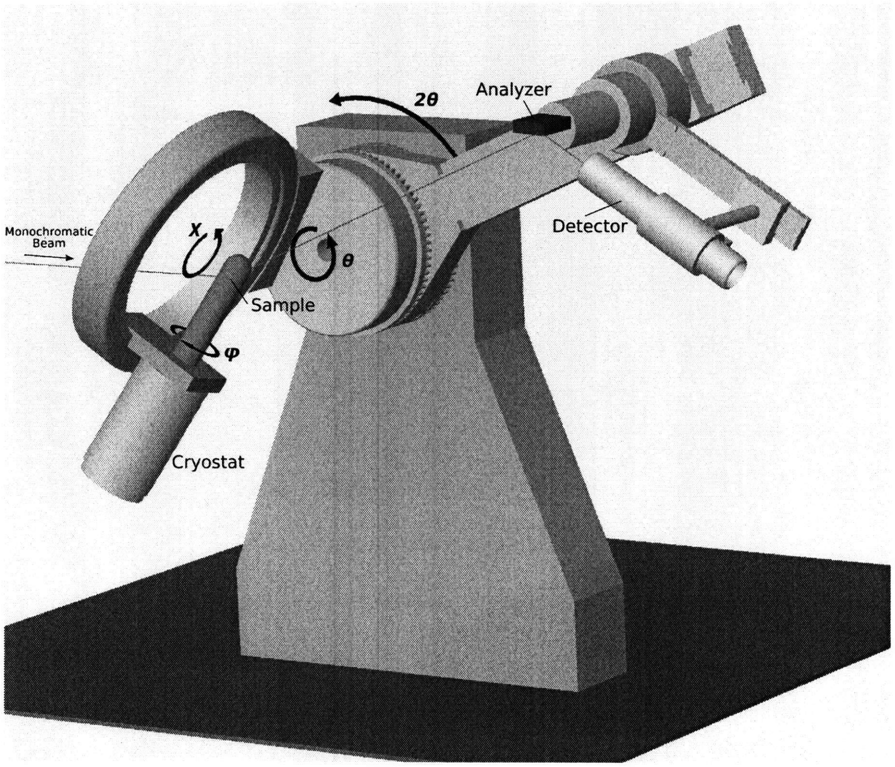

Figure 2-9: Typical synchrotron x-ray scattering diffractometer.

in reciprocal space, thus greatly simplifying the experiment.

The next important component in figures 2-7 and 2-9 is the analyzer. Like the monochromator, an analyzer uses a fundamental Bragg reflection from a high quality Si or Ge single crystal to select out the final energy. An analyzer is not necessary, but desirable for high Q-resolution and low background. If no analyzer is used, then the detector is placed at the analyzer position, and the Q-resolution and background are defined by the detector aperture, which is usually varied by a set of adjustable slits place just upstream of the detector, appropriately named the "detector slits".

2.2.4 X-ray Detectors

For x-rays, two different types of detectors are typically used, ionization or ion chambers and scintillation counters. An ion chamber consists of an anode and a cathode separated by a chamber of air. When the incident x-rays ionize the gas, the ions are collected by the electrodes, resulting in a current, which can then be measured and scaled to the proper units. Ion chambers are not very sensitive detectors, but do have the advantage that they can withstand arbitrarily high beam flux. For this reason they are used as a monitor, which is a detector placed in the main beam just after the incident slits to monitor the incident intensity. This allows all of the data to be placed on the same intensity scale by normalizing to the incident flux. The use of a monitor is especially important at the NSLS where the storage ring current decays over a 12 hour period, resulting in a change in beam intensity by several factors. At the APS, the storage ring runs in top-off mode, maintaining a relatively stable, constant current for weeks at a time.

Detecting the beam scattered from the sample requires more sensitive detection. A commonly used detector is the scintillation counter. In a scintillation counter ionizing radiation, like x-rays, strike a phosphorescent medium, which fluoresces when ionized, emitting visible/UV photons. These photons are then amplified by a photomultiplier tube connected to an electronic amplifier which sends a signal to various electronics to transform the signal into meaningful units. Scintillation counters have the advantage that they are sensitive to a small number of incident photons, but the response of these counters is only linear for a limited range on the low intensity end. Above this threshold, the detector becomes "saturated", and the signal output may not be an accurate indication of the incident intensity. In the extreme intensity limit, these detectors can burn out. Because of the limited linearity range for scintillation counters, often a tunable attenuation is required just before the entrance to the detector. The attenuator is usually a series of metal foils with thicknesses on the order of the x-ray attenuation length.

2.3 Single Crystal Diffraction

Bragg's Law

Just one year after Laue and his collaborators received the Nobel prize for their work on x-ray single crystal diffraction, Sir William Henry and William Lawrence Bragg received the Nobel prize for developing a quantitative understanding of x-ray diffraction known as Bragg's Law:

$$\lambda = 2d \sin\theta, \tag{2.26}$$

where θ, d, and λ are defined in figure 2-10. The easiest way to understand Bragg's law is to examine a monochromatic phase coherent beam incident on a periodic array of atoms. For certain crystal orientations, the atoms form planes spaced a distance d

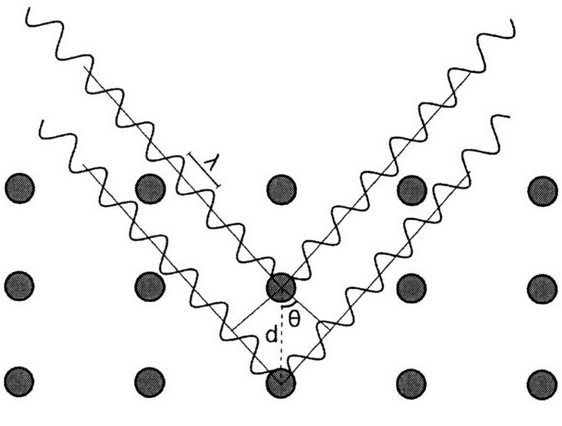

Figure 2-10: Schematic of Bragg scattering in a periodic array of atoms.

apart. For simplicity we can simplify to two photons incident on two planes. Photon 1 will scatter off of plane 1, and photon 2 will scatter from plane 2, a distance d away from plane 1. The geometry of this example is shown in figure 2-10. Since the beam is phase coherent, the photons will remain in phase until they are scattered. If we now examine the phases of the scattered photons we will see that the phase of photon2 lags that of photon 1 by an amount $2d\sin\theta$. The observed intensity from the two photons will be the coherent sum of the amplitudes. The expectation is that the scattered intensity should be maximal if both scattered photons are in phase, and 0 if they are completely out of phase. This leads to the criterium $2d\sin\theta = \lambda$ for constructive interference.

If we now expand this example to $\sim 10^{23}$ photons on 10^23 planes, then the coherent sum will select only those photons which are *exactly* in phase. given by the Bragg condition. The crux of our argument for this example was a phase coherent incident beam. The idea here is that for any real beam, some fraction of the photons will be in phase, and will therefore diffract. Despite its simplicity, equation 2.26 remains the fundamental equation used in diffraction experiments.

2.3.1 Reciprocal Space

There is an alternative formulation of Bragg's law based on the coherent summing of x-rays scattered from individual atoms. Let's assume an x-ray with electric field given $\vec{E}_i(\vec{r}) = \vec{E}_o \exp(i\vec{k}_i \cdot \vec{r})$ is incident on atoms 1 and 2 located at lattice points $\vec{R}_1$ and $\vec{R}_2$, shown in figure 2-11. For this case, the phase differences will be given by the

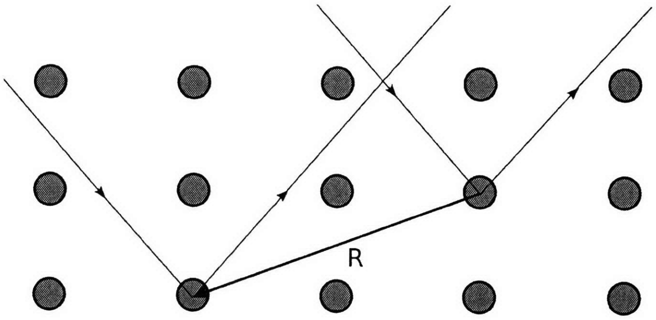

Figure 2-11: Diagram showing x-rays incident on two atoms separated by $\vec{R}$.

projection of the wavevector on the difference in atomic spacing, $\vec{R} \equiv \vec{R}_2 - \vec{R}_1$. In the example illustrated by figure 2-11 the phase of the radiation incident on atom 1 will lead that incident on atom 2 by $\vec{k}_i \cdot \vec{R}$. The phase of the scattered radiation from 1 will lag the scattered radiation from 2 by an amount $\vec{k}_f \cdot \vec{R}$ leading to a total phase difference of $(\vec{k}_i - \vec{k}_f) \cdot \vec{R} \equiv \vec{Q} \cdot \vec{R}$. The vector $\vec{Q}$ is the momentum transfer. From the relative directions of of $\vec{k}_i$ and $\vec{k}_f$ it is not difficult to see that $\vec{Q}$ points perpendicular to the scattering planes. Putting this phase shift into wave form, we have

$$\vec{E}_o e^{i\vec{Q}\cdot\vec{R}} \tag{2.27}$$

If we now sum this over N atoms in a periodic crystal,

$$\vec{E} \propto \sum_R e^{i\vec{Q}\cdot\vec{R}}, \tag{2.28}$$

which mathematically, is simply the Fourier transform of the atomic lattice. In general $\vec{Q} \cdot \vec{R}$ can be anything, but it's not hard to imagine that the special case of $\vec{Q} \cdot \vec{R} = 2\pi n$ will dominate, since the sum will be of the order $N \sim 10^{23}$, whereas when summing all of the other phases should result in some cancellation resulting in a much smaller sum over 10^{23} terms. This, then gives the scattering criterium:

$$e^{i\vec{Q}\cdot\vec{R}} = 1. \tag{2.29}$$

This is true for any arbitrarily spaced atoms. If we now expand this example to an N atom periodic lattice, then $\vec{R}$ will only take on discrete values consistent with integer multiples of the lattice. If we define the smallest periodic unit within the cell by the vectors $\hat{a}$, $\hat{b}$, and $\hat{c}$, then $\vec{R}$ will be a given by

$$\vec{R} = n_1\hat{a}_1 + n_2\hat{a}_2 + n_3\hat{a}_3, \tag{2.30}$$

where n_1, n_2, and n_3 are integers. A lattice consisting of identical atoms located at positions given by $\vec{R}$ is known as a Bravais lattice. Equation 2.29 together with 2.30

requires that $\vec{Q}$ be of the form[41]

$$\vec{Q} = h\hat{b}_1 + k\hat{b}_2 + l\hat{b}_3, \tag{2.31}$$

which, like $\vec{R}$ has the form of a periodic lattice. In fact it can be shown that if $\vec{R}$ is a Bravais lattice then $\vec{Q}$ is also a Bravais lattice[41]. Following the procedure we used to get to equation 2.31, we see that each point in $\vec{Q}$ corresponds to the Fourier transform of a plane wave having the periodicity of the real space lattice. For this reason the lattice made up of all possible $\vec{Q}$ points is referred to as the *reciprocal* lattice. The reciprocal lattice unit vectors $\vec{b_i}$ are related to the real lattice unit vectors $\vec{a}_i$ by the cyclic permutations of the following

$$\vec{b_1} = 2\pi\frac{\vec{a}_1 \times \vec{a}_2}{\vec{a}_1 \cdot (\vec{a}_2 \times \vec{a}_3)}. \tag{2.32}$$

If the crystal structure is known, then the reciprocal lattice vectors can be calculated using equation 2.32. To simplify notation, $\vec{Q}$ is truncated to the indices, $Q = (h, k, l)$, which implies equation 2.31. In this notation, the unit are is the *reciprocal lattice unit.*

2.3.2 Atomic Form Factor

Up to this point the electron has been treated as a point charge which has an isotropic interaction with incident x-rays. However, in a solid consisting of atoms, the electrons are distributed into orbitals, which are also arranged about the nucleus. This results in a non-uniform electron density, which has to be taken into account for an accurate measure of the scattered intensity. The way to obtain this information is analogous to the scattering intensity from a periodic array of atoms, as discussed in section 2.3.1. Let's consider a charge distribution $\rho(\vec{r})$. From equation 2.40, we know that the scattered intensity is proportional to the charge, which in this case is a small element $\rho(\vec{r})d\vec{r}$, located at $\vec{r}$. From section 2.3.1 we know that the phase picked up is $e^{i\vec{Q}\cdot\vec{r}}$. So the intensity scattered from this small charge element is $\sim \rho(\vec{r})e^{i\vec{Q}\cdot\vec{r}}d\vec{r}$, Summing over all $\vec{r}$ we get

$$f^0(\vec{Q}) = \int d\vec{r}\rho(\vec{r})e^{i\vec{Q}\cdot\vec{r}} \tag{2.33}$$

Because $\rho(\vec{r})$ is a complicated function the f^0 is non-trivial to calculate. However, it is clear that for $Q = 0$ the phase factor is 1 (i.e. all scattering is in-phase), therefore equation 2.33 becomes

$$f^0(\vec{Q} = 0) = \int d\vec{r}\rho(\vec{r}) = Z \tag{2.34}$$

where Z is the number of electrons. As Q increases the phase factor becomes non-zero, and therefore phase cancellation will decrease the scattered intensity. The exact form of this behavior is quite involved and has been the topic of many published articles. The calculation usually involves performing some iterative self consistent method on a numerical potential model. The results for various models have been tabulated. One of the more widely accepted models, based on a relativistic Hartree-Fock interaction, was developed by D. Cromer and J. Mann in 1968[42]. They summarized their tabulation by fitting the numerical results to the equation

$$f^0\left(Q\right) = \sum_{i=1}^{4} a_i e^{-b_i\left(\frac{Q}{4\pi}\right)^2} + c. \tag{2.35}$$

where the values a_i, b_i, c were then tabulated for all elements up to Lr. Figure 2-12 shows plots of equation 2.35 for the elements Ti, O, and Cl. All of the above equations depend on the assumption of the scattering center being a perfect oscillating dipole with no damping, i.e., the charge is allowed to follow the oscillating field exactly. In general the primary interaction is with the electrons in the outer shells, so this is a good approximation. However, if the incident x-ray energy approaches the resonant energy levels of one of the core electrons, then those electrons are excited and take part in the scattering. They are more tightly bound than the outer electrons, and therefore do not obey the free oscillating dipole model. So called anomalous dispersion corrections must be added to take into account the dispersion(f') and dissipation (f'').

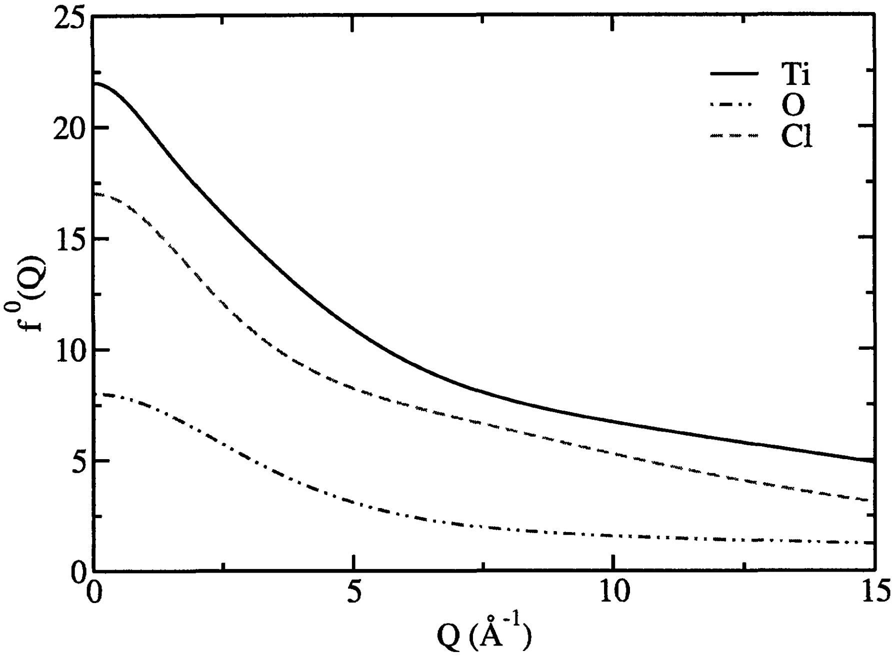

Figure 2-12: Cromer-Mann atomic form factor $f^0(Q)$ for Ti, O, and Cl.

The full atomic form factor is then

$$f\left(\vec{Q},\omega\right) = f^0(\vec{Q}) + f'(\omega) + f''(\omega), \tag{2.36}$$

where $\hbar\omega$ is the incident x-ray energy. Most x-ray experiments are performed away from the electron energy levels, (signified by absorption edges), therefore f^0 is sufficient to describe the atomic form factor. There are experiments where scattering near an absorption edge is desirable, then the anomalous dispersion corrections are necessary. In this work all scattering was performed away from the absorption edge, so we are only concerned with f^0, which from this point on will be written simply as f.

2.3.3 Bravais and General Lattice

In section 2.3.1, scattering from a Bravais lattice defined by equation 2.30 was discussed. While there are 14 different types of Bravais lattice, only a handful of materials crystallize into one of these 14 special lattice types. However, it is still possible to calculated the scattering intensity from a general lattice by breaking it into a Bravais lattice with a basis (see figure 2-13). Now we can use equation 2.30 to define the lattice, but we add the basis:

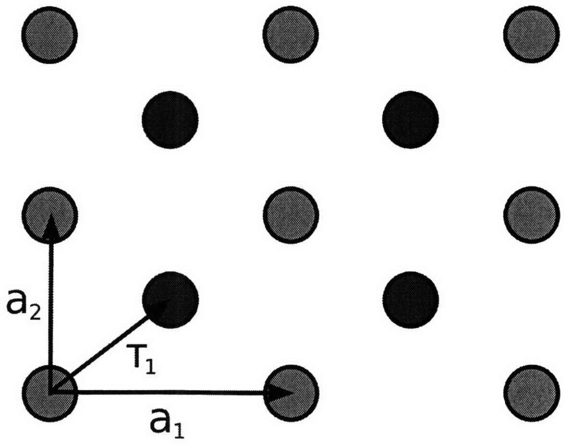

Figure 2-13: A general lattice consisting of a Bravais lattice with unit vectors a_i and a basis with unit vectors τ_i.

$$\vec{R}_i = \vec{R} + \vec{\tau}_i. \tag{2.37}$$

To find the reciprocal lattice of , we can follow the same procedure as in section 2.3.1, using $\vec{R}_i = \vec{R} + \vec{\tau}_i$

$$\sum_i f_i(\vec{Q}) e^{i\vec{Q}\cdot\vec{R}_i} = \sum_R \sum_i f_i(\vec{Q}) e^{i\vec{Q}\cdot(\vec{R}+\vec{\tau}_i)} = \sum_R e^{i\vec{Q}\cdot\vec{R}} \sum_i f_i(\vec{Q}) e^{i\vec{Q}\cdot\vec{\tau}_i}. \tag{2.38}$$

Where we define the structure factor

$$S(Q) = \sum_i f_i(\vec{Q}) e^{i\vec{Q}\cdot\vec{\tau}_i}. \tag{2.39}$$

Whereas the scattered intensity is the same for each $\vec{Q}$ in a Bravais lattice (neglecting all other intensity dependent effects), the structure factor introduces a $\vec{Q}$ dependence for the general lattice. In some crystals, at certain Q-points, the phases exactly cancel, resulting in a structure factor $S(\vec{Q}) = 0$. The set of Bragg reflections with a non-zero structure factor form a set of allowed reflections, which aid in defining the crystal structure. While in general the atoms forming the basis can be located at random positions within the unit cell, there is usually some sort of symmetry to the atomic arrangement. General lattices can then be grouped by the Bravais lattice and symmetry operations of the basis, known as the space group. Characterizing and categorizing of the crystal structures for almost all known compounds has been the work of crystallographers over the 20th century, so that now it is possible to find the tabulated structural characterization of a wide variety of compounds.

2.4 X-ray Scattering Intensity

While having knowledge of the Bravais lattice and structure factor in principle allows one to completely solve an unknown crystal structure, there are other non-structure related factors affecting the x-ray scattering intensity which must be taken into account. While it is impossible to exactly calculate all of these contributions, there are only a handful of dominant effects, which when accounted for can provide a nearly ideal situation for structural refinement. Some of these effects are quite involved mathematically. So that we don't lose sight of the underlying physics, these corrections will be motivated through intuitive examples, rather than mathematical procedure. For a good overview of the mathematics involved, the reader is directed to [43].

2.4.1 Polarization Factor

The first contribution comes from the fact that in the scattering process electrons are being excited by the oscillating electric field. The electrons in turn oscillate and emit radiation in the typical dipole pattern. If the incident beam is polarized, as we saw was the case for an undulator source in section 2.1.4, then the scattered beam will also be polarized. From electrodynamics, the power radiated from a dipole is (SI)

$$P(\phi, \psi) = \left(\frac{\mu_0 p_0^2 \omega^4}{32\pi^2 c}\right) \frac{\cos^2 \psi}{r^2} \hat{r}, \tag{2.40}$$

where $p_0 = es$ is the magnitude of the dipole moment, μ_0 is the permeability of free space, ω is the oscillation frequency and ϕ and ψ are the scattering angles out of and in the polarization plane respectively (see figure 2-14). It is important to point out that equation 2.40 is independent of ϕ, and equals zero when $\psi = 90^o$. This is because the scattered beam cannot have any component of the oscillating field in the propagation direction. For scattering out of the polarization plane the oscillating field is perpendicular to the propagation direction for all angles, therefore the polarization factor is simply $P(\phi) = 1$. For unpolarized sources, such as a rotating anode, it is necessary to take a statistical average over all angles ϕ, ψ. The result is $(1+\cos^2\psi)/2$. This illustrates further the advantage of an undulator source over a rotating anode. For scattering out of the polarization plane, one can scatter at any ψ with no effect on the intensity. In summary, the polarization factor is:

$$I \sim P(\phi, \psi) \propto \begin{cases} \cos^2\psi & \text{in polarization plane} \\ 1 & \text{out of polarization plane} \\ \frac{1+\cos^2\psi}{2} & \text{unpolarized} \end{cases} \tag{2.41}$$

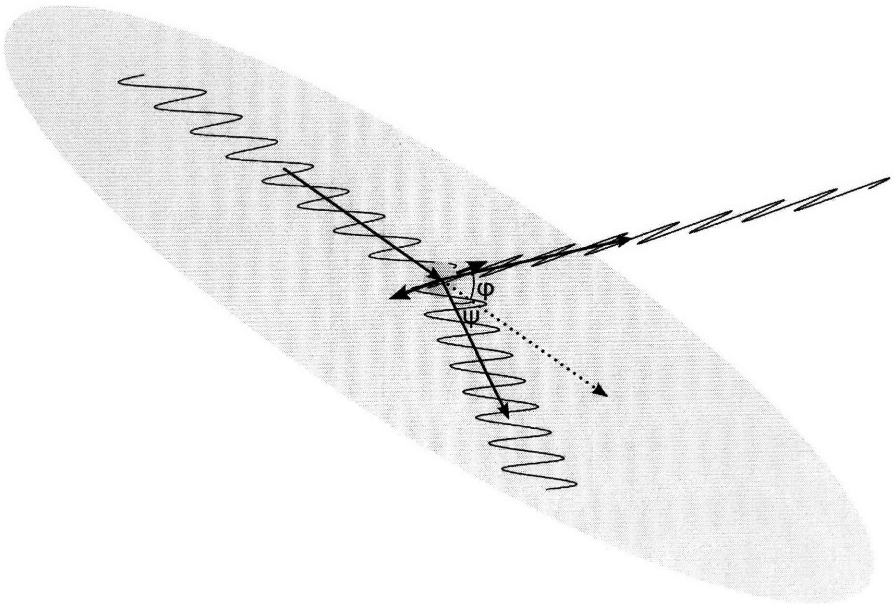

Figure 2-14: Polarized x-rays incident on a single electron. The electron oscillates with the electric field and as a result emits light polarized parallel to the incident beam.

2.4.2 Lorentz Factor

There is additional attenuation due to the facts that the beam is not completely monochromatic, and that crystals have a finite size. To illustrate these effects it is convenient to introduce a different scattering geometry representation, the Ewald construction, named for its innovator, Paul P. Ewald.

Ewald conceived a construction, shown in figure 2-15, where the incident and reflected wavevectors are plotted along with the possible reciprocal lattice points. For elastic scattering, the incident and final wavevector magnitudes are fixed, but there is a solid angle of 4π accessible to the two vectors. These angles of possible scattering geometries for a given incident energy make up the Ewald Sphere. In the 2-d drawing of figure 2-15, the Ewald Sphere is the circle drawn with the incident and final wave vectors as radii. Figure 2-15 shows the ideal case where the beam is perfectly monochromatic and the Bragg reflections are infinitesimally small points.

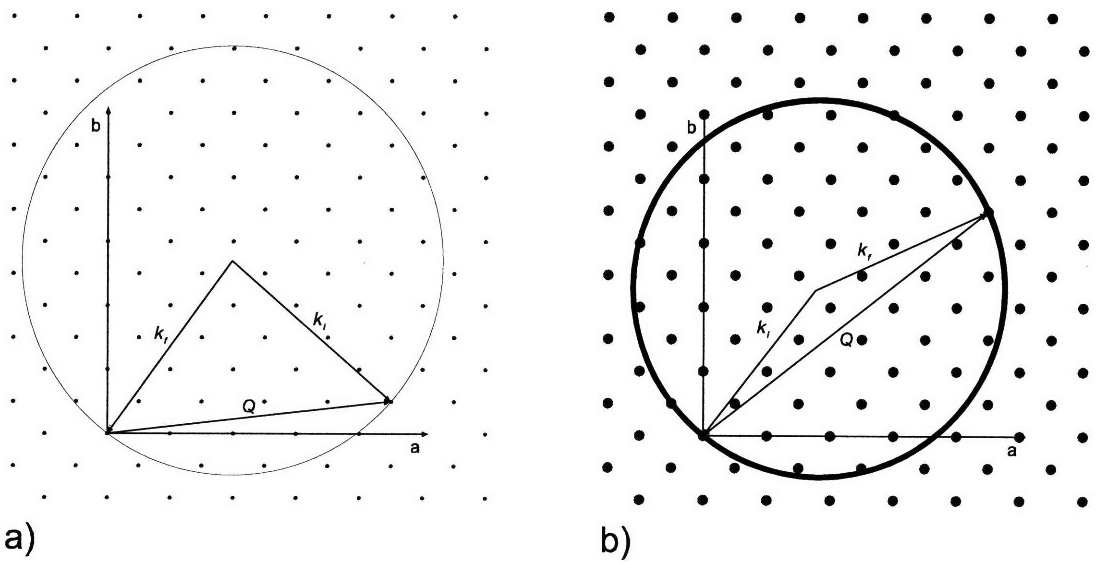

Figure 2-15: The scattering vectors k_i, k_f, and Q form the scattering triangle. For a given energy, there is a solid angle of 4π into which the scattering can occur, as illustrated by the 2D projection of the Ewald sphere in figure a). Figure b) illustrates the smearing effect of the finite crystal size on the reciprocal lattice points, as well as the broadening of the Ewald sphere due to slight non-monochromicity of the beam. Also illustrated is the difference in path length for a reciprocal lattice point through the Ewald sphere for scans along two different $\vec{Q}$ directions.

Real x-ray beams are slightly non-monochromatic by an amount dE, therefore the sphere in figure 2-15 should be replaced by a shell of width dE. The Bragg points will also be smeared out by the finite crystal size effect.[3]

The finite shell width and point size are directly responsible for the Q-dependent intensity variation. This can be understood by examining how the Ewald sphere changes during when scanning one of the four angles defined in section 2.2.3. A transparent example is a scan along the scattering vector, Q, which in real space corresponds to scanning theta and two theta in such a way to keep the same set of Bragg planes in the scattering condition. Figures 2-15a,b illustrate the scattering geometry of two different Q-points. For the one in 2-15a, the Q-point is almost tangent to the sphere, therefore would continue to satisfy the scattering condition for a greater range in the Q-scan. On the other hand the Q-point in 2-15b will intersect the sphere almost normal to the surface therefore less time will be spent in the scattering condition. Experimentally, a peak is observed, the integrated intensity of which is the desired value. The peak width of the first Q-point will be broader than for the second resulting in a greater integrated intensity, for no other reason than the different scattering geometries. The first order correction for this effect is the so-called *Lorentz Factor*, which for a single crystal is $1/\sin 2\theta$, which tends to reduce the intensity of small Q reflections and do nothing to reflections at larger Q. Intuitively, this is what one would expect based on the simple example given above.

2.4.3 Debye Waller Factor

All of the formalism thus far is for T=0, where the atoms are frozen into a minimum energy configuration. For T¿0, thermal energy causes the atoms vibrate about the equilibrium position. Statistically, for a single measurement, the probability of finding an atom away from equilibrium is essentially 1, meaning that the atoms are randomly distributed in space. One must wonder, therefore, if any of the formalism based on

---

[3] It can be shown that the width of a Bragg peak described by equation 2.28 is proportional to $1/N$, where N is the number of unit cells. If $N = \inf$, then the Bragg peak is a perfect delta function[35].

a periodic lattice applies to real systems. It turns out that while for any given measurement the probability of finding the atom at the equilibrium position. x_0 is zero, the time averaged position is a distribution of width σ, peaked about $x - x_0$. As the temperature is decreased, σ decreased, until at $T = 0$, $\sigma = 0$, and the probability of finding the atom at x_0 is 1. This example illustrates that there is some temperature dependent factor influencing the scattered intensity, based on the thermal population of vibrational states. With detailed knowledge of the lattice dynamics, it is possible to calculate this factor, known as the Debye-Waller factor. For a rough idea of the functional form of this correction, we can assume a unit cell with a basis τ_i, displaced by u_j, $j = x, y, z$ indicates the direction of the vibrational displacement. The structure factor will have the form

$$\sum_i f(\vec{Q}) e^{i\vec{Q}\cdot(\tau_i + u_j)}. \tag{2.42}$$

From the above discussion, we know that at finite temperature, the instantaneous positions aren't so useful, but rather the thermal average,

$$\langle \sum_i f(\vec{Q}) e^{i\vec{Q}\cdot(\tau_i + u_j)} \rangle = S(\vec{Q}) \langle e^{i\vec{Q}\cdot\vec{u_j}} \rangle, \tag{2.43}$$

The term, $\langle e^{i\vec{Q}\cdot\vec{u_j}} \rangle \equiv e^{-W}$, is known as the the Debye-Waller factor, which quantifies the effect of thermal vibrations on the scattering intensity. The thermal average is worked out explicitly in [41]. The result is

$$W = \frac{\hbar G^2}{2M\omega}, \tag{2.44}$$

where M is the atomic mass, G is a reciprocal lattice vector and ω is the vibration frequency. Usually the Debye-Waller factor is very near one, especially for low temperatures, therefore it is usually neglected. For lighter atoms, especially Hydrogen, the Debye-Waller factor can change significantly, therefore, it must be accounted for when comparing high and low temperature scattering intensities.

2.4.4 Crystal Mosaic

Quite often a single crystal isn't easily realizable for all compounds. Instead The single crystals consist of tiny crystallites which are slightly misaligned with respect to each other. For a single crystal, once the scattering condition is satisfied by 2θ, rotating the sample about the 2θ axis (rocking curve) will result in a sharp peak observed at the detector. If we now take several single crystals and misalign them slightly, 2θ will still select the proper Bragg plane spacing, but rocking the sample will bring the Bragg planes for different crystallites into illumination resulting in several observed peaks over the rocking curve. If we now consider a large number of slightly misaligned crystallites, The peaks will merge together forming one broad peak in the angle scan. In crystals where the mosaic spread is greater than the spectrometer resolution, the Bragg peak will have a structure consisting of multiple small peaks, centered about the Bragg position. To obtain the total integrated intensity from such a crystal mosaic requires coarsening the resolution to capture the entire angular divergence of the scattered beam, then repeating the rocking curve. While it is possible to obtain reasonable intensity measurements from a crystal with a bad mosaic, it is optimal to have a crystal with a mosaic spread less than the resolution of the instrument.

2.4.5 Absorption

As discussed in section 2.2, X-rays are absorbed by materials as they pass through them. The attenuation of the beam intensity is exponential, having the form

$$I(x) = I_0 e^{-\frac{x}{l}}, \tag{2.45}$$

where l is the *attenuation length.* Since the electrons are primarily responsible for x-ray absorption, the attenuation length depends on the atomic number, and density of the atoms in the material. The attenuation length can be calculated as a function of incident energy with knowledge of these parameters, which can then be used to estimate the attenuation for different scattering angles (i.e. the path length through the sample as a function of scattering angle).

2.4.6 Multiple Scattering

In our discussion of Bragg scattering, we assumed that every photon entering the detector is scattered once. In actuality, photons incident on an atom will be scattered in all directions, but only those which satisfy 2.26 will be detected. However, it is also possible that a photon is scattered once in a specific direction where it can scatter a second time into the detector. Since each scattering event is elastic, the detector cannot quantify the number of time s photon has been scattered. While extremely unlike, multiple scattering events are a real consideration with modern high flux x-ray beams. Multiple scattering can be predicted, however, which can be illustrated using the Ewald construction introduced earlier to discuss the Lorenz factor (figure 2-16b. If two allowed reciprocal lattice points coincide with the Ewald sphere simultaneously, and if the two points are separated by an allowed Q-vectors, then a multiple scattering event occurs.

To measure a multiple scattering peak, one can either scan the incident energy,

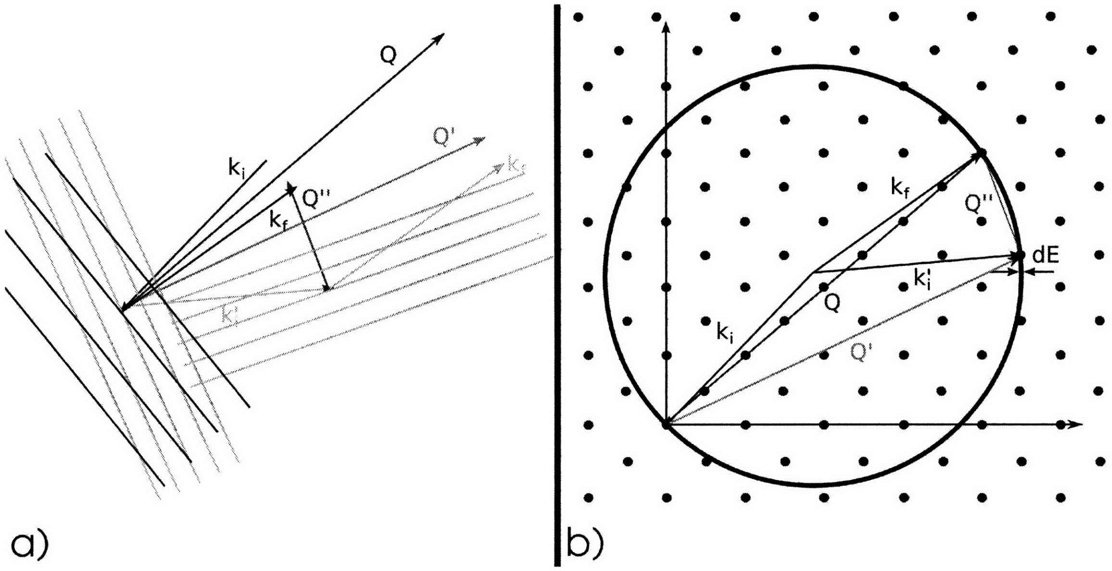

Figure 2-16: Visualization of multiple scattering using Bragg planes (a), and the Ewald construction (b). The vectors $\vec{k_i}$, and $\vec{k_f}$ are the incident and final vectors which satisfy the scattering condition $\vec{Q}$. However, photons can also be scattered into $\vec{k_i'}$ with momentum transfer $\vec{Q'}$ which also satisfies the scattering condition, since $\vec{Q'}$ falls on the Ewald sphere. This process will be detected at $\vec{k_f}$ if $\vec{Q'}$ and $\vec{Q''} \equiv \vec{Q} - \vec{Q'}$ are allowed reflections.

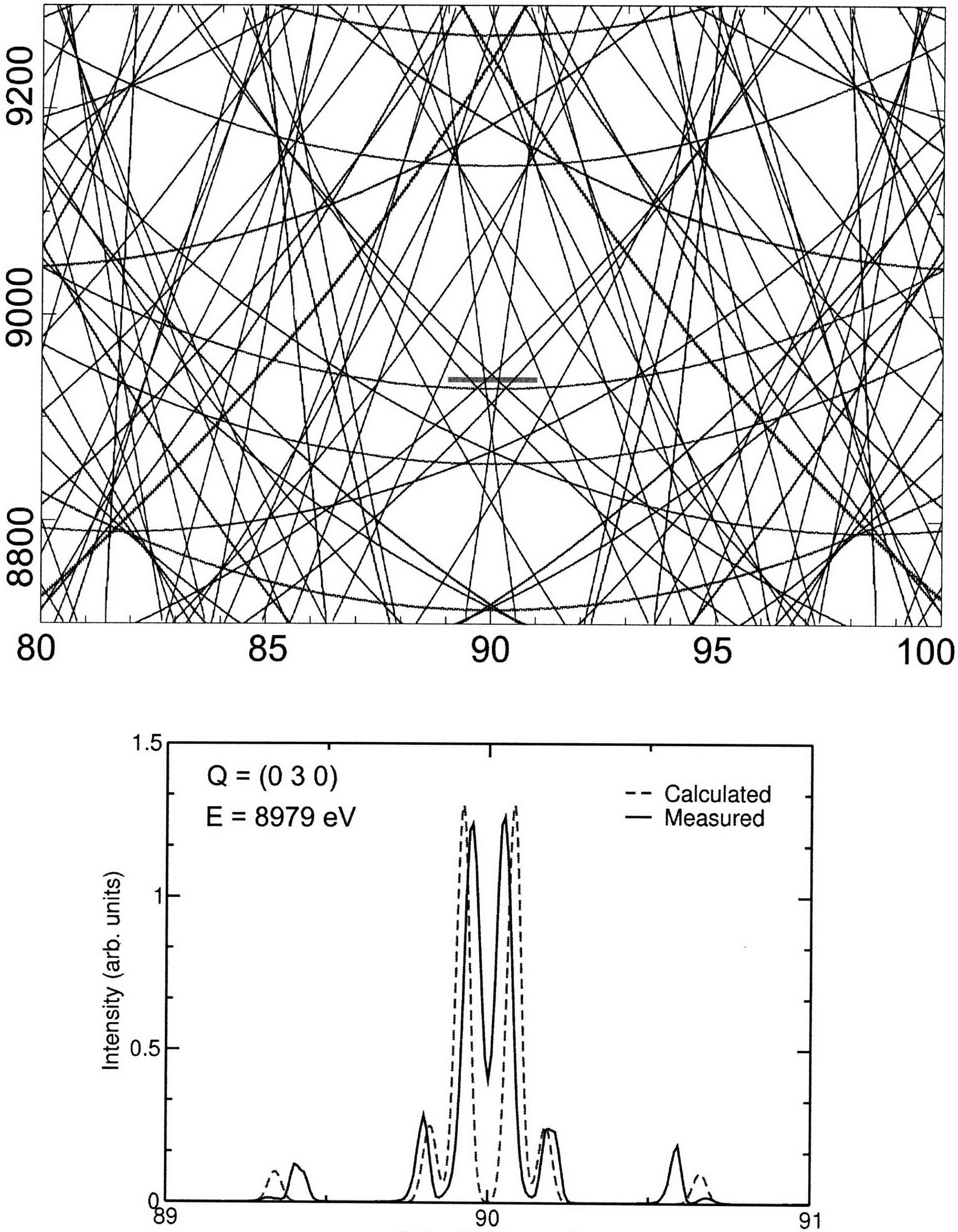

Figure 2-17: Renniger plot in a small range of Energy and Azimuth for LSCO at the forbidden (0 3 0) reflection. The plot in the lower panel corresponds to a measurement of the scattering intensity along the red line drawn on the Renniger plot. The small energy difference is due to slightly different lattice parameters used in the calculation and experiment.

which is equivalent to scanning the radius of the Ewald sphere, or one can rotate the sample about the Q-vector, which is equivalent to rotating the Ewald sphere about Q. From figure 2-16b it should be clear that either scan passes different reciprocal lattice points through the surface of the Ewald sphere. Since for different energies (i.e. sphere radii), a given reciprocal lattice point will intersect the sphere at a different azimuthal angle, it is possible to calculate the trajectory in energy-azimuth space of each allowed reciprocal lattice point. Such plots, known as Renniger plots, can be calculated and used to know where multiple scattering can be expected.

For an illustration of the usefulness of Renniger plots, I will use show where this was used to understand some of our measurements. The objective was to measure a weak modulation in $\mathrm{LaCuSr}_x\mathrm{O}_{2-x}$, which was predicted to give a small peak at the otherwise forbidden (0,3,0) position in reciprocal space. We were surprised to find rather intense peaks for certain incident energies. To understand this, a Renniger plot was calculated to ascertain whether or not these were multiple scattering peaks. Figure 2-17 shows the calculated Renniger plot for relevant region in energy and azimuth space for $Q = (0, 3, 0)$ $\mathrm{LaCuSr}_x\mathrm{O}_{2-x}$. In general if multiple scattering is a concern, then a Renniger plot can be used to find energy (E), and azimuth (A) values which have no nearby multiple scattering trajectories. In figure 2-17, the region around $E = 8800\ eV$ and $A = 91.5$ is a such a location.

2.4.7 Summary

This section provided a brief overview of the various non-structure related factors contributing to the x-ray intensity. Some of them can be well accounted for mathematically, therefore providing a good comparison between calculated and experimental scattering intensities. To summarize we can write down an expression for the total scattered intensity, taking into account the various corrections. For scattering out of the polarization plane with a polarized source from a *single crystal*

$$I(\vec{Q}) = \overset{\textbf{Lorentz-Polarization Factor}}{\frac{1}{\sin 2\theta}} \quad \overset{\textbf{Bragg Condition}}{|\sum e^{i\vec{Q}\cdot\vec{R}}|^2} \quad \overset{\textbf{Structure Factor}}{|S(\vec{Q})|^2} \quad \overset{\textbf{Debye-Waller}}{e^{-2W}}, \tag{2.46}$$

where 2θ is the scattering angle, from which Q can be calculated using an alternative form of the Bragg equation $Q = 2k\sin\theta$. Equation 2.46 contains all of the important fundamental corrections considered for the scattered x-ray intensity analysis in this work.

2.5 X-ray Powder Diffraction

There are many cases in the study of solid state materials where scattering from a single crystal is not practical. Characterizing a new material about which little is known is a non-trivial task with single crystals. An alternative, widespread technique is powder diffraction, which is the diffraction from a collection of thousands of tiny single crystals having random orientations. If an x-ray beam illuminates N single crystallites, and the scattering angle corresponds to that of a primary reflection, then a small fraction dN of the total crystal mass will be aligned within the resolution d2θ

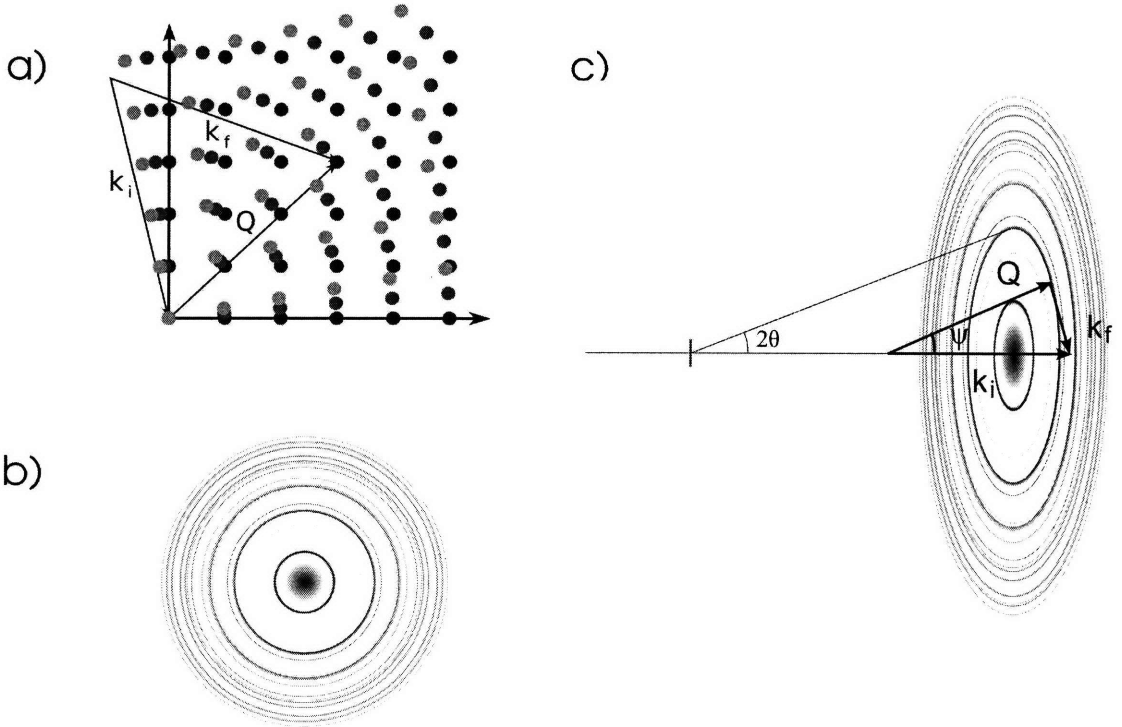

Figure 2-18: a) Reciprocal space map of scattering due to 3 misaligned single crystals. b) Simulated Debye-Scherrer rings for TiOCl. c) Scattering geometry schematic showing the fraction of crystals aligned within a range $d2\theta$ of the scattering angle.

of the Bragg condition. The total integrated intensity can therefore be estimated by calculating the total fraction of illuminated crystals which will diffract.

The scattering condition for an array of crystals is best visualized in the Ewald picture from section 2.4.2. Figure 2-18a shows the reciprocal space map of the scattering from three crystals which are slightly misaligned. By changing the direction of Q, the reflections from the crystal twins can be brought into the scattering condition. Here the scattering from only 3 crystals is illustrated. Generalizing this to 1000's of randomly oriented crystals one can imagine that the Bragg spots from each single crystal will fill in the entire 2π angle forming a ring of scattering. This is only two dimensions. To get the third, we then have to rotate this circle out of the plane to form a full 4π shell of scattering angles which satisfy the Bragg condition.

Placing a 2D position sensitive detector (image plate) behind the sample will result in a series of concentric rings centered on the incident beam direction, known as Debye-Scherrer rings (figure 2-18b). The radius of each Debye-Scherrer ring provides the scattering angle 2θ. The fraction of crystals which satisfy the scattering condition is given by the number of crystals whose Bragg planes are within $d\psi$ of θ. In reciprocal space, this condition carves out a shell of width $d\xi$ from the 4π angles of possible Q directions (figure 2-18c). If the angle between Q and k_i is ψ, then the solid angle, $\mathrm{d}\Omega$ will be $2\pi \mathrm{d}\psi \sin\psi$. The angle ψ is nothing more than one of the base angle of the isosceles triangle formed by $\vec{k_i}$, $\vec{k_f}$, and $\vec{Q}$. Since the apex angle is 2θ, we instantly arrive at the result $2\psi = \pi - 2\theta$, or $\psi = \pi/2 - \theta$. Therefore $\mathrm{d}\Omega$ is given by

$$d\Omega = 2\pi d2\theta \sin(\pi/2 - \theta) = 2\pi d2\theta cos(\theta).$$

If the intensity scattered from a single crystal is I, then the total intensity scattering from N crystals is NI. However, one needs to take into account that there may be multiple reflections having the same Q value. For example in a cubic system with lattice parameter a, all permutations of the reflections $(\pm1, \pm1, \pm1)$ have a Q of $\frac{2\pi}{a}\sqrt{3}$. The reflection $(\pm1, \pm1, 0)$ has 12 different permutations, therefore making it 1.5 times more likely to align with the Bragg angle than the (1,1,1) peaks. This multiplicity, m_{hkl}, must also be accounted for. With these considerations, the total number of crystals having Q vectors which will fall within an angle $\psi + d\psi$ is $m_{hkl}\mathrm{d}2\theta\pi\cos\theta NI/4\pi$. After the sample the x-rays will be scattered into the solid angle $\mathrm{d}2\theta\sin 2\theta$. For a detector with angular resolution $d\xi^4$, the fraction of the x-rays scattered into the detector will be

$$\frac{d\xi d2\theta\cos\theta m_{hkl}NI}{2\sin 2\theta} = \frac{d\xi m_{hkl}NIcos\theta}{2\cos\theta\sin\theta} = \frac{m_{hkl}d\xi d2\theta NI}{2}\frac{1}{2\sin\theta}. \tag{2.47}$$

Powder diffraction requires the consideration of an additional scattering angle dependent term in the intensity. Dropping the angle independent prefactors and combining this with the correction terms from equation 2.46 the total integrated intensity is,

$$I = |S(\vec{Q})|^2 \cdot e^{-2W} \cdot \frac{1}{\sin\theta\sin 2\theta}. \tag{2.48}$$

The last term in equation 2.48 is the Lorentz polarization factor for scattering out of the polarization plane of the beam (see section 2.4.1). Equation 2.48 assumes an isotropic distribution of sample orientations, but often times, the crystallites have a preferred orientation. This complicates the task of interpreting powder patterns immensely. Corrections are possible, but involved. This effect can be reduced by integrating over the entire Debye-Scherrer ring.

Powder diffraction is a very widespread and useful technique. Generally powders are easier to grow in larger quantities, making them attractive from an experimental point of view. However, one purpose of including this section was to illustrate the limits of scattering from powder samples. The obvious drawback is that all directional information in reciprocal space is lost to the integration over all angles. Secondly, from equation 2.48 powder scattering introduces an additional attenuation factor for scattering from large Q (high 2θ) reflections. Even this isn't so bad if scattering from small angles. The real drawback to powder diffraction comes from the small fraction of crystals that satisfy the Bragg condition. This can be shown by considering the factor NI from equation 2.47, which is the factor that counts the number of properly

---

[4] $\mathrm{d}\xi$ for an image plate is 2π

aligned Bragg planes. For a properly aligned single crystal all N of the planes will scatter into a detector having resolution d$\xi\times$d2θ. By comparison a powder of the same mass scattering into the same detector will have a fraction d$\xi d2\theta$ of the NI intensity. In section 2.1.2 we saw for a synchrotron the beam divergence is typically $\sim 1\times10^{-3}$ degrees. The magnitude of ξ is determined by the detector slits. For a very coarse resolution of 0.1 - 1^o, the fractional intensity is $10^{-4}-10^{-3}$. If a small structural change causes an observed peak with $\sim 1000 cts/sec$, 2θ at small scattering angle, then it may be detectable in a powder experiment through increased counting time. In general, however, resolving small structural changes with powder scattering is impractical, making single crystal samples a necessity.

2.6 Inelastic X-ray Scattering

In recent decades, with the improvement of synchrotron sources, the technique of *inelastic* x-ray scattering has been developed. In an inelastic experiment, the incident and final scattering energies are different. By keeping one of the energies fixed and scanning the other, the energy transfer spectrum can be measured. Such information is valuable for probing microscopic interactions through the vibrational spectrum of

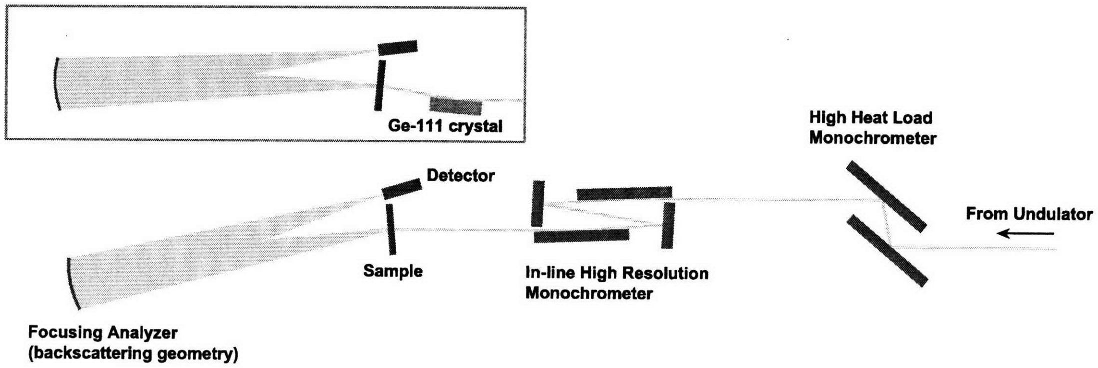

Figure 2-19: Inelastic x-ray scattering diffractometer at sector 3 of the Advanced Light Source at Argonne National Laboratory. The angles and distances are not to scale. Unique features of this instrument are the in-line monochromator and focusing analyzer. The inset shows a Ge-111 crystal deflecting the beam to lower 2θ angles allowing access to higher Bragg angles. Without the crystal the maximum 2θ is $\sim 18^o$. The crystal allows a maximum of $\sim 30^o$.

a unit cell, discussed in section 3.4.1.

The vibrational modes have typical energies on the scale of meV, requiring meV resolution from a $\sim 10\ keV$ x-ray beam. From equation 2.21, this requires a $\frac{\delta E}{E} \sim 10^{-7}$. Still the $\frac{\delta d}{d}$ term is negligible, since it is possible to manufacture sufficiently perfect monochromator crystals, so the issue still lies in the $\delta\theta \cot\theta$ term. An undulator beam with divergence of $\sim 1\mu$rad, requires a scattering angle $\geq 84^o$ to reach meV resolution, which is in the near backscattering limit.

Inelastic beamline design has a multitude of challenges. The first is simply because near backscattering geometry requires beam tubes to be sufficiently long to provide room for the experimental setup, which must be placed nearly at the beam source. The earliest inelastic x-ray scattering beamlines are designed in this manner. The second is having the ability to change the energy with meV precision. In a backscattering geometry, scanning the monochromator angle isn't very feasible, since this would require precision movement of the entire spectrometer. Instead, the fine energy control is obtained through changing the monochromator temperature, and letting thermal expansion change the energy by altering the Bragg plane spacing. Such a beamline are in operation at the European Synchrotron Radiation Facility (ESRF) in Grenoble, France. This spectrometer achieves an energy resolution of $\sim 3meV$ [44].

A more recent development in inelastic x-ray spectrometer design has been implemented sector 3 of the Advanced Light Source (APS) at Argonne National Laboratory (ANL). A schematic of the beamline is shown in figure 2-19. The remarkable breakthrough is the in-line monochromator, which not only can be easily integrated into normal beamlines, but it also has been optimized for maximal intensity and energy resolution [45]. At 21.5 keV, this monochromator has an energy width of 1.3 meV [44], which is nearly 3 times better than the backscattering monochromator at the ESRF. The monochromator, described in detail in reference [45], consists of two nested channel cut monochromators, the angle of which is precisely controlled to μrad precision. The temperature of the monochromator is maintained by cryo-cooling with liquid nitrogen for maximal stability.

After the high resolution monochromized beam the sample is mounted on a triple axis spectrometer, similar that illustrated in section 2.2.3. However, care must be taken in designing the two-theta arm with a meV resolution analyzer, due to the backscattering geometry. For example, sector 3 uses the silicon (18 6 0) reflection, with a Bragg angle of 89.98^o. Such a small angle between the beam incident on and scattered from the analyzer required its placement 6 m from the spectrometer center of rotation, with the detector near the sample (see figure 2-19). This results in a $\sim 2\ mm$ separation between incident and scattered beams, allowing sufficient room for the detector.

Having the analyzer at such a distance from the center of rotation presents additional design challenges. First of all, the angular divergence of the beam scattered from imperfect crystals is far greater than that of the monochromized beam. In order to increase the solid scattering angle, a focusing analyzer with a diameter of 100 mm was used. Of course this coarsens the Q-resolution of the spectrometer, so masks with various hole sizes were available for placement over the face of the analyzer.

The combination of having a heavy analyzer assembly on a 6 m long two theta arm required scattering in the horizontal plane for precise stable control of the scattering angle. Unfortunately this is also in the polarization plane of the undulator beam, therefore, the Q-dependent Polarization factor must be taken into account (see section 2.4.2). This also had the disadvantage that the x-ray hutch size limited the maximum scattering angle to $\sim 18^o$. For a time at sector 3, this limitation was overcome by placing a Ge-111 single crystal just before the sample to deflect the beam in the negative θ direction, then the spectrometer was translated to bring the beam back through the center of rotation (see inset in figure 2-19). Doing this changed the effective θ_0, allowing angles up to $\sim 30^o$. Recently this capability has been removed, however.

The overall spectrometer resolution is 2.2 meV as determined by placing Plexiglas^{TM} at the sample position, then scanning the monochromator. For practical purposes, the Plexiglas^{TM} scatters elastic x-rays into the full 4π solid angle, with an energy width much smaller than the spectrometer resolution (i.e. negligible convolution effects)[44].

In the beginning of this section it was stated that inelastic x-ray scattering with meV resolution has only matured in recent decades. While in principle the technology existed to build these beamlines has been in existence for quite some time, the main issue is one of intensity. First of all, taking a meV bandwidth requires eliminating $\sim 10^6$ photons from the keV white beam. Recall as well that in order to achieve such high resolution requires near backscattering Bragg angles, which according to section 2.3.2 has a very small atomic form factor, and is therefore a very inefficient scatterer. Not only are the photons backscattered once, at the monochromator, but again at the analyzer, resulting in an additional intensity loss. These factors are fundamental, meaning they are not due to lack of technology, or poor design, but are a result of the laws of physics. The only optimization possible is to choose materials for the monochromator and analyzer which have a larger atomic form factor at high angles. Otherwise, this is a limit defined by the laws of physics. For an idea how significant these factors are, at sector 3, the flux before and after the monochromator are $\sim 10^{14}$, and $\sim 10^8$ photons/sec. respectively. For comparison, the flux at the sample position of bending magnet beamline X22C at the NSLS (second generation light source) is $\sim 10^9$ photons/sec. Typical phonon peak intensities measured at sector 3 are tens of counts per minute, therefore a second generation light source simply cannot provide the photon flux necessary to detect phonon scattering. In this work data measured on the sector 3 beamline therefore represent a state of the art measurement which 30 years ago was simply not feasible.

2.7 SQUID Magnetometer

In the study of magnetic materials, it is essential to have the capability to characterize the bulk magnetism. While this can be done through various means, by far the most sensitive technique is Superconducting QUantum Interference Device (SQUID). SQUID theory is quite involved requiring extensive background in superconductivity. The scope of this work is to provide the essential concepts behind SQUID functionality. A nice overview of SQUID physics, practical design concepts, and a comprehensive list of references, the reader is directed to reference [46].

The essential component of a SQUID is the Josephson junction, which is a pair of superconductors separated by an insulator. In a superconductor, the charge carrier is a coupled pair of electrons. These so-called *Cooper Pairs* have total spin $S = 0$, and therefore obey Bose statistics. The Cooper pairs form a sort of Bose-Einstein condensate, and the cooper-pair wavefunctions become phase coherent. Therefore in the superconducting state, the electrons can be characterized by a single macroscopic wavefunction, $\psi = \psi_0 e^{i\phi}$. In the Josephson junction the wavefunction tunnels through the insulator from one superconductor to the other with some interesting effects.

If there is a phase difference between $\delta = \phi_1 - \phi_2$ between the wavefunctions on either side of the junction (see figure 2-20a), then a current, $I(\delta)$ will flow even in the absence of an applied voltage. If a DC voltage is applied to the junction, then the current will oscillate with a frequency $\omega = 2eV/\hbar$. These effects are summarized by the following fundamental Josephson junction equations

$$I = I_0 \sin\delta \qquad \text{Zero Applied Voltage} \tag{2.49}$$

$$, I = I_0 \sin\left[\delta(0) - \frac{2eVt}{\hbar}\right] \qquad \text{Applied DC Voltage} \tag{2.50}$$

where I_0 is the critical current of the junction, and e is the electron charge. The heart of a SQUID magnetometer is a superconducting ring, with two Josephson junctions encircling a magnetic flux Φ (see figure 2-20b). The fundamental property of the super-current in the ring critical to the sensitivity of a squid, is that the superconducting current will adjust itself to maintain an integer multiple of the flux quantum $h/2e$ passing through the ring. If a constant current is applied across the ring, then current will split and flow into junctions A and B, each with its own phase. For $\Phi = 0$, the phases will be equal, and the voltage V will be zero. When Φ is turned on, the superconducting current will fluctuate to maintain the integer multiple of $h/2e$ in the ring, causing the phases at A and B to be different. This will cause V to oscillate between values V_{min} and V_{max} with a period $T = \Phi_0 = hc/e$. This summarizes the essential physics behind a SQUID. The remaining considerations have to do with con-

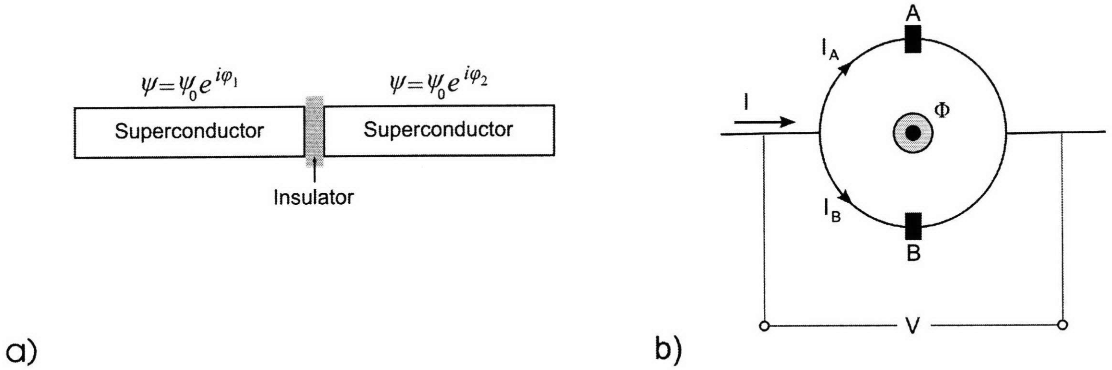

Figure 2-20: a)Schematic of a Josephson junction. The macroscopic wavefunction tunnels from one superconductor to the other through the insulator with a phase shift, $\delta = \phi_2 - \phi_1$. b) A Meissner loop with two Josephson junctions with a flux Φ passing through the middle. A constant bias current I is applied through each junction. If $\Phi = 0$, then the phases through each branch of the loop are equal and $V = 0$. As Φ is increased, the voltage at V will oscillate as a a function of applied flux with a period $\Phi_0 = hc/e$.

verting the oscillatory voltage response to a linear output proportional to the applied field. It turns out that a sinusoidal modulation of the applied field with frequency ω will cause V to oscillate at ω or 2ω depending on whether V is at or midway between extrema on the $V - \Phi$ curve. By feeding the oscillatory response of V into a lock-in

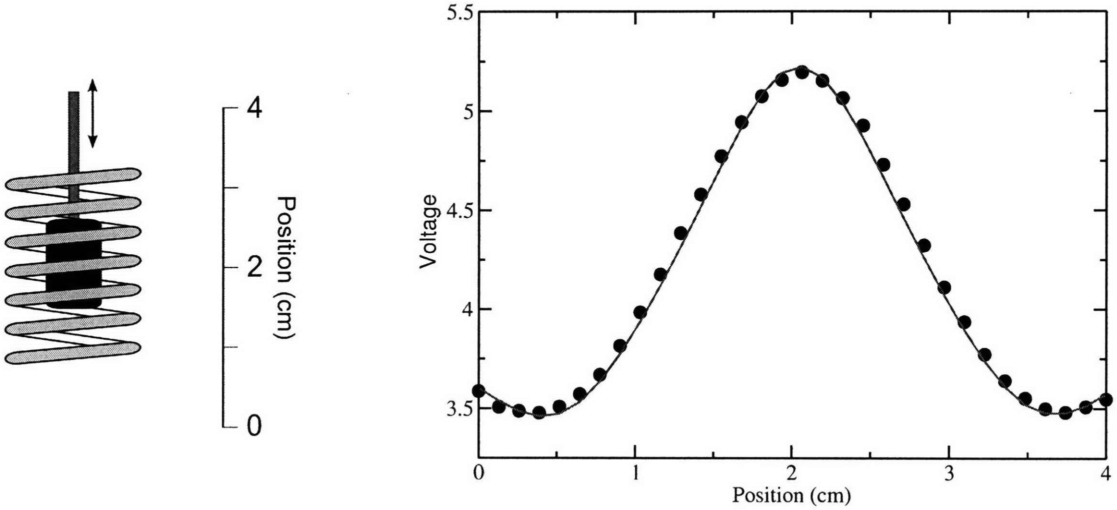

Figure 2-21: Quantum Design MPMS magnetic moment measurement. Sample is translated through the solenoid pickup coil which is connected to the SQUID circuit. Plotted is a measured response to the translation (filled circles) with its theoretical fit (line).

amplifier reference to a fixed oscillation, it is possible to bias the flux Φ to maintain the voltage V at an extremum. The output of the lock-in amplifier is then sent to an integrator, which tallies the number and direction of the flux correction resulting in a total response which is linearly proportional to the applied DC flux.

All of the magnetic susceptibility data in this work were measured on a Quantum Design Magnetic Properties Measurement System, which uses SQUID technology to measure magnetic moments. The sample is mounted on the end of a long thin rod, which is placed in the middle of a coil which is inductively coupled to the squid coil. To measure the magnetic moment of a sample the MPMS translates the sample out of the coil, then point-wise translates the sample through the coil, measuring the SQUID response as a function of translation. The software then fits this response to an appropriate theoretical model (predetermined by Quantum Design), and extracts the total magnetic moment.

2.8 Heat Capacity

A useful quantity to supplement the magnetic susceptibility is the specific heat. From thermodynamics, the specific heat is defined as the amount of heat required to change

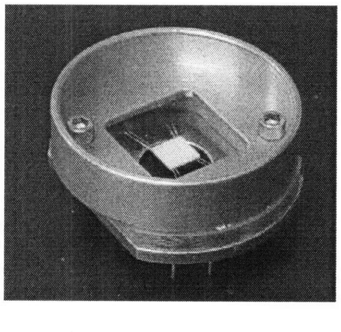

Figure 2-22: Quantum Design heat capacity puck. The sample is attached to the white platform using a thermally conducting grease. Under the platform are the heater and thermometer for the calorimeter. The puck is then inserted into a socket of the PPMS which connects it to the system circuitry and temperature control.

the temperature of a system by an amount dT,

$$c_p = \left.\frac{dQ}{dT}\right|_p, \quad c_v = \left.\frac{dQ}{dT}\right|_v, \tag{2.51}$$

where the subscripts v, p indicate constant volume and pressure respectively. Typically the experimentally measured quantity is c_p. Conceptually measuring c_p is relatively straight forward. By quantifying the amount of heat applied to a system while monitoring the systems temperature, it is possible to extract dQ/dT. In practice making detailed measurements of c_p with fine temperature resolution is a technical challenge. In this work specific heat data are presented which were measured using the specific heat option of a Quantum Design Physical Properties Measurement System (PPMS). Using a thermally conducting grease, the sample is mounted to a heat capacity "puck", which contains all of the elements of the calorimeter (figure 2-22. The PPMS uses a heating coil to heat the sample, therefore the sample heating is simply proportional to the coil current. The current is pulsed, and the thermal response of the system is monitored.

The heat capacity of the heating platform and grease are accounted for by first making a calibration or "addendum" measurement, which is simply a measurement over the desired temperature and/or magnetic field range with everything but the sample. This is then compared to the response with the sample to extract the sample specific heat using the differential equation

$$C_{total} = -K_w(T - T_b) + P(t), \tag{2.52}$$

where C_{total} is the combined specific heat of the sample and platform, K_w is the thermal conductance of the wires supporting the platform, $P(t)$ is the power applied by the heater, T is the platform temperature, and T_b is the temperature of the puck[47]. The solution is an exponential function with decay constant C_{total}/K. This is in the limit of "good" thermal coupling, which is determined "on the fly" by the instrument. If the thermal coupling is determined to be less than a given threshold, then a different "two-tau^{TM}"[5] model is implemented. The effectiveness of this model isn't readily clear, and since the data in this work were taken in the "good" thermal conductivity limit, we will limit the discussion to equation 2.52.

A primary reason for measuring the specific heat is to extract the entropy, S, which is related to the specific heat by the relation

$$c_p = T \left. \frac{dS}{dT} \right|_p . \tag{2.53}$$

The entropy is a useful quantity for characterizing phase transitions, which we will see in section 3.2.

---

[5] The two tau model is a Quantum Design trademark

3 Spin-Peierls in TiOCl

3.1 Sample Growth and Characterization

The first reported growth of TiOCl was by Schäfer et. al. in 1958 [48]. The article discusses various chemical reactions which lead to the formation of TiOCl. For our purposes, the most convenient reaction was

$$2\mathrm{TiCl_3} + \mathrm{TiO_2} \rightarrow 2\mathrm{TiOCl} + \mathrm{TiCl_4} \tag{3.1}$$

At room temperature $TiCl_3$ and TiO_2 are powders. The basic procedure is to seal a stoichiometric mixture of the two reactants, then vaporizing them at about 650°C, which upon cooling form either a fine powder or single crystals of TiOCl. This section is dedicated to describing the procedure used to implement this procedure as well as the various techniques used to optimize the growth.

3.1.1 Powder Samples

Both $TiCl_3$ and TiO_2 are hydroscopic, so care had to be taken when handling them. When not in use, the powders were stored in an argon environment. To mix the powders the molar fraction had to be converted to mass. The mass ratio of $TiCl_3$:TiO_2 in the above reaction is 3.86:1 . Through multiple trials, however, we determined that a mass ratio of 6:1 resulted in a more complete reaction. The powders were weighed, mixed and packed into a cleaned iron high pressure bomb. The chamber was then sealed in the glovebox, then transfered to the furnace for sintering. The furnace was then ramped to 600 ^oC at a rate of 1^oC per minute. After 12 hours at 600 ^oC the furnace was then ramped back down to room temperature at the same rate (1^o per minute). The bomb was then open in air, at which point a yellow-green gas would emerge. We assume this to be the $TiCl_4$ reacting with water vapor in the air. The powder was then repeatedly washed with acetone then dried. The powders were stored in a dessicator to keep them dry. The structure and composition were verified using x-ray powder diffraction (see section ...). Figure 3-1 shows a powder diffraction pattern measured on one of our better powders on a rotating anode source, compared to the calculated diffraction pattern. All of the peaks in the calculated pattern have corresponding measured peaks, meaning the crystal symmetry and lattice parameters are correct. The relative intensities are also consistent, with only slight deviation. This indicates that the chemical composition is basically correct. To make stronger claims requires a measurement with better statistics out to higher two theta angles. Generally, detailed structural analysis is performed on powder diffraction patterns

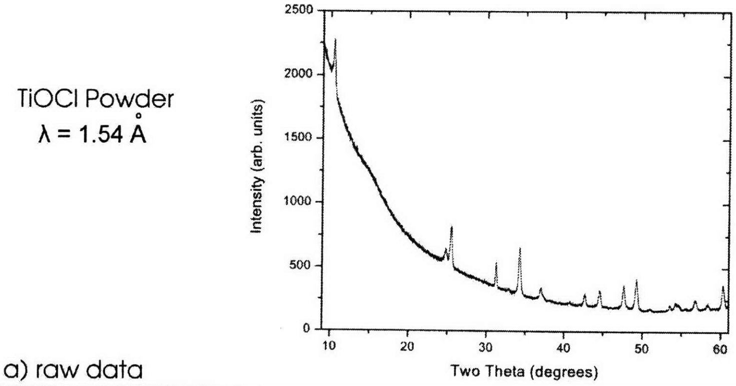

a) raw data

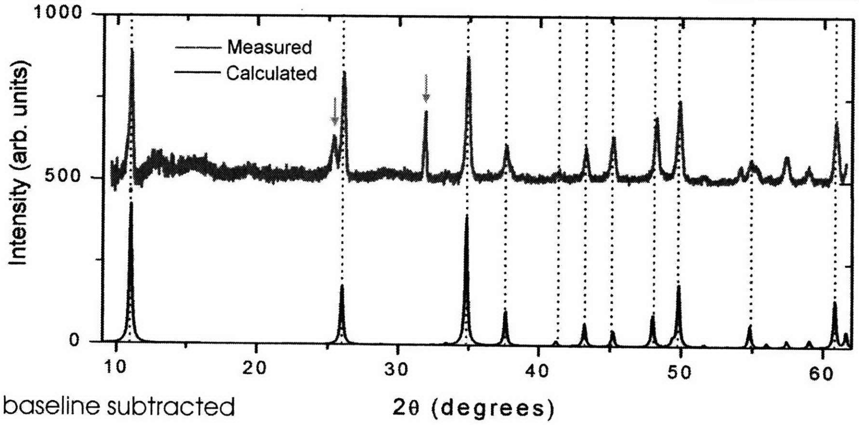

b) baseline subtracted

Figure 3-1: TiOCl powder diffraction pattern measured on a rotating anode diffractometer. The sloping background in a) is an experimental artifact, and has therefore been subtracted in b) for better comparison with the calculated diffraction. The arrows indicate measured peaks which do not occur in the calculated pattern.

measured either at a synchrotron or neutron source. Examples of each of these can be found in sections (...) and (...).

Even with the best powder diffraction data available, the detection of small impurity concentrations isn't feasible. It becomes necessary to rely on other experimental techniques, depending on what effect impurities will have on the material properties. In the case of TiOCl, the 1-D magnetic properties are of interest, therefore knowing the magnetic impurity content becomes important. Fortunately this is straightforward to characterize using a SQUID magnetometer (see section 2.7. The magnetic susceptibility was measured using a Quantum Design MPMS (see section 2.7). A typical curve for TiOCl is shown in figure 3-2. The various magnetic signatures highlighted by Seidel et. al. [4] are labelled. At this point, the region of interest is $T < 50K$, labelled "Curie tail". The "gap", T_{c_1}, T_{c_2} are all intrinsic signatures. The curie tail and the broad "bump" around 300 K are indicators of impurity content. The origin of the 300 K bump remains a bit of a mystery, but we're quite sure it's

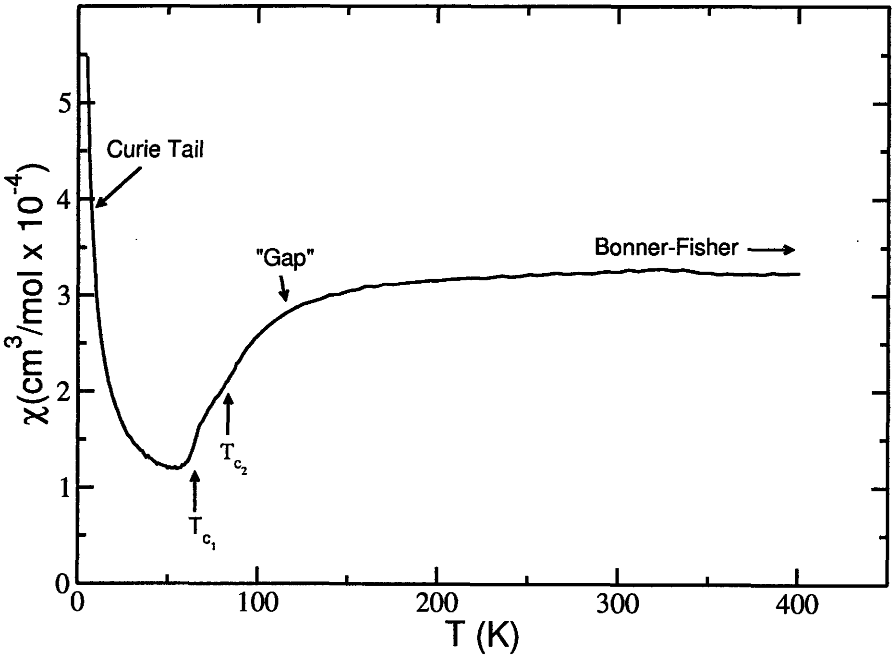

Figure 3-2: Plot of DC susceptibility measured on ~ 50mg of TiOCl powder with highlighted characteristic magnetic signatures (according to Seidel et. al. [4]). The applied field, H, and sample mass have been divided out to convert measured magnetic moment to magnetic susceptibility.

related to some impurity, since its magnitude fluctuated from batch to batch.

The Curie tail arises from a small concentration of paramagnetic impurities within the sample. As the label implies, a paramagnet follows Curie's law, namely

$$\chi(T) = \frac{c}{T - T_c} + \chi_0. \tag{3.2}$$

For our purposes, T_c is 0, and χ_0 is a temperature independent offset. It turns out that it is possible to quantitatively determine the impurity concentration from the magnitude of the Curie tail. The curie constant, c, can be extracted from a fit of the $T < 50K$ region to equation 3.2. The expression for c derived using a microcanonical ensemble of spins is

$$c = \frac{N_o \mu^2}{k_B}, \tag{3.3}$$

where N_o is the number of magnetic atoms per volume, μ is the magnetic moment which in our case is μ_B, the electron magnetic moment, and k_B is Boltzmann's constant.

The only challenge to extracting a meaningful number from the fit, is to express c in the proper units. The MPMS measures the total magnetic moment, μ, using the cgs unit EMU. To extract the susceptibility from μ requires the expression, $M = \chi H$, where $M = \mu/V$ is the magnetic moment per volume, and H is the applied field. In cgs, M and H have the same units, therefore χ is unitless. For example,

$$1\ emu/cm^3 = 1\ erg/gauss/cm^3 = 4\pi\ Oersted.$$

Therefore it is possible to change from μ in emu to a unitless χ by the following transformation:

$$\chi = \frac{M}{H} = \frac{\mu}{H_{oersted} \cdot V} = \frac{4\pi\mu \cdot d}{H_{emu/cm^3} \cdot m}, \tag{3.4}$$

where d and m are the density and mass of the sample respectively. To calculate the impurity concentration, equation 3.3 needs to solved for N_o,

$$N_o = \frac{c \cdot k_B}{\mu_B^2} \tag{3.5}$$

The final step is to substitute the fitted value for c into equation 3.5:

$$
\begin{aligned}
N_o &= \frac{\left(1.615\times10^{-3}\right)(.0862)}{(5.788\times10^{-6})(9.274\times10^{-21})} &&= 4.1\times10^{20}\,cm^{-3} = 2.064\times10^{-4}\text{Å}^{-3}\\
[N_o] &= \frac{[K][meV/K]}{[meV/Oersted][Oersted{\cdot}cm^3]} &&= [cm^{-3}].
\end{aligned}
$$

This corresponds to about .02 per unit cell, or 1 paramagnetic moment every 47 unit cells. Compared to the interaction of neighboring spins, any perturbation due to the paramagnetic impurities is likely too small to have an effect. In summary, we can safely proceed with confidence that we are measuring the intrinsic magnetic properties of TiOCl. This assumes, of course, that the powder is pure-phase TiOCl, which from the x-ray powder diffraction (fig. 3-1) there is clearly a small impurity phase concentration. The only way to determine the origin of the paramagnetic signal is to measure the susceptibility of a known phase pure sample. The batch on which tl

ol

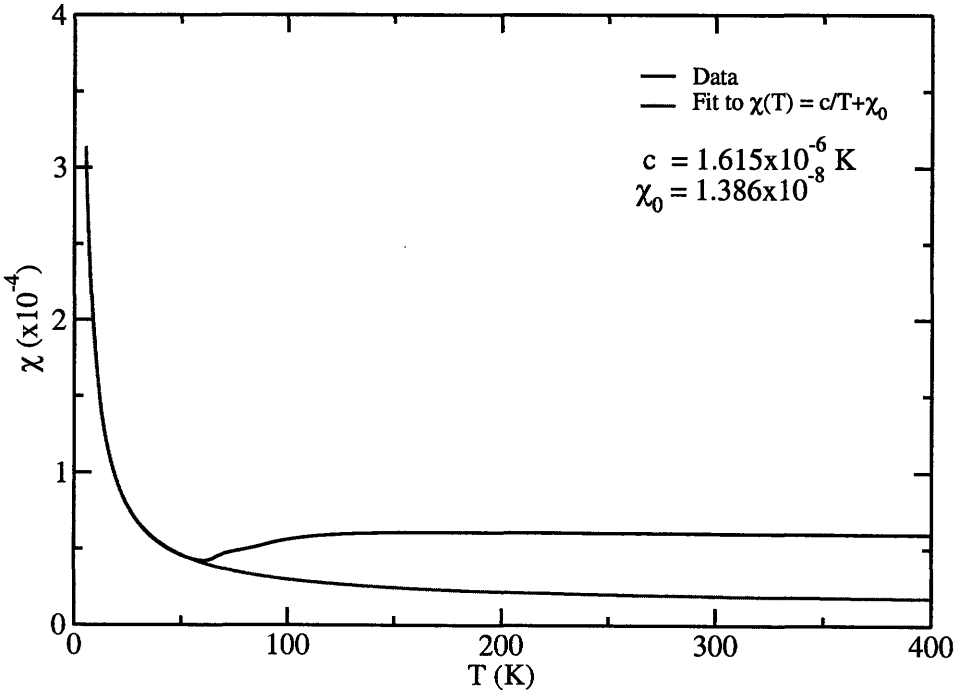

Figure 3-3: DC Susceptibility with low temperature (T < 50 K) region fitted to curie law, $\chi(T) = \frac{c}{T} + \chi_0$.

3.1.2 Single Crystal Samples

Powders are convenient, in that it is generally easy to grow large quantities in a short amount of time. For many bulk property measurements, but because a powder consists of a large number of randomly oriented single crystals, directional information is lost. For scattering measurements, this means integrating the Brillouin zone in all directions, losing much valuable information. Such information requires a single crystal sample.

The preparation of TiOCl single crystals is similar to the powder growth. The handling and stoichiometry of the reactant powders is identical. However, unlike the powder growth, single crystal growth works by vapor transport. In vapor transport, the growth chamber has a built-in temperature gradient, with the constituent powders on the hot side. The powders vaporize, and travel across the gradient condensing on the cool side of the chamber. To achieve the necessary temperature gradient, the prepared powders were loaded into long quartz tubes which were sealed by melting off the ends in a propane glass blowers torch. First one end would be sealed, the tube then transferred into the argon-glove-box for filling. Because it was not possible to heat the quartz tubes in the glove box, the end would be sealed by Parafilm^{TM} after the tube was loaded. The tube would then be quickly removed from the glove box, hooked up to a vacuum pump which evacuated the tube to $\sim 10^{-2}$ torr. The tube would then be sealed under vacuum and allowed to cool submersed in insulated packing material (to slow the cooling). The optimal growth tubes had a 2mm thickness, 2cm outer diameter, and were about 40 cm long. The tube was then placed in a two-

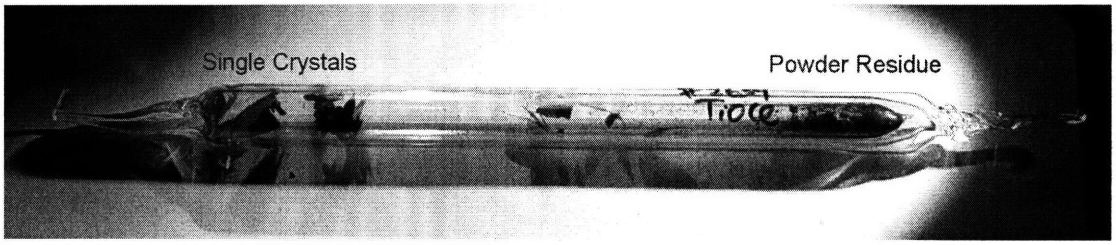

Figure 3-4: Sealed quartz tube with TiOCl single crystals on one side and powder residue on the other. This was one of the more successful growths in terms of crystal quality and size.

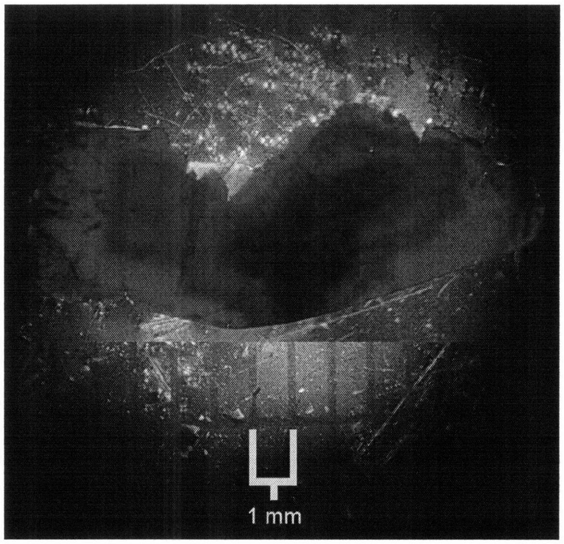

Figure 3-5: TiOCl single crystal viewed under an optical microscope with back-lighting. This was the biggest crystal from all of the growth attempts (extracted from the tube pictured in figure 3-4). It is $\sim 100 \times 50mm$ across, and $\sim 50\mu m$ thick. On average the crystals were rectangular having dimensions $\sim 30mm \times 40mm \times 40\mu m$ along a,b,c respectively.

zone tube furnace, and the whole tube was heated up uniformly to 650 ^oC, at a rate of 1 ^oC/minute. After several 12 hours at 660 ^oC the temperature on one side of the furnace was lowered to 550^oC. After about 12 hours under gradient, the tube would begin to form small seed crystals on the cool side. We would let these seed crystals grow for about 3-5 days...until the powder on the hot side was gone. When the growth was complete, the tubes would contain many thin single crystals stuck to the cool side of the tube, with only a small amount of powder residue remaining on the hot side. One of the more successful growth tubes in terms of crystal size and quality is shown in figure 3-4. The tubes were then cut open, and the crystals washed repeatedly in acetone. The resultant crystals are small brownish colored translucent rectangular flakes with average dimensions $\sim 30mm \times 40mm \times 40\mu m$ along a,b,c respectively. One of the larger crystals obtained is shown in figure 3-5. The crystals were very fragile and tended to self cleave along the c-direction. To check the single crystal structure and composition, x-ray powder diffraction was performed on a few pulverized crystals. Rotating anode results indicated very high purity, and as part of another experiment, we even measured the powder diffraction at the NSLS powder diffraction beamline, X7A. This beamline is a wiggler source which from section 2.1.4 we know to have a broad divergence in the oscillation plane. However, this was utilized to acquire more intensity by loading the powder into a tube having roughly the same dimensions as the beam. Since only 2θ matters, the large sample dimension parallel to the 2θ-axis doesn't affect the resolution. In addition a position sensitive detector was used to integrate over a larger range of 2θ, greatly reducing the counting time, and the sample was continuously rotated for better powder averaging. Figure 3-6 shows the powder diffraction pattern from the synchrotron. The measurement

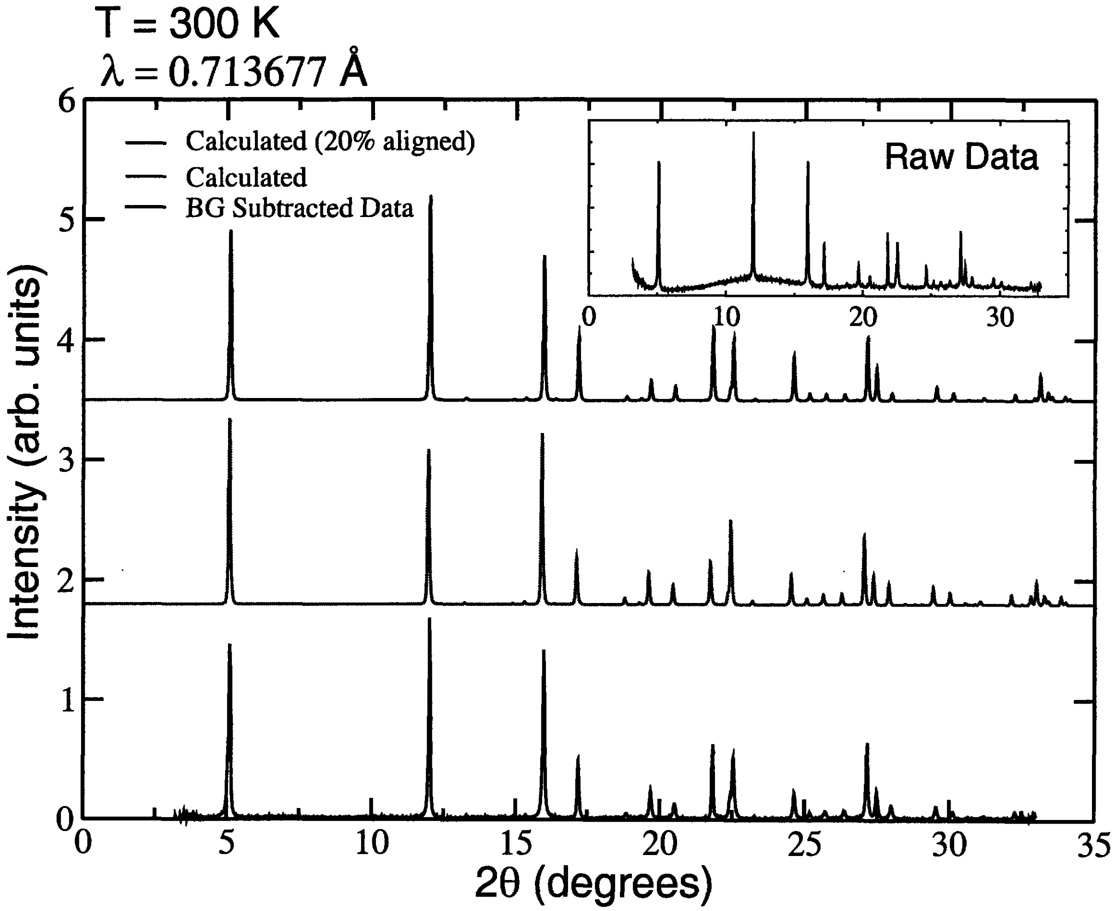

Figure 3-6: Powder diffraction measured at the NSLS beamline X7A. The inset shows the raw data which has a weakly 2θ dependent baseline which has been subtracted for better comparison with the calculated pattern. The arrow highlights a small impurity peak. Compared to the diffraction pattern in figure 3-1, this diffraction pattern has far better signal to background, and a larger range in Q. Taking these into consideration, one can concluded that the single crystal structure and stoichiometry are nearly ideal.

time is comparable to that of figure 3-1. The synchrotron data is better for structural refinement not only because the signal to background ratio is significantly better, but also because of the high energy used ($E \sim 17keV$) the number of accessible peaks is greater for better comparison with the theory. In principle this data was good enough for a full Rietveld refinement. This we did not do, however, rather we simply verified by inspection. The calculated and measured diffraction patterns agree perfectly with respect to peak positions, meaning the lattice parameters and unitcell symmetry are correct. The relative intensities vary, which could be due to the absence of a Debye-Waller correction in the calculation.

Again, to verify the magnetic properties of the crystal, we measured the susceptibility on a single crystal and compared it to the power susceptibility. All of the expected signatures indicated in figure 3-2 were present. There was a small curie tail which by following the same procedure as in section 3.1.1 was determined to be about 0.0033/unitcell or about 1 impurity every 300 unitcells. Because of the high single crystal purity, this helps to pin down the intrinsic paramagnetic impurity content. This also indicates that the powder is probably contaminated with a small concentration of another paramagnetic phase.

3.1.3 Optimization of Vapor Transport Growth

Glass Lathe

The previous section described in general the process by which we grew our TiOCl single crystals. The crystals grown by the method described were sufficient for most of our measurements. However, increasing interest in doing neutron scattering on single crystals, lead to a demand for larger crystals. From trial and error, we had determined that larger amounts of reactant powders resulted in larger crystals in general. The limiting factor to the amount of powder we could load into a quartz tube was the structural integrity of the tube itself. Because we were essentially vaporizing all of the powder, often times the resulting pressure would cause the tube to explode inside the furnace. The situation was worsened by the fact that sealing the tubes required melting and stretching the glass from the original diameter to zero, thus introducing strain, and lowering the pressure threshold. This is the reason for the small diameter, yet thick glass tubes. The only way to contain more powder was to make the tube longer, which also had it's limitations, since a good gradient could only be maintained over about 30-40cm. It was therefore of great interest to increase the diameter of the tube in order to achieve higher chamber volume. To do this, however, would require a very gradual decrease in diameter down to the point where it is sealed off. Doing this by hand was difficult enough with just a plain glass tube, let along when the tube was under vacuum. The problem was further complicated by the requirement to use quartz rather than Pyrex glass, because of the high baking temperature. To overcome these difficulties would require the tube to be constantly turned while being heated, then gradually drawn out while turning until it eventually separated. In the glass industry this is commonly facilitated through the used of a glass lathe. Glass

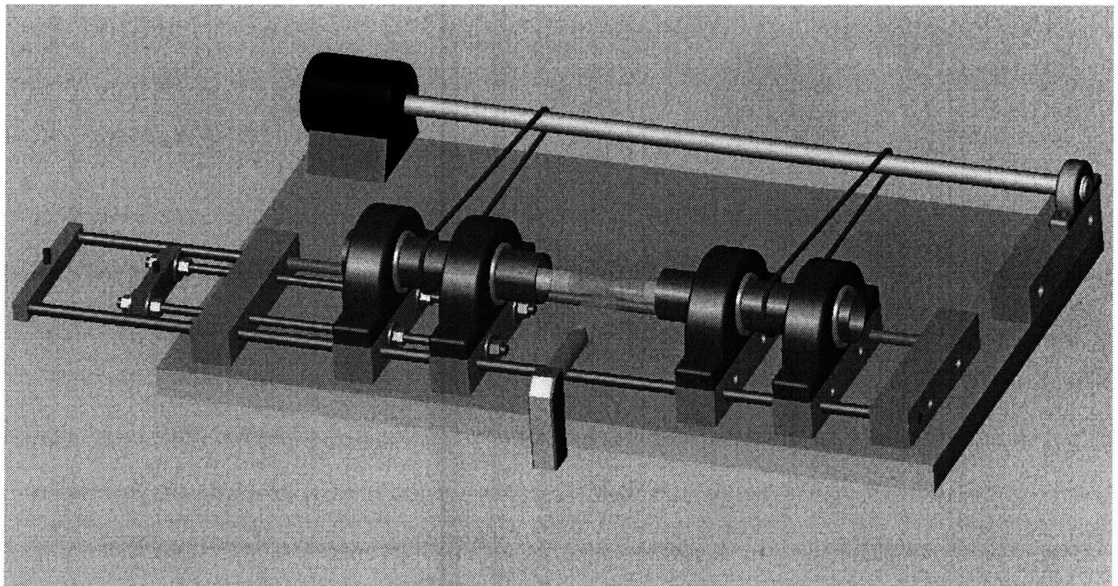

Figure 3-7: Glass lathe for making TiOCl single crystal growth chambers. The chucks of the lathe are hollow stainless steel tubes which also serve as the pulleys. Both chucks are coupled to the motor by bands which turn around a long rod. This design allows the translation of one of the chucks while keeping both turning at the same rate. The glass tube can be any arbitrary length and the hollow chuck design allows for a vacuum tube to be connected through a swivel joint to the end of the tube.

lathes are commercially available, but expensive, so we set out to build a low budget lathe optimized for the purpose of making TiOCl growth chambers.

To serve our purposes, the glass lathe had to consist of two chucks which would hold the glass in place, since when the glass melts it has no structural integrity. The chucks had to turn at the same speed or else the glass would break when it is still solid. In additional to these considerations one of the chucks needed to translate while turning, in order to draw the molten glass out. These considerations were all taken into account with the design in figure 3-7. The lathe chucks were two stainless steel tubes mounted in a set of pillow blocks which were mounted on freely moving aluminum blocks. One set of pillow blocks was anchored to the table while the other was left free to translate. the stainless steel chucks also had a belt around them and therefore served as pulleys which were coupled to a long rod connected to a motor. This kept the two chucks rotating at the same speed. The effectively wide pulley allowed for free movement of the free chuck while still being coupled to the motor.

While designs for mounting the torch and translating the chuck by some hydraulic device were in the design phase, this was never implemented. Rather the lathe required two operators, one to hold the torch and the other to translate the sample. The lathe was successfully used to manufacture a handful of growth chambers, but unfortunately, the resultant crystal size was about the same. Given more time, a methodical approach to sample chamber design would surely have lead to larger crystals. However, as is usually the case, there were time constraints, so other means to obtain larger crystals had to be explored.

3.1.4 Crystal Growth the "Hard Way"

While work was underway to optimize the crystal growth to obtain larger single crystals, it was obvious that ~gram sized crystal necessary for neutron scattering wouldn't be attainable for quite some time. Motivated by the work of work of He et. al [49], we therefore decided to make a co-aligned array of the ~mg sized crystals. The goal was to have 1g of single crystal co-aligned within 2^o. The average crystal mass at the time was nominally ~ 1 mg, requiring $\sim$ a 1000 crystal array.

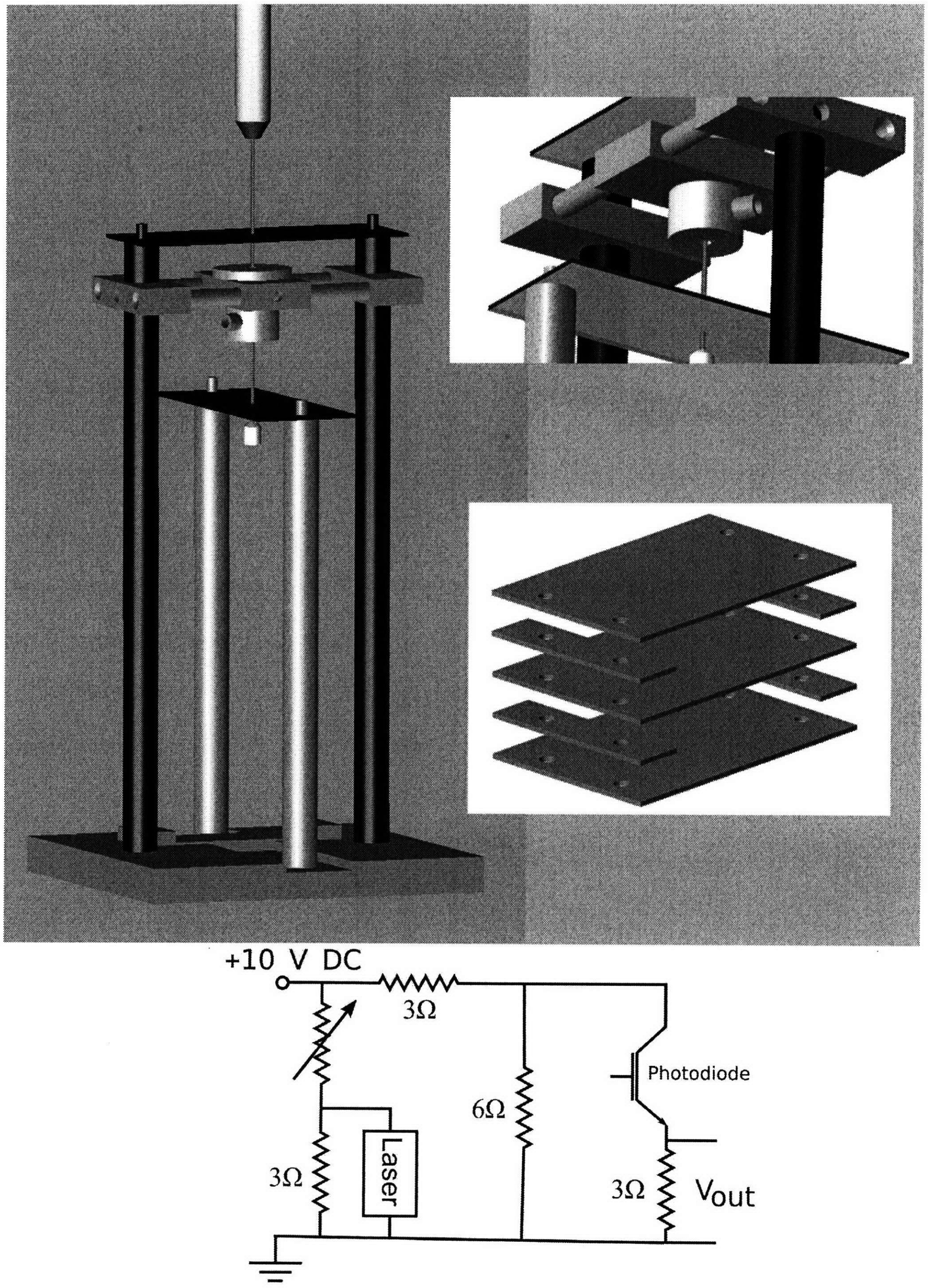

Figure 3-8: Apparatus to aid in assembling ∼1000 co-aligned single crystals for neutron scattering experiment. The alignment procedure is discussed in detail in the text. Below is a wiring diagram for the electronics. The sole purpose of the circuit is to provide the proper voltage to the source of the diode, and as well provide a variable voltage to the laser, which was a pen laser modified to be plugged into a DC power source.

The essential step to co-aligning single crystals is to first determine the crystal orientation. This is a straight-forward task using x-rays, but x-rays can be time consuming. Once the orientation is known, it must then be fixed to a well-defined reference direction. The 2^o mosaic spread requires that each crystal on average be within 1^o either direction of the reference, or within $\pm 0.2\%$. This proved to be the real challenge in the construction of the crystal array.

It turns out that TiOCl has a couple of properties which we were able to utilize in the co-alignment. First of all, the crystals grow in thin flakes with c perpendicular to the crystal face, reducing the problem to finding the orientation of the a-b plane. Secondly, TiOCl is an insulator, and therefore transmits light. Due to the orthorhombic crystal structure, the transmitted light is polarized. Finally, because the crystals are quite thin as grown, the transmitted intensity is significant. These properties enabled us to orient the a-b plane by detecting the transmitted intensity of polarized light through the crystal as a function of rotation about the c-axis. This still leaves the problem gluing the crystals within 1^o of a fixed reference. To facilitate the alignment in this procedure, I designed the apparatus in figure 3-8.

The sample was fixed to the underside of a rotating cylinder by suction through a small pinhole leading to a vacuum pump. The cylinder had a concentric hole which allowed light from a pen laser to pass through the sample and onto a photo diode. The pen laser proved an ideal light source as it provided a very intense, highly collimated, polarized beam, which was refined by aligning its polarization with that of a polarizing polymer. Upon rotation a minimum in the measured intensity occurred every 180^o. This would uniquely define the crystal orientation. The angular resolution was then improved by placing a second polarizer aligned perpendicular to the first one under the sample, therefore reducing the period between minima by a factor of 2, effectively doubling our angular resolution. Once the minimum was found orientation would be locked in using a set screw. The lower polarizer and detector would be removed, and the entire cylinder translated down to the sample plate where a small drop of GE^{TM} Varnish held the crystal in place. The pump was then turned off, and the cylinder raised. Since the crystals cleave easily along the c-direction, stacking the crystals was

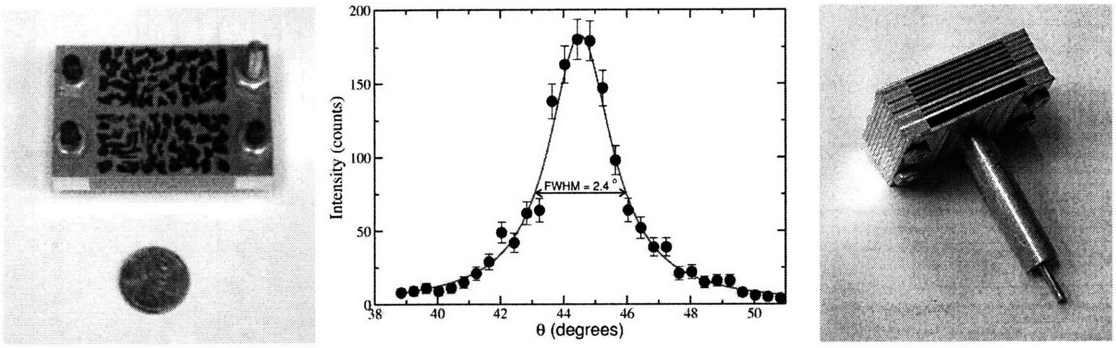

Figure 3-9: Assembled crystal mosaic along with a characteristic rocking curve measured on a triple axis neutron spectrometer showing an angular spread of 3^o, slightly larger than the 2^o desired.

not possible. Instead, the crystals were aligned side by side, filling up the face of 2cmx3cm aluminum plates which were then stacked as shown in figure 3-8.

This process greatly simplified the co-alignment, reducing the time for one single crystal to about 5 minutes. In total we co-aligned 1200 crystals for a mass totalling 813 mg. The assembled crystal along with a rocking curve from a triple axis neutron spectrometer are shown in figure 3-9. The FWHM of the rocking curve is a direct measure of the crystal mosaic spread, which we measured to be about 3^o, slightly larger than our goal.

This method of crystal growth can be quite advantageous, in that one has very good control over the crystal quality(as was the case in reference [49]), since the crystallites to be glued must be hand selected. Unlike natural crystal growth where unexpected delays are common, this technique has the additional advantage that the end result depends primarily on time invested: more time=larger crystal. The problem is the sample plates and glue introduce a significant background. Whether or not this is problematic depends on the experiment.

3.2 Thermodynamic Characterization

Once high quality single crystals were obtained, it was possible to explore the physics of TiOCl to determine whether or not it was a novel inorganic spin-Peierls system. The first challenge was to further characterize the "gap" as well as the magnetic transitions highlighted by Seidel et. al. [4] (see section 1 and figure 3-2). Throughout this work the variables T_{c_1}, T_{c2}, and T_{gap}, as defined in figure 3-2 will be referenced.

The first set of measurements was meant to supplement the susceptibility measurements already published. The idea was to characterize the so-called gap. If the gap is due to singlet pairing, as required for a spin-Peierls transition, then the spin in the gapped state is $S = 0$, and therefore there is no preferred orientation. In an ordered magnetic state, there will be some anisotropy in the magnetic response, so one simply needs to compare the susceptibility along all three crystallographic directions. In preparation for the susceptibility measurement, six crystals were co-aligned to increase the sample size, and thus improve the signal to background ratio. The crystal orientation was determined using a triple axis spectrometer on a rotating anode source. Once the orientation was known, the crystal was cut along the b-direction, to provide a straight reference line. The six crystals were then stacked and squeezed

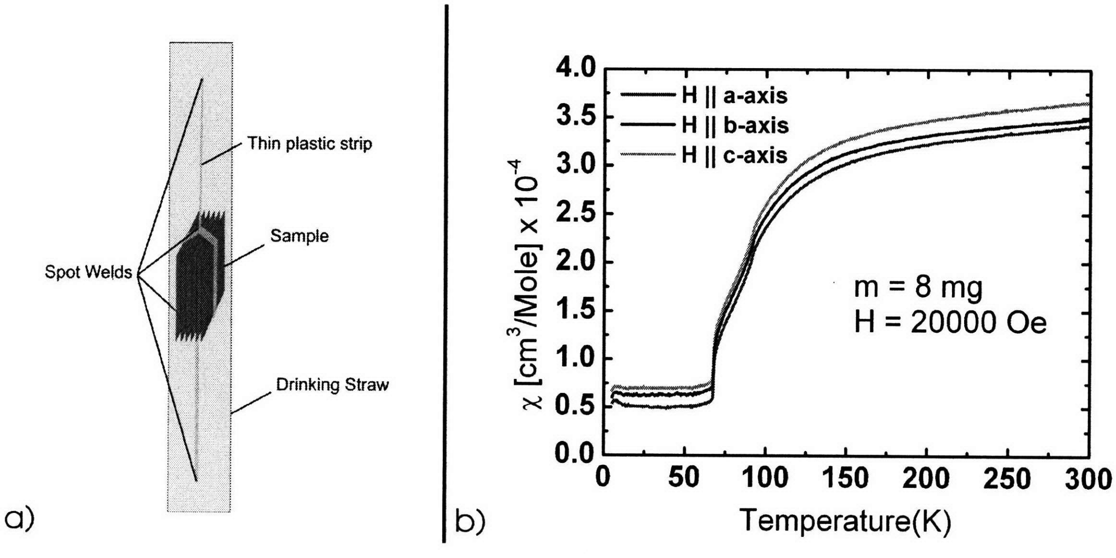

Figure 3-10: a) Sample mount configuration for anisotropy measurements. The stack of co-aligned samples is squeezed between two thin strips cut from a plastic drinking straw. The strips are then spot welded on either side of the crystal stack to hold them in place. The entire assembly is then spot-welded to the inside of a drinking straw. This allowed for a small-uniform background. b) The susceptibility measured along the a,b,c directions. The curie tail has been fitted and then the temperature dependent part subtracted out. Clearly, the data look practically identical, with only a small temperature independent offset, most likely due to crystal field anisotropy.

between two long-thin plastic strips cut from a plastic drinking straw. The two strips were then melted together on either side of the crystal stack to hold them in place (figure 3-10). This configuration provided a low, position independent(see section 2.7) background. While it was difficult to quantify, the co-alignment was estimated to be within at least 4 degrees.

The total assembled sample mass was 5.1 mg, which was measured under an applied field of $H = 20000Oe$. After each direction was measured, the sample was removed from the MPMS, realigned in a different orientation, then placed back into the instrument for measuring. The magnetic susceptibility was measured along all three crystallographic directions. After the subtraction of a small Curie tail, the curves are identical, except for a small temperature independent offset, most likely due to anisotropic crystal field contributions (figure 3-10b). This isotropic drop in susceptibility implies spin-singlet formation, as expected. In the process of measuring the isotropy, data was taken upon warming and cooling, and to our surprise, the susceptibility exhibited a thermal hysteresis at T_{c_1}, but not T_{c_2}(figure 3-11a. Hysteresis is typically associated with a first order phase transition, which is a surprising result, since spin-Peierls transitions observed in past materials have been second order[23][50]. This novel observation sparked a more detailed investigation as to the nature of the transitions at T_{c_1} and T_{c_2}.

An important tool to characterize phase transitions is the heat capacity measurement. If sensitive enough, the heat capacity measurement can quantify the latent heat required to facilitate the phase transition, and from this the total entropy can be estimated. Figure 3-11b,c compares the heat capacity, C_p with $d(\chi(T) \cdot T)/dT$, a quantity proportional to the magnetic specific heat [51]. Clear peaks in C_p at T_{c_1} and T_{c_2} correspond to peaks in $d(\chi(T) \cdot T)/dT$ leading to the conclusion that these anomalies have some magnetic contribution. A rough estimate of this contribution, can be obtained by integrating the specific heat in order to calculate the total change in entropy over the transition region. However, at these temperatures, the heat capacity is dominated by phonons, so before integrating, a background must be subtracted. Without knowing a priori what the intrinsic specific heat should be, we simply fit the

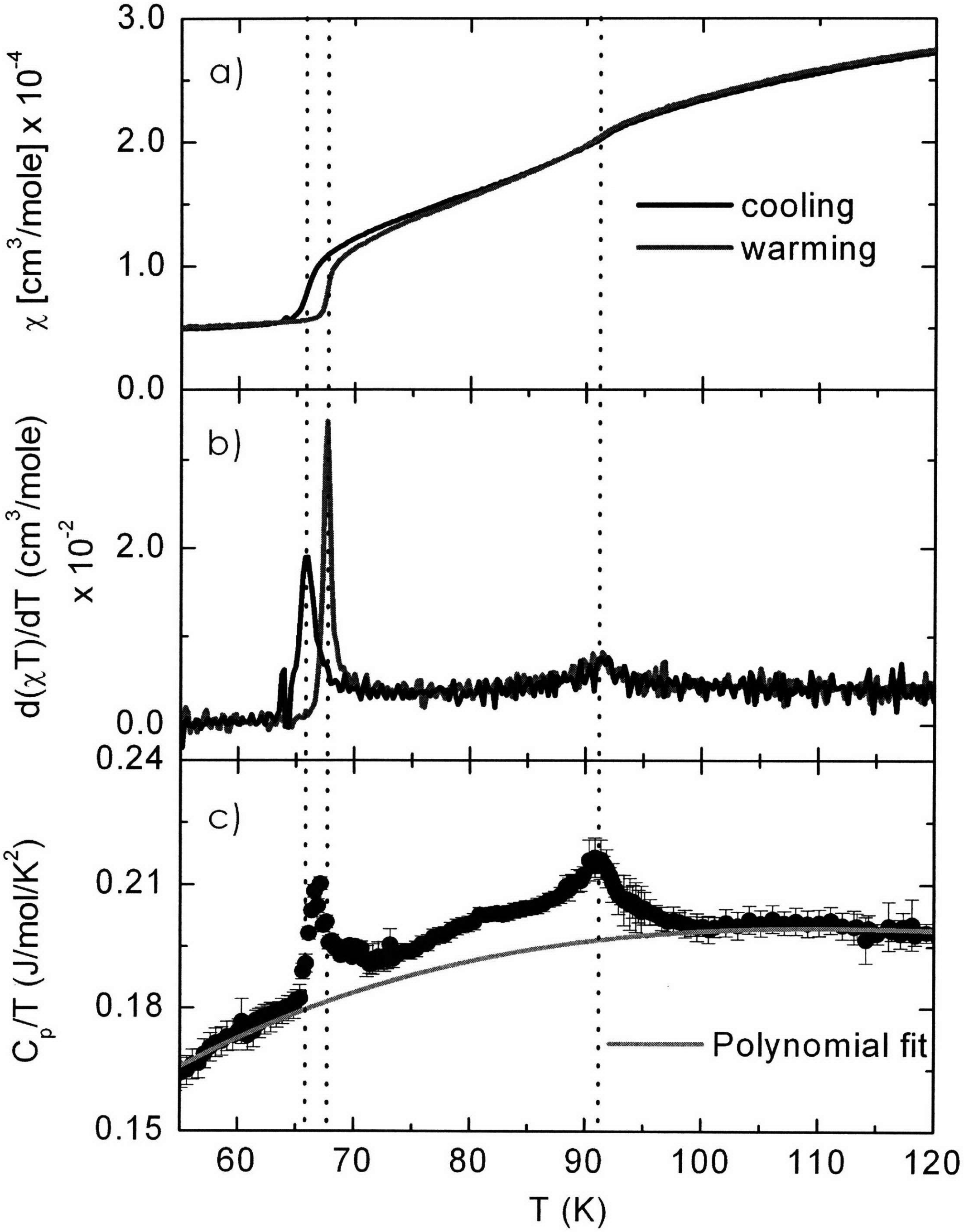

Figure 3-11: a) Magnetic susceptibility upon warming and cooling after the subtraction of a small curie tail. The signature sharp drops at T_{c2}=92 K and T_{c_1} = 66 K (cooling) are clearly present. The quantity $d(\chi T)/dT$ (b) which is proportional to C_p/T, which has peaks corresponding to C_p (c), indicating a magnetic contribution to the total change in entropy at these temperatures.

background in the vicinity of the transition region to a fourth order polynomial. Integrating the region enclosed by the C/T data over temperatures between 65 K and 100 K yields $.04 \pm .02/NK_B$ for the total change in entropy. We note that the primary source of error for this value comes from the estimation of the lattice contribution to the specific heat. Using the expression $S/Nk_B \approx (2/3)(k_BT/J)$ for the entropy of a S=1/2 uniform chain at temperature T [51], with $J/k_B = 660K$ from reference [4], and taking T to be an average of T_{c_1} and T_{c_2} we estimate the maximum available magnetic entropy to be $S/Nk_B = .08$, about a factor of two greater than the measured value. In a similar study, Hemberger et. al. measured a value of $.12 \pm .02$ for S/Nk_b. Our observations are consistent with most of the entropy change for the transition being magnetic in origin.

The specific heat and magnetic susceptibility results provide some insight into the nature of the two transitions. It is known that the entropy change at T_{c_1} and T_{c_2} are both primarily magnetic and that there is hysteresis at T_{c_1} but not at T_{c_2}. With this information, it is tempting to assume that the spin-Peierls transition is actually at 92 K, rather than 65 K, since as of yet there is no published mechanism for hysteresis in spin-Peierls theory. Assuming that T=92 K is the spin-Peierls transition, then all of the data thus far is consistent with the spin-Peierls story. However, it is not conclusive. Singlet formation alone is not enough for spin-Peierls. There must also be a lattice dimerization along the chain direction associated with the transition. The ideal probe to measure such a lattice distortion is a four circle diffractometer on a synchrotron x-ray beamline.

3.3 Study of Low Temperature Distortions using Elastic X-ray Scattering

All of the elastic scattering data presented in this work were measured at the NSLS, at beamlines X20 and X22, both of which are hard x-ray ($5 \leq E \leq 30$keV) bending magnet beamlines, and are equipped with four circle spectrometers like the one in section 2.2.3. The various rotational angles referred to in this section are as defined in section 2.2.3. The sample was glued to a custom made sample holder using GE varnish ^{TM},

which was then screwed to the end of a closed-cycle cryostat for cooling. The temperature was controlled by a Lakeshore temperature controller, which was precise to within 0.2 K. All measurements were taken in transmission geometry which provided access to a greater range in reciprocal space. The chain dimerization is a unit-cell doubling lattice distortion, resulted in new reciprocal lattice points forming at half integer positions along the dimerization direction. This was the starting point for our x-ray exploration.

3.3.1 Lattice Distortions and Superstructures

Single Unit Cell Distortions

Generally speaking the lattice measured at room temperature is different from the T=2K lattice. This is because at room temperature, there are lattice vibrations which

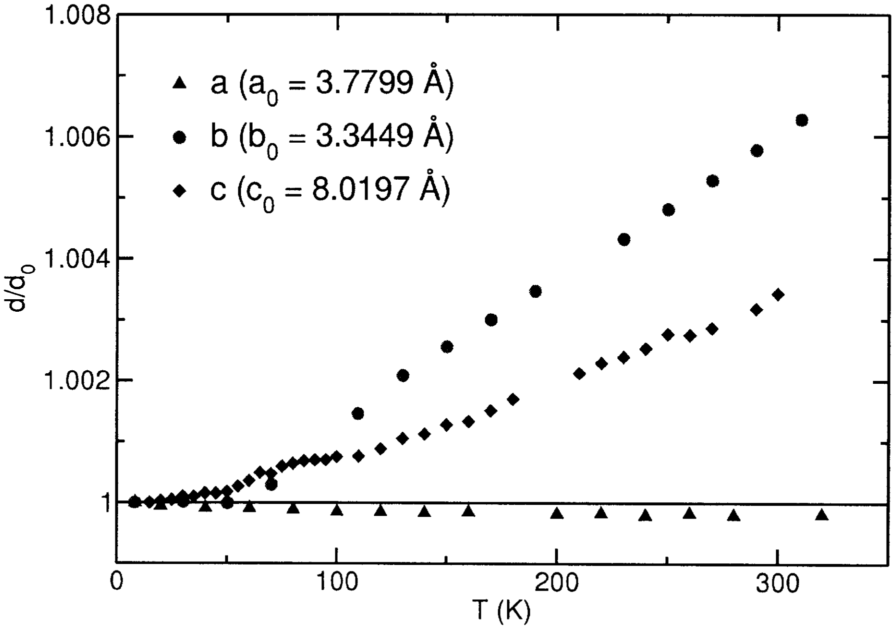

Figure 3-12: Plot of the thermal expansion for each lattice constant in TiOCl. The structural details are discussed in section 1.4.

tend to smear out weak interactions, resulting in a time averaged potential leading to the room temperature lattice. Cooling the material reduces these vibrations until at T=0 K, they are effectively zero. This leaves room for other interactions to affect the atomic arrangement. In the simplest case, the crystal symmetry is maintained, but interatomic spacing changes, resulting in a unit cell of different size. High resolution x-ray scattering is the ideal probe to measure this effect. Changing the atomic spacing correlates to changing d in Bragg's law (equation 2.26)

$$\lambda = 2d\sin\theta,$$

resulting in a change in the measured value of θ. If θ is measured along a principal crystal axis, then d is a multiple of that lattice constant. Therefore by measuring the scattering angle as a function of temperature along each of the principal axes the thermal expansion of the lattice can be calculated. Figure 3-12 shows the measured lattice expansion as a function of temperature for the compound TiOCl (see section 1.4).

In other types of structural changes, atoms will change position within the unit cell as a function of temperature. If an atom is displaced from a high symmetry position, this can change the crystal symmetry, resulting in an observable change in the diffraction pattern. If the atomic movement does not change the crystal symmetry, then it is more complicated to detect, since this will only change that atom's contribution to the structure factor, an can therefore only be detected through a careful measurement of the scattered intensity.

To best illustrate these concepts, we can examine the the shifting of atomic positions within a simple 2D lattice, shown in figure 3-13. The undistorted lattice shown in a) has rhomboidal symmetry. The unit vectors point from one atom to each of its nearest neighbors. The rectangular unit cell drawn is not the primitive cell, but it is a periodic unit of the lattice. The distortion in b) changes the symmetry from rhomboidal to rectangular, making the rectangle the new primitive cell. In reciprocal space the triangular reciprocal lattice is still observable, but lower intensity points have appeared at 1/2 integer locations changing the reciprocal lattice to rectangular symmetry. Note, however, if we take had taken the rectangular unit cell to be the primitive cell in a), then the distortion in b) does not change the symmetry, just the relative intensity of the observed peaks. Further movement of the atoms along the same direction will not result in any new reflections, it will only change the relative intensities of the existing ones. In the final example, we examine the distortion in c), for which the rectangular unit cell in a),b) is no longer a periodic unit of the lattice. The new primitive cell is the primitive cell from b) with the a-lattice param-

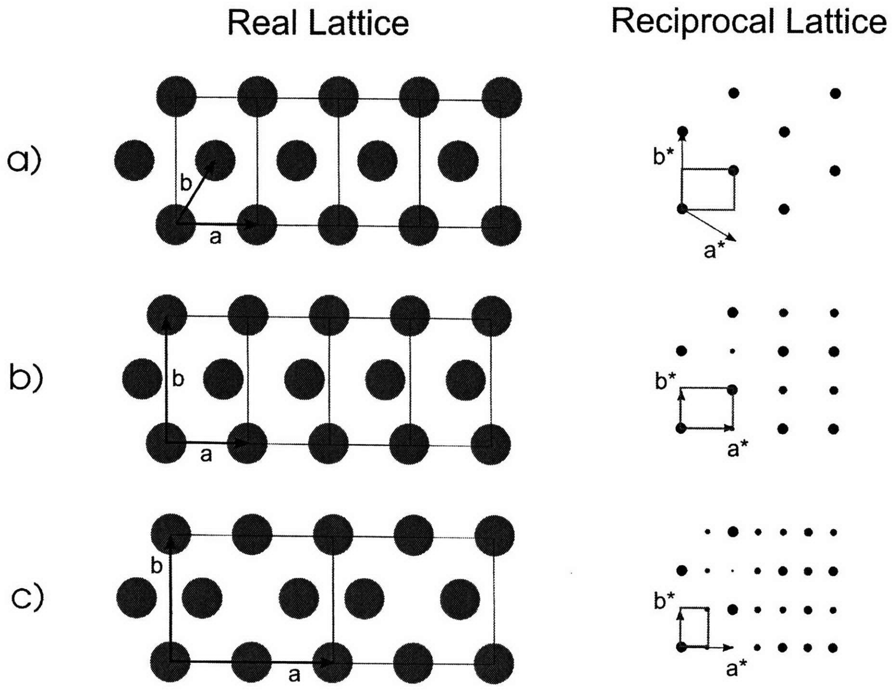

Figure 3-13: Comparison of various real space monatomic lattices with corresponding reciprocal lattices. The size of the reciprocal lattice point is proportional to the relative intensity (as calculated using equation 2.39). a) A 2D rectangular lattice with a 2 atom basis, $R_1=(0,0)$, $R_2=(0.5,0.5)$. In this case the unit cell is bi-layered in both a,b directions, therefore only h,k with h+k=2n are allowed. b) Unit cell preserving lattice distortion, $R_1=(0,0)$, $R_2=(0.6,0.5)$. The main allowed Bragg peaks remain but in addition, some of the forbidden peaks become allowed, albeit with much smaller intensity. c)Unit cell doubling distortion. The doubled unit cell now has a 4 atom basis: $R_1=(0,0)$,$R_2=(0.5,0)$, $R_3=(0.2,0.5)$,$R_4=(0.8,0.5)$. The allowed peaks in the undistorted lattice are the most intense for the doubled unit cell reciprocal lattice. However, new sets of points have filled in the h+1/2 positions, consistent with the doubling along h in real space.

eter doubled. We see that the diffraction pattern is similar to that in b), but with extra reciprocal lattice points at the h+1/2 positions, consistent with the doubling of the unit cell along this direction. There are many examples of unitcell doubling distortions in nature. Section 3.3 discusses such a lattice distortion in TiOCl.

Incommensurate Structures

The last distortion of the previous section (figure 3-13c) is a special example of a much more general type of distortion. Unlike the previous distortions, it could not be described by a single unit cell, rather it extended over two unitcells. We can generalize this to a distortion which involves N unit cells, where N doesn't even have to be a rational number. When the amplitude of a distortion is modulated over N unit cells, this is known as an incommensurate distortion. The analysis of incommensurate structures, can be quite involved. In this section, a few simple examples of incommensurate modulations will be presented along with techniques used to identify them.

Sinusoidal Modulation

We begin with a distortion of the form

$$u(x) = \delta \cos(\pi l a/\lambda), \tag{3.6}$$

where l labels a lattice site, λ is the number of unit cells spanned by one period of the displacement and a is the lattice parameter. The periodicity of the lattice is being modulated by an additional displacement which may or may not be in phase with the lattice. If the modulation is a multiple period of the lattice, it is called a commensurate modulation. The example in figure 3-13 represents a commensurate modulation with $\lambda = 2$ unit cells. There are also modulations which have a wavelength which is not an integer multiple of the lattice, for instance $a\sqrt{17}$. Such modulations are called incommensurate modulations. While it may seem elusive, it is actually straight forward to calculate the scattering intensity from an incommensurate modulation along a single chain of atoms by substituting $x_i + u(x)$ into R_i of equation 2.39.

$$\begin{aligned} S(Q) =& \sum_i e^{i\vec{Q}\cdot(x_i+u(x))} \\ =& \sum_i e^{iQ(x_i+\delta\cos(\pi la/\lambda))} \\ =& \sum_i e^{iQx_i} e^{iQ\delta\cos(\pi la/\lambda)}, \end{aligned}$$

Generally the magnitude of such displacements are small, so the exponential can be expanded for $\delta Q << 1$,

$$\begin{aligned} e^{iQ\delta\cos(\pi la/\lambda)} \approx& 1 + iQ\delta\cos(\pi la/\lambda) \\ =& 1 + i\frac{Q\delta}{2}\left[e^{i\pi la/\lambda} + e^{-i\pi la/\lambda}\right] \end{aligned}$$

Substituting this expansion back into the structure factor, using $q = 2\pi/\lambda$, and $x_i = la$,

$$S(Q) = \sum_i e^{iQx_i} + \frac{Q\delta}{2}\left[e^{i(Q+q)x_i} + e^{i(Q-q)x_i}\right], \tag{3.7}$$

we see that the incommensurate modulation results in peaks appearing at $Q+q$ and $Q-q$ in reciprocal space. A computer generated numerical simulation of the structure factor for a sinusoidal modulation (not using approximation 3.7)of the atomic spacing along a linear chain of 2000 atoms is shown in figure 3-14.

Square Wave Modulations

Not all modulations are smoothly varying functions like the sine function. One example is the case where a system spontaneously forms ordered domains which are out of phase with one another. In our linear chain example constructing such a modulation would require shifting $\lambda/2$ atoms by $+\delta$, then shifting the next $\lambda/2$ atoms by $-\delta$, creating a modulation which is essentially a square wave, of wavelength λ. While analytical forms for a square wave exist[52], they aren't straight forward to apply to

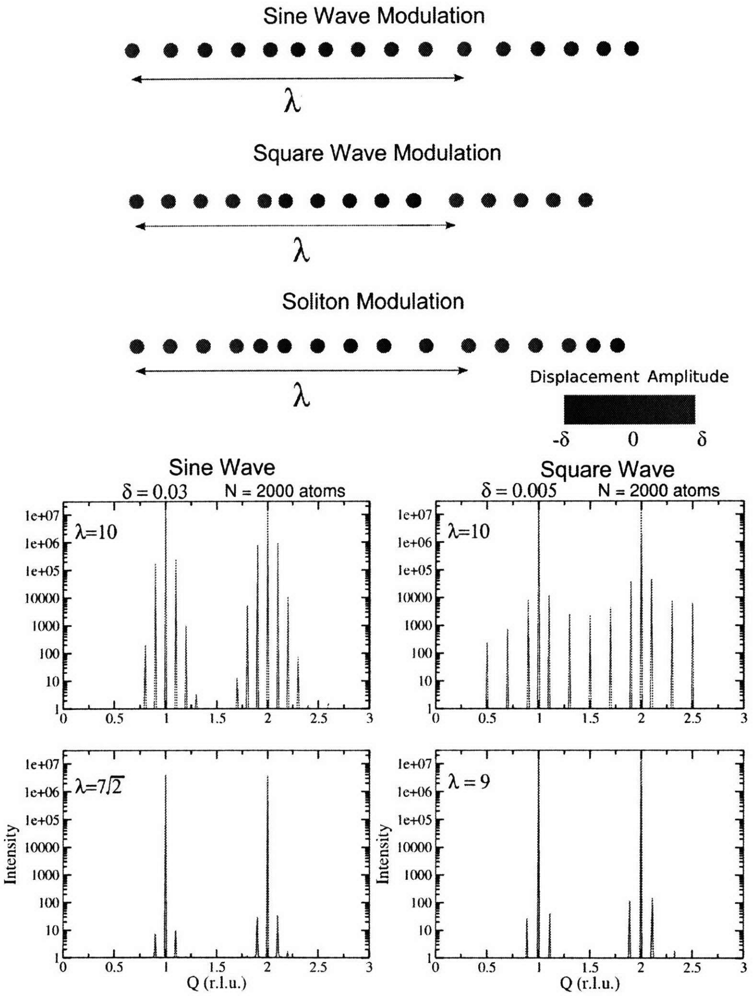

Figure 3-14: Schematic representations of various lattice modulations, along with the corresponding exact numerical diffraction pattern (direct structure factor calculation, i.e. no expansions). In the atomic chains, the atomic color is representative of the displacement magnitude, red=δ, blue=$-\delta$. In the third displacement pattern the stationary atom separating the domains is known as a soliton [5]. The upper plots for the sine and square waves show the diffraction from a modulation which is an integer multiple of the unit cell and is therefore commensurate. Note that the intensities are plotted on the same scale but the modulation amplitude for the square wave is nearly a factor of ten less than that of the sine wave. In the lower frame of the sine modulation, the wavelength is simply an incommensurate multiple of the unit cell. For the square wave, an incommensurate modulation is difficult to interpret, since by definition a square wave is discrete, and therefore must always be commensurate. By choosing an odd number the wavelength, $\lambda = 9$, the modulation is a mixture of 4,5 for $\lambda/2$ lengths.

this analysis. However using the Fourier expansion for the square wave [52],

$$f(x) = \frac{4}{n} = \sum_{n=1,3,5,\ldots} \frac{1}{n} \sin\left(\frac{2n\pi x}{\lambda}\right), \tag{3.8}$$

a relatively straight forward solution presents itself. Now instead of a single sine function the modulation is a sum of sine functions, which can be treated in a manner identical to the derivation of equation 3.6. The scattering from a square wave modulation is therefore

$$S(Q) = \sum_i e^{iQx_i} + \frac{2Q\delta}{\pi} \sum_{n=1,3,5,\ldots} \frac{1}{n}\left[e^{i(Q+q_n)x_i} - e^{i(Q-q_n)x_i}\right], \tag{3.9}$$

where $q_n = 2n\pi/\lambda$. The diffraction pattern from two different wavelength square wave modulations is shown in figure 3-14 along with comparable sine wave modulation diffraction patterns. The clear differences are that the square wave modulation results in much more intense satellite peaks relative to the main Bragg peak (the amplitude of the modulation used is almost ten times less for the square wave modulation). In addition, the sine wave contains all harmonics, whereas the square wave clearly has only odd ones. In addition the ration of the intensities of the higher harmonics to the first one is larger for a square wave. These differences are more pronounced for the commensurate modulations in the upper panels. The incommensurate modulation isn't well defined for a square wave, since by definition a square-wave is a discrete modulation. By setting $\lambda = 9$, the modulation contains a mixture of $\lambda/2 = 4, 5$ domain sizes, which is the closest approximation to an incommensurate square-wave modulation.

The Soliton

In a sense the square wave modulation is an intellectual construction, since in real systems changes tend to be more gradual. The final atomic arrangement in figure 3-14 shows domains of displaced atoms separated by one which remains stationary. The stationary atoms, called *solitons*[5], form a sub-lattice for which thermodynamic properties[53], waveforms, and diffraction patterns can be calculated[54]. Solitons have been experimentally observed in many systems, Polyacetylene [55], TTF-CuBDT[56], and $CuGeO_3$ [54] to name a few. Because of this, it is worth discussing the soliton modulation in addition to the sine and square waves.

The analytical form for a soliton is given by[57],

$$u(l) = \delta sn(\frac{la}{\Gamma k}), \tag{3.10}$$

where $sn(x)$ is the Jacobi elliptic function of the first kind, l labels a lattice site, with spacing a. The parameters Γ and k are soliton specific properties, requiring a brief discussion of the Jacobi Elliptic function. Here only enough will be discussed to understand how it applies to scattering. If interested the reader is directed to [58][59]. To understand $sn(\phi)$, we first need to define the function

$$u(\phi, k) = \int_0^\phi \frac{dt}{\sqrt{1 - k^2 \sin^2 \phi}}, \tag{3.11}$$

which formally is the *incomplete elliptic integral of the first kind.* The Jacobi elliptic function is the inverse of $u(\phi, k)$,

$$sn(u, k) = sin(\phi, k).$$

. The variable k is a parameter known as the *elliptic modulus*, and it has a value $0 \leq k \leq 1$. From equation 3.11, if $k = 0$, then the $u(\phi, 0) = \phi$, therefore, $sn(u) = sn(\phi) = sin(\phi)$, and the Jacobi Elliptic Function becomes a sine curve. In the limit $k \rightarrow 0$, it is less clear what happens. The integrand of $u(\phi, 1)$ becomes singular for $\phi = n\pi/2$, meaning that $sn(\infty, 1) = 1$. It is also easy to deduce $u(0, 1) = 0$. Beyond this it is difficult to get a feel for the function, therefore it is convenient to turn to numerics. Conveniently, Wolfram's Mathematica Software has an $sn(x, k)$ function, and while it blows up for $k = 1$, for $k = 1 - 10^{-}9$, $sn(x, k \rightarrow 1)$ resembles a long wavelength square-wave. This tells us that roughly speaking $sn(x, k)$, is a function which can be continuously tuned from sine wave to square wave using the parameter

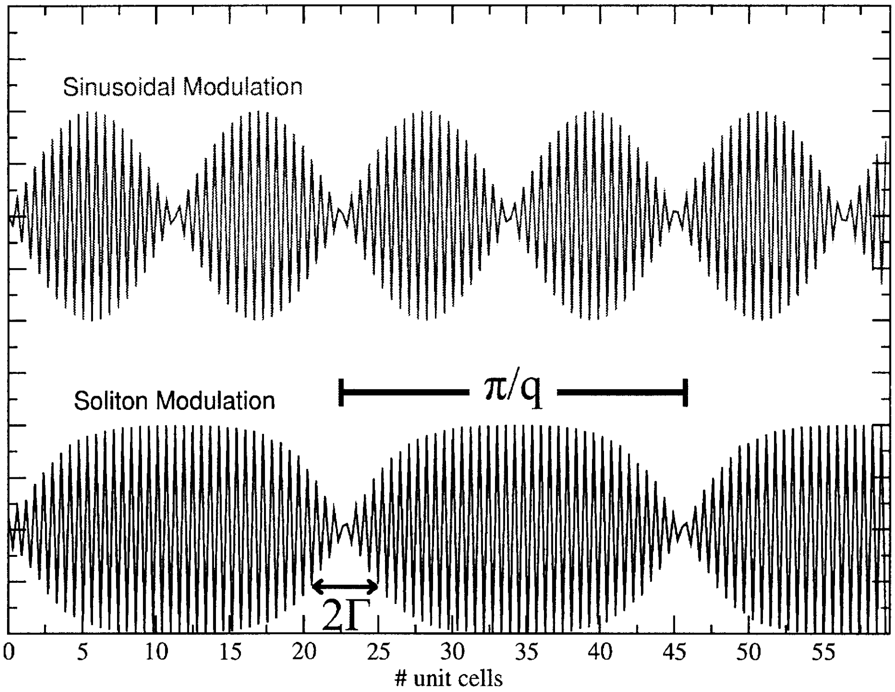

Figure 3-15: Red curve is a sinusoidal modulation along with a soliton modulation. The soliton width Γ is defined along with the soliton separation given by π/q, where q is the position of the observed satellite peak in reciprocal space.

k. This defines k in equation 3.10.

How does this apply to solitons? Figure 3-15 compares a rapid oscillation modulated by sine and soliton functions. From this plot we can now define Γ from equation 3.10 as the soliton width. What we also get from figure 3-15 is the value $\lambda/2 = \pi/q$ is the inter-soliton distance. The relationship between λ and Γ is[54]

$$\frac{\pi}{q} = 2kK(k)\Gamma \tag{3.12}$$

where $K(k) \equiv u(\pi/2, k)$ is the *complete elliptic integral of the first kind.*

Harmonic Analysis of Incommensurate Scattering Peaks

In figure 3-14 we saw that the relative intensities of the harmonics due to scattering from a sinusoidal and square-wave modulation vary significantly. It turns out that a quantitative measurement of the harmonic ratios can be used to deduce the wave form of the modulation. In section 3.3.1, an analytical expression for the diffraction pattern from a square wave modulation was derived using the Fourier expansion. This approach can be applied to any function if the Fourier expansion is known. The general form for the scattered intensity from a a periodic modulation $u(x)$ is [54]

$$I_n \sim \left(\int_0^{\pi} d\theta \sin(n\theta) \sin\left[Q\, u(x)\right] \right)^2, \tag{3.13}$$

where $\theta = qx$, and $q = 2pi/a$ is the reciprocal lattice vector of the harmonic peak position relative to the nearest Bragg peak. The displacement modulation, $u(x)$ can be expanded into it's Fourier components $u(x) = \sum_m a_m \sin(m\theta)$. The $m = 1$ term corresponds to a simple sine wave modulation. The expected ratio of the 3rd to 1st harmonics can then be calculated by making the substitution $u(x) = \delta sin(qx)$ into equation 3.13, then calculation I_n for $n = 1$ and $n = 3$. value for I_3/I_1 can be calculated,

$$\begin{aligned}
\frac{I_3}{I_1} &= \left(\frac{\int_0^{\pi} \sin 3\theta \sin\left[Q\delta \sin\theta\right]}{\int_0^{\pi} \sin\theta \sin\left[\delta Q \sin\theta\right]} \right)^2 \\
&\approx \left(\frac{\int_0^{\pi} \sin 3\theta \left[Q\delta \sin\theta - (Q\delta)^3 \sin^3\theta/6 + ...\right]}{\int_0^{\pi} \sin\theta \left[Q\delta \sin\theta + (Q\delta)^3 \sin^3\theta/6...\right]} \right)^2 \\
&\approx \left(\frac{\int_0^{\pi} \sin\theta (Q\delta)^3 \sin^3\theta/6}{\int_0^{\pi} \sin\theta Q\delta \sin\theta} \right)^2 = \frac{(Q\delta)^4}{576},
\end{aligned}$$

where the second sine function has been Taylor expanded for $Q\delta << 1$. For I_1, the $(Q\delta)^3$ term has been dropped since $(Q\delta)^3 << Q\delta$. For I_3 the 3rd term was necessary since

$$\int_0^{\pi} \sin m\theta \sin n\theta = \begin{cases} 0, m \neq n \\ \frac{\pi}{2}, m = n \end{cases} \tag{3.14}$$

The factor of 576 results from the integration. From this exercise we expect the ratio I_3/I_1 for a sinusoidal modulation to go like

$$\frac{I_3}{I_1} \sim \frac{(Q\delta)^4}{576}. \tag{3.15}$$

For the example in figure 3-14, $\delta = 0.03$ and $Q = 2$, therefore, $(Q\delta)^4 = 2.25 \times 10^{-8}$, which is consistent with the I_3/I_1 ratio for a similar value for $Q\delta$ from reference [54]. Comparing the ratio of the intensities of the third and first harmonics for the plots in figure 3-14 we see that the ratio is $\sim 10^{-6}$, which is due to the finite chain size used. By repeating the simulation for 10^5 atoms, I was able to recover the proper I_3/I_1 ratio.

Now that the sinusoidal ratio has been calculated, the square wave ratio is relatively straight forward. As usual we expand the second term in powers of $(Q\delta)$. In section 3.3.1, we already expanded the square wave in terms of its harmonics. Because of equation 3.14, the square wave expansion is truncated to the 3rd and 1st order terms for the numerator and denominator respectively. This is the major difference from the sine function, since the $(Q\delta)^3$ in the Taylor expansion was necessary for the numerator to be non-zero. In the square wave case the integrals as well as the $Q\delta$ terms cancel, making I_3/I_1 proportional to the ratio of the a_3 and a_1 Fourier coefficients of the square wave, (1/3), leaving

$$\frac{I_3}{I_1} \sim \left(\frac{a_1}{a_3}\right)^2 = 1/9 \sim 10^{-1}. \tag{3.16}$$

Indeed this is consistent with figure 3-14, even for a chain of 10^5 atoms.

The harmonic ratio of the soliton modulation is a little trickier, but follows the same procedure. To get the Fourier coefficients, $sn(x,k)$ must be expanded in the *nome*[59], Y, defined by

$$Y = e^{-\pi \frac{K(\sqrt{1-k^2})}{K(k)}},$$

where $K(k)$ is the complete elliptic integral of the first kind defined in section 3.3.1. The coefficients of the expansion are

$$a_{2m+1} = \frac{Y^{(2m+1)/2}}{(1 - Y^{2m+1})}.$$

Following the same procedure for the sine and square waves, to find the ratio I_3/I_1, requires finding the ratio a_3/a_1[54].

$$\frac{I_3}{I_1} = \left(\frac{Y}{Y^2+Y+1}\right)^2. \tag{3.17}$$

With this we have the tools to evaluate the relative intensities of the most common periodic oscillations. In section 3.3.5 this technique will applied to characterize an incommensurate modulation in the compound TiOCl.

3.3.2 Commensurate Superlattice Peaks

Upon cooling the sample to base, we found a superlattice peak at the (0 2.5 0) position. Scans along and perpendicular to the chain are shown in figures 3-17(a) and (b) respectively. A comparison of the fitted peak width to that of the (0 2 0) Bragg peak showed the (0 2.5 0) to be resolution limited in both directions, meaning the dimerization is long range over a length scale comparable to the beam size ($\sim 1mm$). The weak shoulder in the transverse scan (b), is due to crystal mosaic which, depending on the sample used, ranged from 0.2-1.5 degrees (in θ). We also explored other reciprocal lattice positions and found that the new reciprocal lattice to be essential the same as the undimerized reciprocal lattice, but with new reciprocal lattice points at (h k+1/2 l). So the change in symmetry is similar to the example illustrated in figure 3-13.

To estimate the degree of dimerization, our initial inclination was to compare the (0 2 0) and (0 2.5 0) integrated intensities. This proved meaningless, however, since

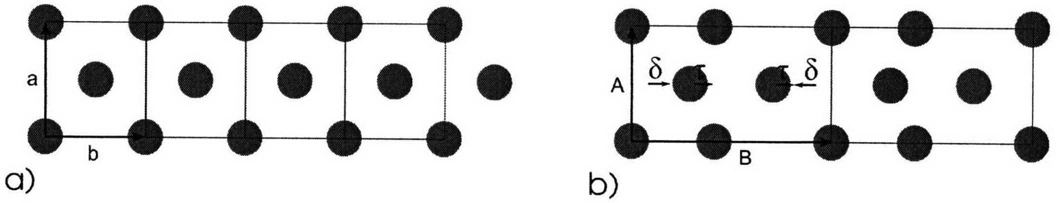

Figure 3-16: Schematic drawing of the model lattice used to fit the measured peak intensities. The supercell has dimensions (A,B,C)=(a,2b,c). The adjustable fitting parameters were the dimerization magnitude, δ, and a relative translation of neighboring chains, τ.

the (0 1.5 0) superlattice peak was an order of magnitude more intense than (0 2.5 0). We therefore measured the integrated intensities of about 45 Bragg and superlattice peaks, and fitted them to the x-ray structure factor (equation 2.39 of an orthorhombic unit cell with lattice parameters, A=a,B=2b,C=c, where a,b,c are the undimerized lattice parameters (figure 3-16). The adjustable parameters illustrated in figure 3-16b were the dimerization distance (δ) and a relative shift of one chain with respect to the other (τ). The parameter τ was necessary since it isn't clear how one chain dimerizes with respect to its neighbor (see discussion of figure 3-26 in section 3.3.3). The fit converged on values $\delta = 0.1 \pm 0.07$Å, and $\tau = 0.17 \pm 0.1$Å. In principle 45 peaks should yield better certainty than this. The most likely cause for this uncertainty is the non-uniformity of the crystal. This introduces an orientation dependent intensity which cannot be accounted for theoretically. Our model was also reduced to the movement of only Ti^{3+}. In reality the O^{2-} and Cl^{-} ions are also most likely displaced but our poor sample quality made resolving these movements impractical. Because Ti^{3+} is both the magnetic ion and strongest scatterer of x-rays, it is reasonable to assume that the observed structure factor is dominated by Ti^{3+} movement. Subsequent to our measurement, Shaz et. al.[60]. performed a single crystal refinement of the low temperature structure, and found changes in the O,Cl positions comparable to the change in Ti positions. They report a δ of 0.18Ådimerization. While they don't report it explicitly, it is possible to extract τ from the structural information provided. We estimate their value of τ to be about 0.1Å. The temperature dependence of the integrated intensity of the (0 2.5 0) peak is shown in figure 3-17c. There is clear, sharp drop to zero at about T=65 K. which corresponds to T_{c_1} in our thermodynamic measurements. In the language of phase transition physics, the peak intensity serves as an *order parameter*, or some characteristic which is quantifiably different on either side of the transition. In a water to ice transition the order parameter would be the density, for instance. The order parameter for the transition at T_{c_1} in TiOCl is unlike that of spin-Peierls systems observed in the past, which had more classic mean-field power law type behaviors. In addition, the peak intensity exhibited a thermal hysteresis, with a width comparable to that observed in the magnetic susceptibility.

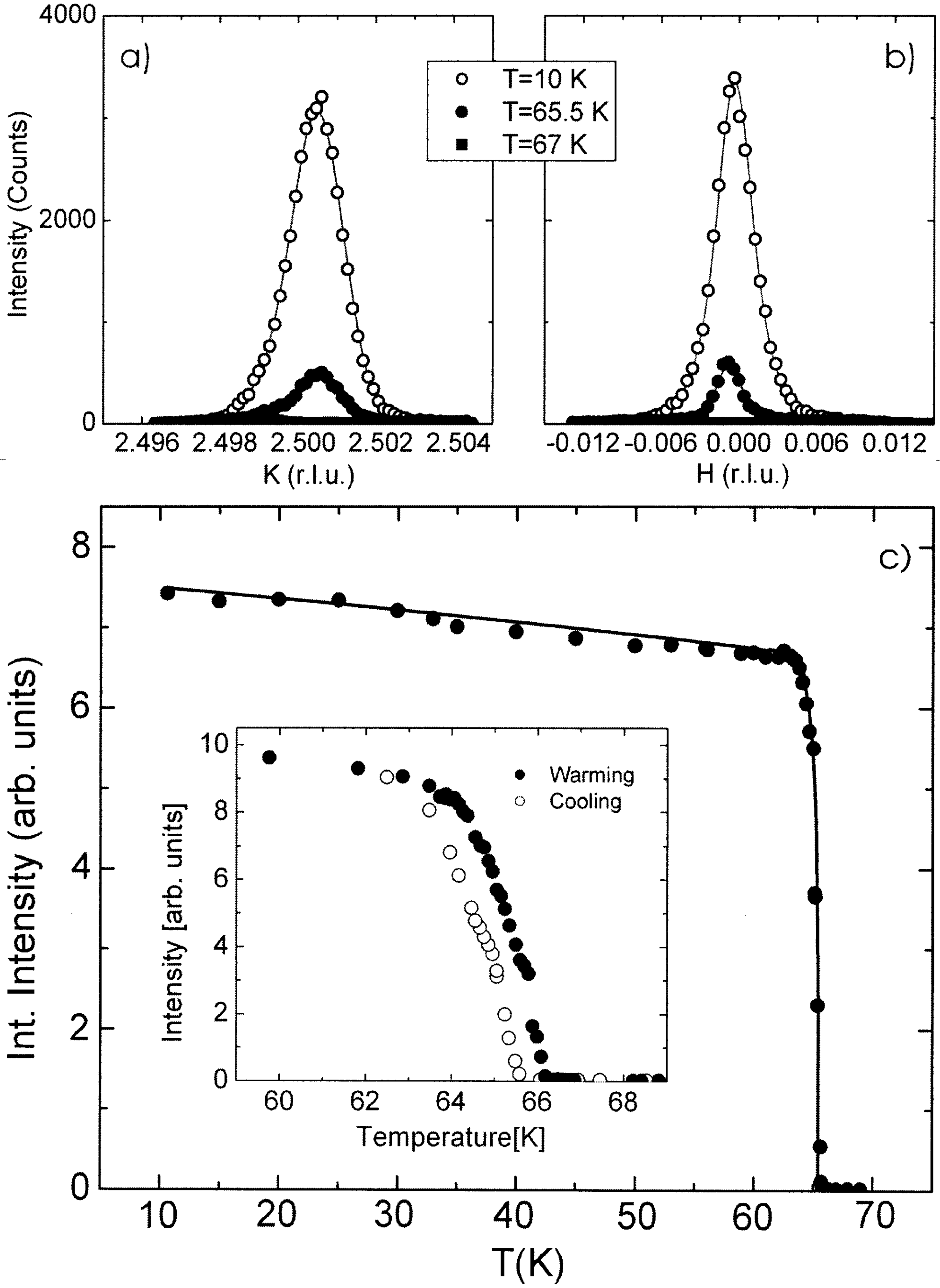

Figure 3-17: Longitudinal (a) and transverse (b) scans through (0 2.5 0) the commensurate position along with the temperature dependence of the integrated intensity (c), which exhibits a thermal hysteresis with a width comparable to that of the magnetic susceptibility (c inset). The line through the data in c) is a guide to the eye.

In our initial measurements we found no evidence for any structural change at T_{c_2}. The conclusion was then that the lattice dimerization at T_{c_1} was spin-Peierls-like, but it wasn't safe to label the transition spin-Peierls until we sorted out the origin of the first order behavior of the transition.

3.3.3 Incommensurate Superlattice Peaks

In one experiment we were trying to acquire a detailed characterization of the order parameter upon warming. We followed the peak intensity through T_{c_1}, and found that at about T=70 K, well above T_{c_1}, the superlattice peak was still present, and with significant intensity. Our initial thought was that something was wrong with the temperature sensor, but we later noticed that the values of H,K were several resolution widths away from the (0 2.5 0) position. Thinking we had lost alignment, we drove the instrument back to the (0 2 0) Bragg peak, to find that it was still perfectly aligned. We went back to the superlattice peak and warmed the sample a little more, which caused the peak to move. We then tried tried a long H scan which revealed another peak a symmetric position about the H-axis. At this point we realized that we had discovered a novel set of superlattice peaks which were at positions incommensurate with the lattice. Figure 3-18 shows a series of scans along the H

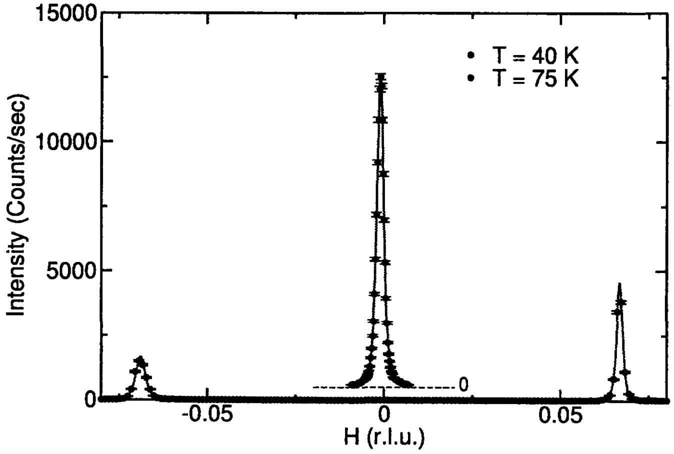

Figure 3-18: Long scans along H showing the incommensurate and commensurate peaks present at different temperatures. The commensurate scan has been offset from zero for clarity. The incommensurate scan is at a K of 2.492.

direction through the commensurate and incommensurate positions. The peaks are well separated at T=66.5 K. Upon cooling the separation decreases until at T=63 K (T_{c_1} for cooling), they seem to have merged into the commensurate position. A more quantitative study of the temperature dependence of all of the fitted peak parameters is summarized in figure 3-19. Upon cooling through T_{c_2}, peaks appear at positions (H+±0.08,K±.012,0) (figure 3-20, bottom frame). As the system is cooled further, the peaks continuously move toward the commensurate superlattice position where they merge at T_{c_1}.

In section 3.3.1 several different lattice modulations were presented along with their respective diffraction patterns. The commensurate peak observed below T_{c_1}can be considered to be due to a two unit cell ($\lambda = 2$) modulation. If we now consider the diffraction pattern due to a harmonic modulation with a wavelength slightly larger or smaller than 2 by an amount δ, the peak at q=0.5 position will split into two new peaks with positions given by

$$q = \frac{2\pi}{a(2+\delta)} = \frac{2\pi}{a}\frac{1}{2\left(1+\frac{\delta}{2}\right)} \approx \frac{\pi}{a}(1-\frac{\delta}{2}) = q_c - q_c\frac{\delta}{2},$$

where q is the wavevector of the incommensurate peak reduced to the Brillouin Zone, and q_c is the commensurate q-vector. From this the incommensurate peak positions relative to the $q_c = 0.5$ will be $q_c\delta/2 = \delta/4$. Along the H direction the peak splitting is about the Brillouin zone center, therefore the corresponding modulation will have a wavelength given by $1/\delta H$, where δH is the incommensurate peak position in reciprocal space. From figure 3-19, just below $T_{c_2}$the incommensurate wavevectors are $\lambda_b = 2.06$, and $\lambda_a = 12.5$ for the b and a directions respectively.

The inset in the ΔH plot shows the exact theory for the temperature dependence of $\Delta Q = \sqrt{(\Delta a^*)^2 + (\Delta b^*)^2}$:

$$\delta\,(t) = 4.62/[4.61 + ln(1/t)], \tag{3.18}$$

where $t = (T - T_{c1})/(T_{c2} - T_{c1})$ is the reduced temperature, $\delta(t) = \Delta Q(t)/\Delta Q(t=1)$. This expression was derived by W.L. McMillan using a mean field expansion of the lattice free energy to help understand the incommensurate to commensurate lock-in transition in charge density wave modulations. The basic assumption of McMillan was that the energy due to small deviations from the locked in commensurate wavelength can best be minimized by creating a long-wavelength phase (rather than amplitude) distortion[6].

Unlike the commensurate superlattice peak order parameter, the incommensurate order parameter has a gradual onset, with no thermal hysteresis. A second order phase transition characteristic is the power law order parameter behavior, the exponent of which determines the universality class. The red line in figure 3-19a is a power law fit of the integrated intensity

$$I(T) = a(T - T_c)^{\beta}. \tag{3.19}$$

The value of β converged on $\beta = 0.3 \pm 0.1$. After the onset of the incommensurate peak, the intensity continues to increase, leveling off at its maximum value at about T=75 K. The intensity remains constant as the sample is cooled toward T_{c_1}. Just below T=70 K (indicated by the vertical dashed lines in figure 3-19) the systems enters a region in which it was difficult to distinguish between commensurate and incommensurate peaks. In fact, it was unclear whether or not there was a coexistence of incommensurate and commensurate phases. To clarify this H,K mesh scans were taken around the incommensurate/commensurate regions at temperatures approaching T_{c_1}.

Figure 3-20 contains intensity maps over the scanned regions, showing the evolution from incommensurate to commensurate upon cooling. A log scale is used to make all of the peaks clearly visible, but this also has the unfortunate side effect of enhancing the diffuse scattering in the peak tails. The important aspect to focus on is the most intense core of each peak, which shifts continuously toward the commensurate position as $T \rightarrow 65K$. Figure 3-21 shows a mesh scan over a large area which reveals higher harmonics of the reflection. These harmonics give us a possibility to model the incommensurate modulation, which will be discussed over the next two

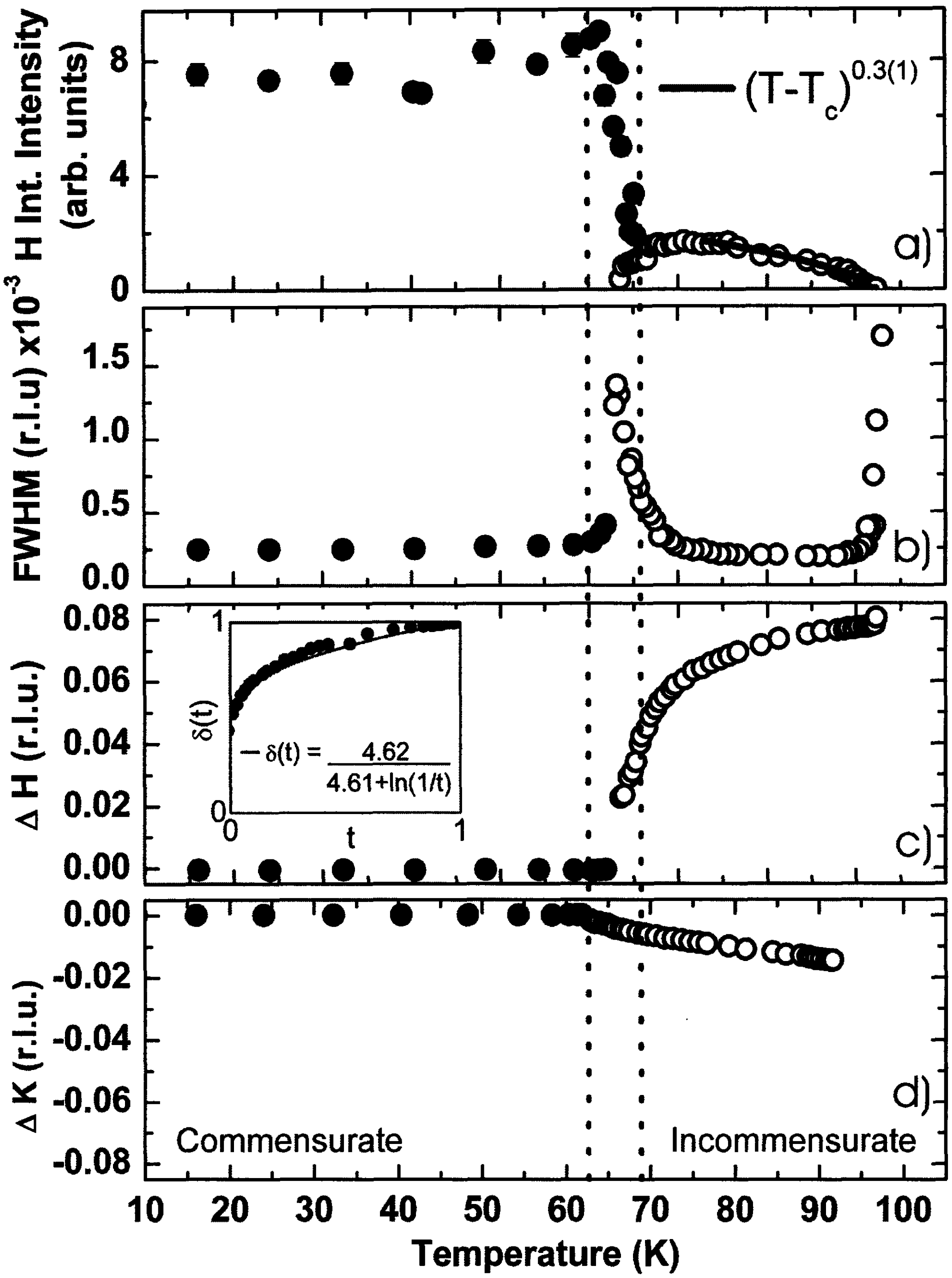

Figure 3-19: Temperature dependence of fitted peak parameters for commensurate and incommensurate temperature regions. The incommensurate intensity in figure a is fit to a power law $(T - T_c)^{\beta}$. The FWHM quoted in figure b, is that along the H direction. Along K, the peak remained resolution limited. The inset of figure c shows the parameter δ, which is the change in wavelength of the incommensurate modulation along with the exact theoretical model of McMillan ([6]).

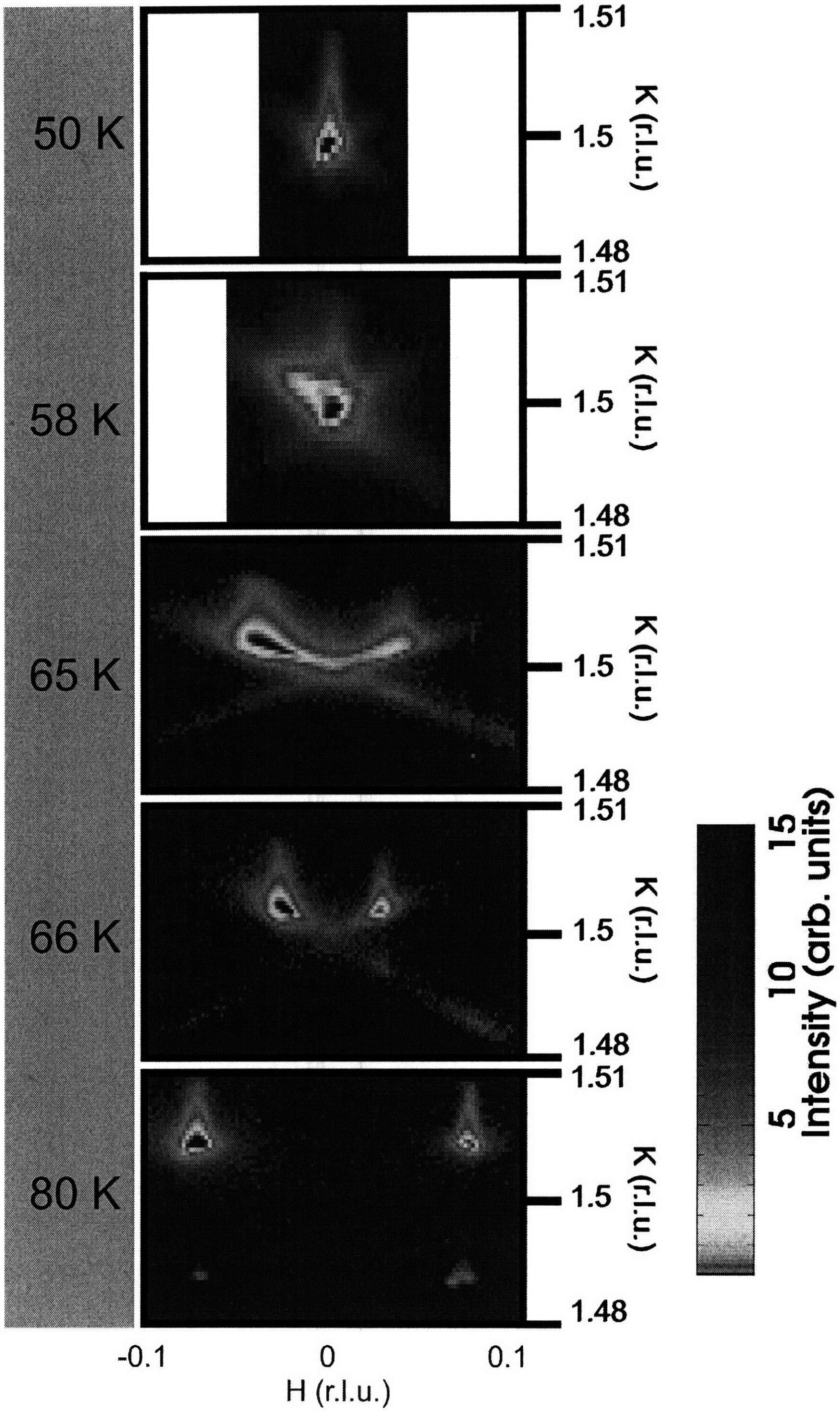

Figure 3-20: Mesh scans showing the temperature evolution from incommensurate to commensurate. The scale is a log scale, so much of the width is most likely due to low intensity diffuse scattering.

sections.

3.3.4 Modelling of the Incommensurate Modulation

In section 3.3.1 three different modulation wave forms were investigated, a sine wave, a square wave and a soliton. Each of this results in a pattern of equally spaced satellites, with the difference in each modulation type manifesting itself in the ratio of the intensities of the higher harmonics to the first harmonics. The procedure for modelling the incommensurate modulation will be to first find the simplest model to reproduce the observed diffraction, for which all modulation forms are equivalent. The waveform can then be refined by analyzing the ratio of the observed harmonics. Conceptually, the simplest modulation is a square wave, which corresponds to an arrangement of anti-phase domains, where the domain wall spacing gives the incommensurate wavevector. In the case of a dimerized lattice two anti-phase domains are always separated by a single undimerized atom (see figure 3-22). The incommensurate wave vector is then given by the soliton spacing. In the case of TiOCl, we observe satellites in both the H and K directions, therefore implying a 2D soliton lattice. If we consider the solitons like atoms, and compare the diffraction patterns of the atomic

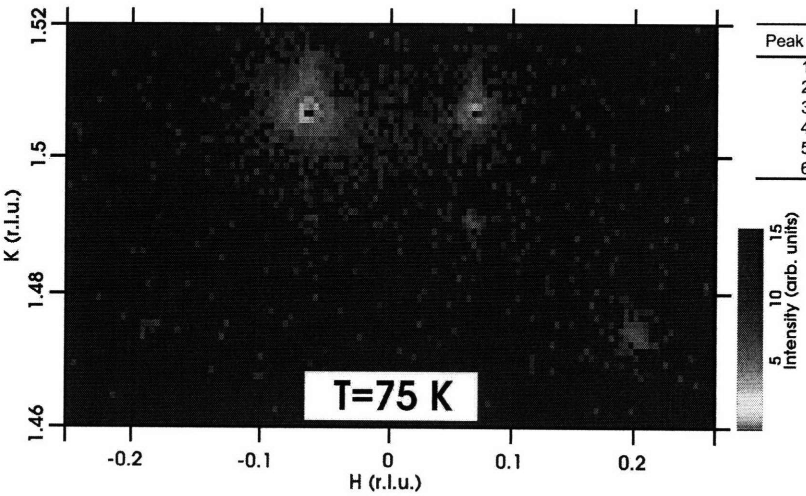

Peak	H (r.l.u.)	K (r.l.u.)	Rel. Intensity
1	-0.0653(1)	1.50778(4)	3665 ± 15
2	0.0682(1)	1.50768(8)	3665 ± 12
3	-0.067(3)	1.4908(2)	9 ± 1
4	0.0670(7)	1.4910(2)	22 ± 2
5	-0.188(4)	1.4750(5)	1.0 ± 0.7
6	0.1982(4)	1.4740(1)	32 ± 2

Figure 3-21: Mesh scan showing the first and third harmonics on the $-\Delta K$ side of the commensurate position. No third harmonics were observed on the $+\Delta K$ side (see text). The table contains the positions and relative intensities of each of the observed peaks. The peaks are numbered from right to left and top to bottom.

arrangements in figure 3-13, we can see that in order to get diffraction along the diagonal the soliton lattice symmetry has to be rhomboidal, rather than rectangular. This can be done by shifting the solitons on neighboring chains with respect to eachother. This is a nice model conceptually, however, as discussed in section 3.3.1, a square-wave modulation can never be truly incommensurate. The temperature dependence of the incommensurate wavevector in figures 3-19c,d requires that the modulation be incommensurate, meaning this simple soliton picture cannot apply. We therefore turn to the sine function to model the incommensurate modulation, which has no restriction on the choice of incommensurate wavevectors. The modelling of the incommensurate structure with the sine wave is shown in figure 3-23. The core of the model is the sinusoidal shape of the commensurate state, where the atom sits at an extremum of the sine wave with wavelength $\lambda = 2$. The incommensuration along K can then be obtained by making the wavelength slightly larger than 2. In figure 3-23, $\lambda = 2.04$ is used. The reflections in figure 3-21 are also asymmetrically weighted about the $K = 1.5$ axis which can be reproduced by phase-shifting one chain with

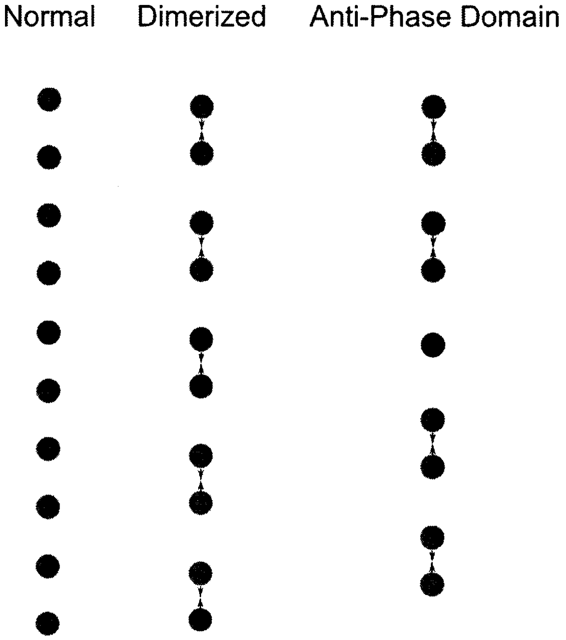

Figure 3-22: Cartoon showing that the boundary between two anti-phase domains in a dimerized lattice is a single undimerized atom, known as a soliton. The soliton spacing gives the incommensurate wavevector.

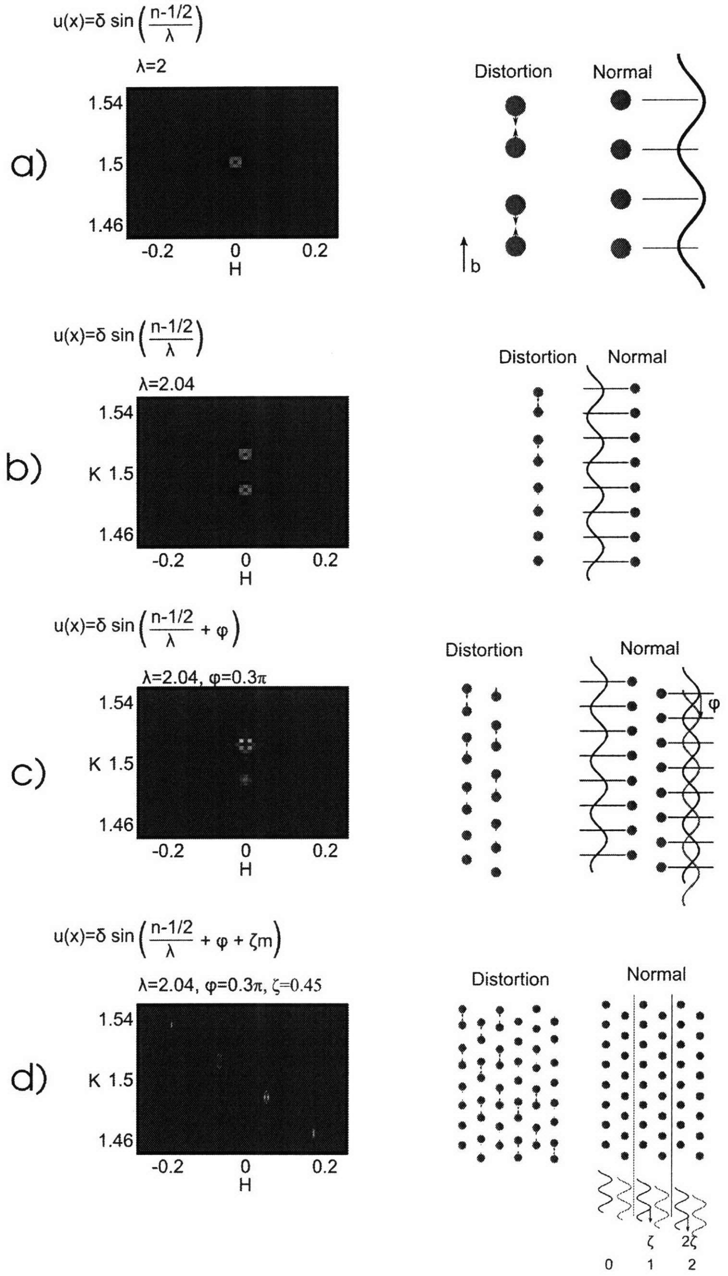

Figure 3-23: The commensurate state can be modelled by a sine wave with the extrema centered on the atomic positions (a). To get a splitting about the commensurate position along the b-direction, the wavelength of the sine wave can be made slightly different from 2 (b). The asymmetry results from phase shifting the modulation of one chain with respect to its neighbor (c). Finally, one diagonal of the incommensurate diffraction pattern in 3-21 can be obtained by phase shifting the modulation of each unit cell along the a direction. The overall phase shift increases with increasing a. Here the atomic positions are defined as (x,y) = (ma,nb).

respect to its neighbor by an amount ϕ. In figure 3-23c, $\phi = 0.3\pi$. The value of ϕ which best describes the data is $\phi = \pi/2$ corresponding to neighboring chains being perfectly out of phase with eachother. This ϕ also makes the most intuitive sense. Finally we need to make make incommensuration run along the diagonal, which from our soliton discussion we learned can be done by a shift of the solitons as a function of a. In our sinusoidal model, the corresponding parameter is a phase shift ξ of the modulation of each unit cell with respect to its neighbor. This results in a total phase shift of $n\xi$ of the n^{th} unit cell with respect to the first. Figure 3-23 shows the diffraction corresponding to a shift of $\xi = 0.45$.

The pattern in figure 3-21 has satellites running along both diagonals. We've only constructed one. The other can be obtained by changing the sign on xi, which corresponds to a domain twinning. Figure 3-24 shows the fully modelled modulation of the diffraction pattern in figure 3-21. The parameter values which best describe

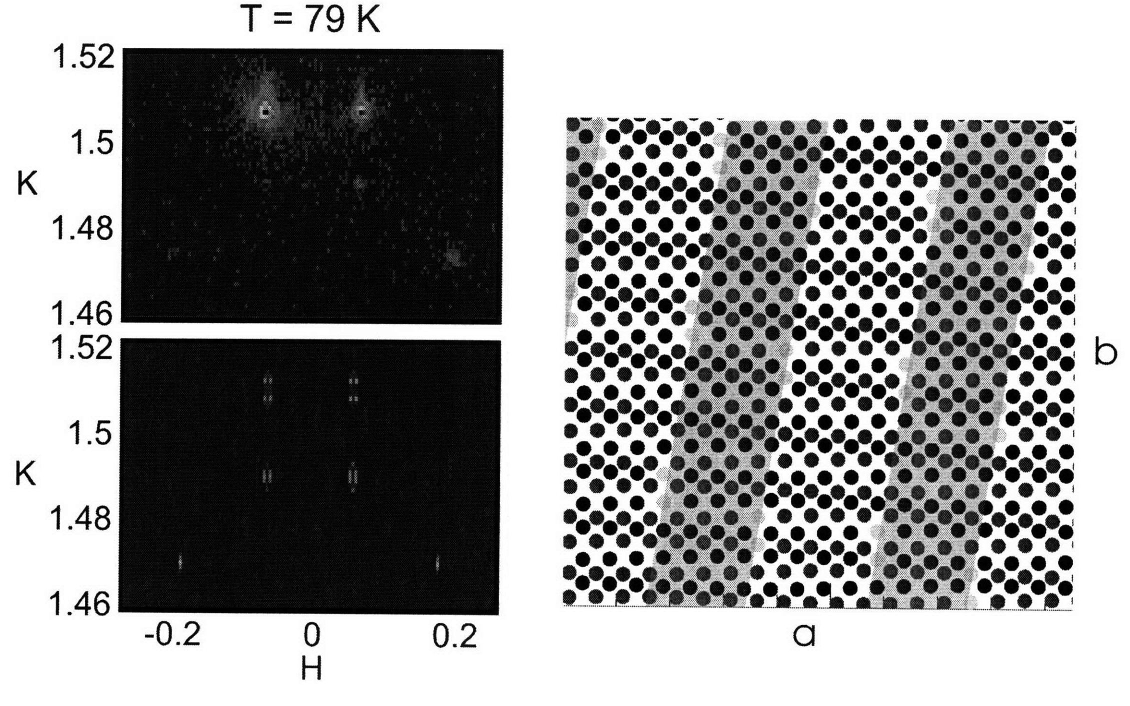

Figure 3-24: Fully modelled incommensurate diffraction along with a schematic of the atomic positions which generate the pattern. The solitons are highlighted in yellow, and the shading highlights the anti-phase domains which occur across the diagonal boundary. The atomic shifts have been exaggerated for illustration purposes. The parameters which give this pattern are discussed in the text.

the data are

$$\lambda = 2.041, \quad \phi = \frac{\pi}{2}, \quad \xi = 0.45 \tag{3.20}$$

and the twinning fraction of $+\xi/-\xi$ is 60/40. This model successfully reproduces both the peak pattern and the peak intensity asymmetry, of the first harmonics about the $K = 1.5$ axis, which we see from the table in figure 3-21 is about 1/100. However, we also see that the third harmonic intensity should be about the 1/200 times the strongest peak, but in our model it has an intensity $\sim 10^{-4}$ that of the strongest first harmonic. Recall from section 3.3.1, that the sinusoidal modulation has very weak third harmonics for small δ. It turns out that we can attain the correct intensity ratio by making δ unphysically large. Therefore we can expect to improve on this by changing the waveform. Since the square wave modulation has already been ruled out, the next viable possibility is the Jacobi elliptic function which was also discussed in section 3.3.1.

3.3.5 Harmonics

Now we have a good understanding of the basic structure of the incommensurate state. The final refinement to be made is to find the exact form of the modulation from the ratio I_3/I_1, following the procedure outlined in section 3.3.1. Figure 3-25a shows scans along H and K through the first and third incommensurate harmonics, along with corresponding scans through the commensurate peak at 10 K. The first harmonics are resolution limited, whereas the third harmonics show a clear broadening, implying a difference in characteristic lengths scales for each harmonic. This broadening from first to third harmonics was also observed by Christianson et. al. in the magnetic field induced incommensurate state in $CuGeO_3$[61]. While they could provide no quantitative treatment of the broadening, they did state that a finite width of the third harmonic requires a non-zero width of the first harmonic. Any broadening of the third harmonic is most likely due to imperfections in the crystal lattice. This broadening will effectively increase $I3/I1$, so corrections must be made assuming the harmonic should be resolution limited. By summing over all third harmonics then dividing this by the sum over all first harmonics in 3-25, we get a ratio $I_3/I_1 = 1/110$.

In section 3.3.1, we saw that I_3/I_1 was ~ 0.1 for a square wave, which is not consistent with our I_3/I_1 ratio. The next easy guess is a sinusoidal modulation, which from equation 3.15 should be $\sim (Q\delta)^4/576$, for distortion amplitude δ. In section 3.3.2 we found the commensurate atomic displacement to be about 3%. The sum of the integrated intensities of all six incommensurate peaks plus third harmonics is about ten times less than the integrated intensity of the commensurate peak, so ϵ is roughly $.003b$. Using this for $Q = 1.5$, we find an expected sinusoidal I_3/I_1 of $\sim 10^{-10}$, which differs significantly from the measured value 1/110. Since the measured ratio was only a factor of 10 different from that for a square wave, (compared to 10^-8 for the sine wave), it is reasonable to assume that the modulation is a smeared square wave. We therefore turn to the soliton. Recall from section 3.3.1 that the soliton function $u(la/\Gamma k, k)$ depends on both $x_i \equiv la$ and the parameter, k, which from 3-15 we saw defines the soliton width Γ. The value of k can be determined from I_3/I_1 measured for one value of the incommensurate wavevector δq using equation 3.17. This value of k can then be used in equation 3.12: $\frac{\pi}{\delta q} = 2kK(k)\Gamma$ to determine the soliton width. As δq changes with temperature, k will change which effectively changes the soliton spacing. Therefore, once Γ is known, the δq dependence of k, and thus the I_3/I_1 ratio is determined. For TiOCl, we determined $k = 0.97$ at $q = 0.11$, which corresponds to $\Gamma \sim 8$Å. For a nearest neighbor Heisenberg model, Nakano and Fukuyama predict [5].

$$\Gamma = \frac{\pi J b}{2\Delta_o}, \tag{3.21}$$

where J is the intra-chain coupling and Δ_o is the excitation gap. Using $J = 660K$ from Seidel et al. [4], and $\Delta_o = 430K$ from Imai [62], the theoretical soliton length for TiOCl is $\Gamma = 8.1$Å, which is in very good agreement with the measured value. The soliton spacing $\pi a/0.11 = 108$Åis much larger than the soliton width, so the solitons are widely spaced, and the modulation resembles a smeared square wave, as we guessed by comparison of I_3/I_1 with that of the square wave. Once Γ is determined the entire $I_3/I_1(\delta q)$ can be calculated. This calculation along with the measured I_3/I_1

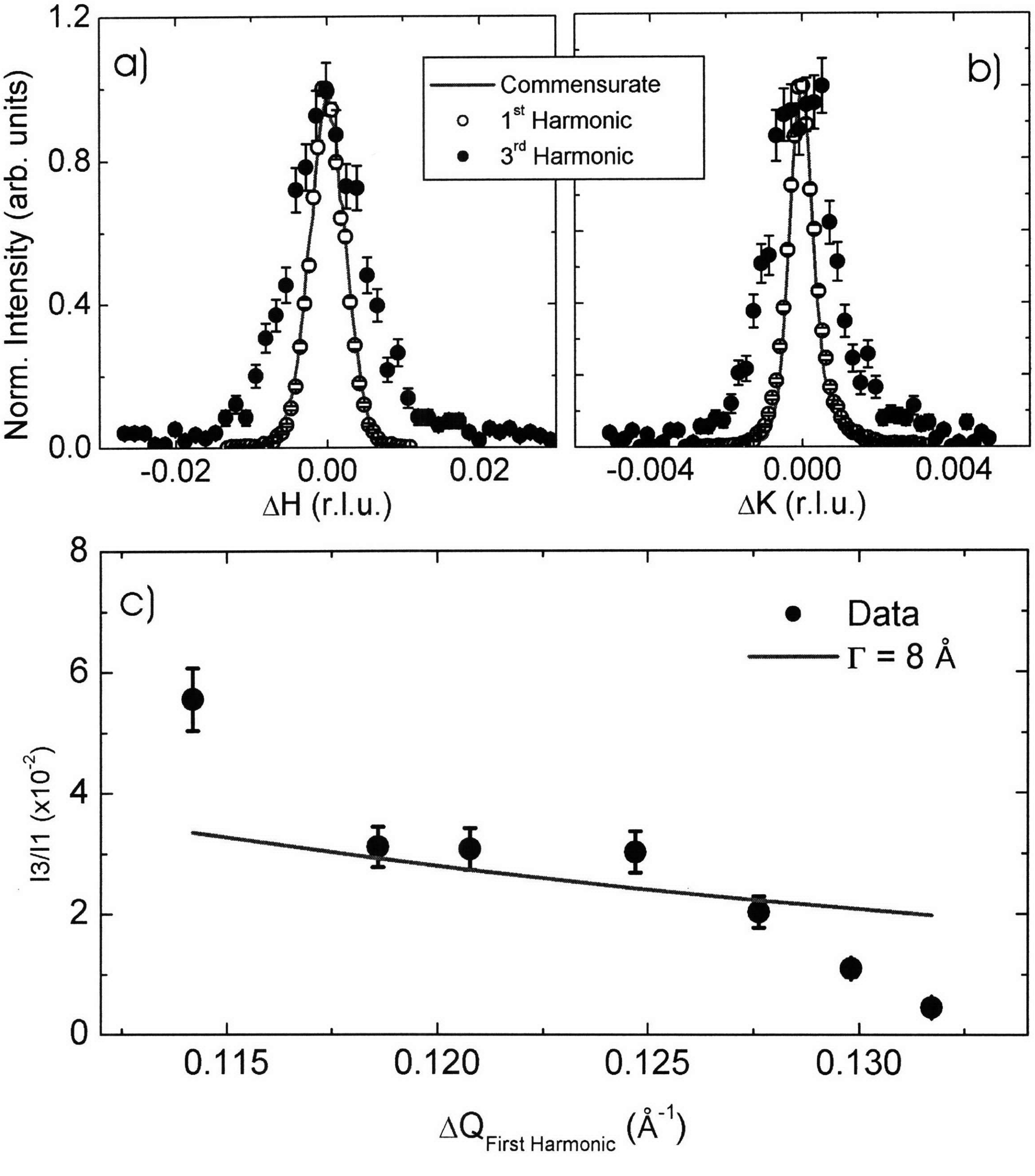

Figure 3-25: Comparison of the commensurate peak with first and third incommensurate harmonics (figures a,b), and (figure c) the ratio I3/I1 as a function of the incommensuration, ΔQ, with a fit line to the expected behavior for a soliton with width $\Gamma = 8$Å.

ratios are shown in in figure 3-25b.

We now have valuable insight into the nature of the incommensurate state, and can therefore make some predictions as to its origin. It appears that at T_{c_2}=92 K, the spin interactions want to make the lattice dimerize. If the atoms formed a perfect rectangular lattice, then the only competition is between the spin energy and the

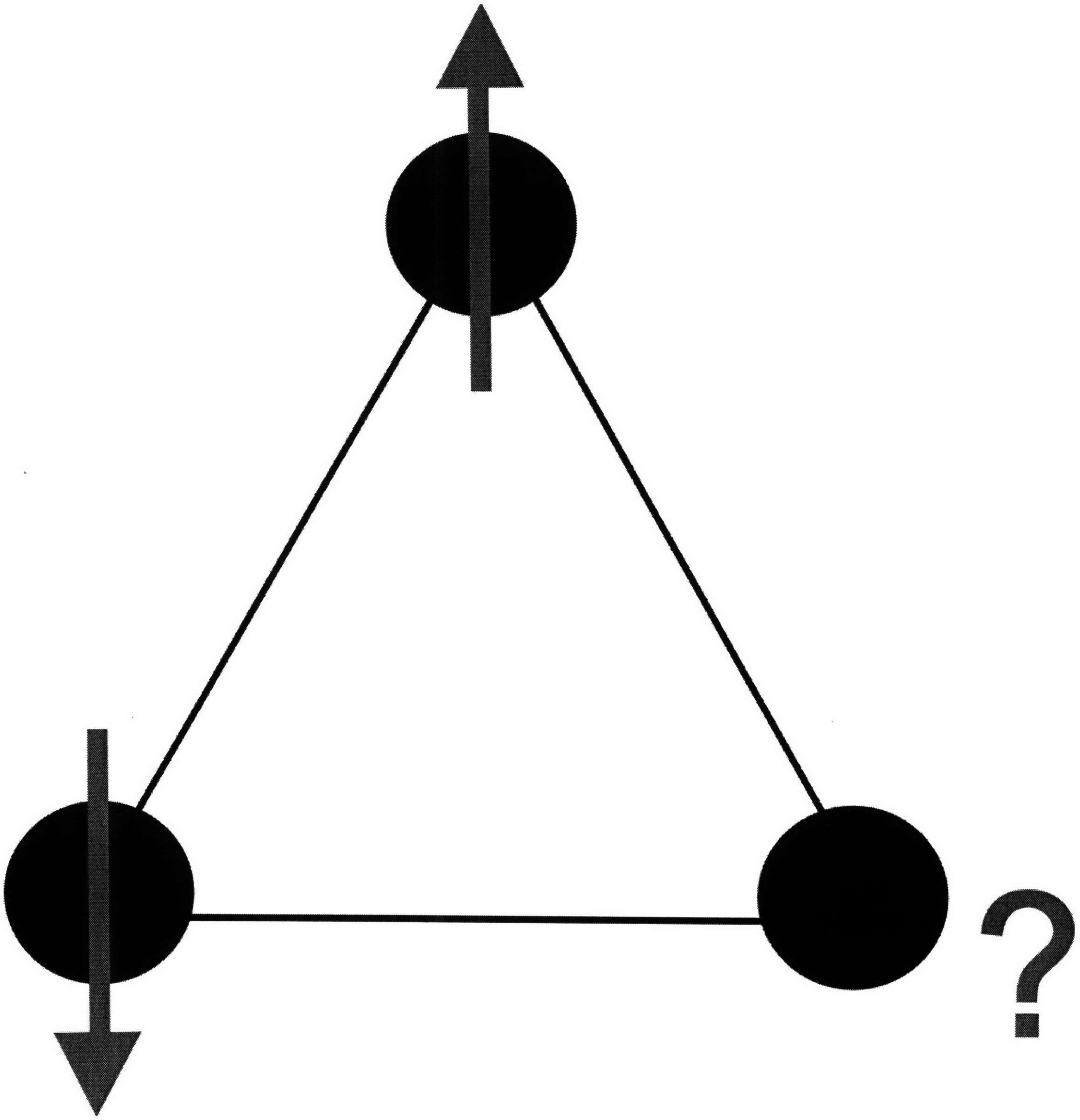

Figure 3-26: Cartoon illustrating that a simple rectangular lattice has no problem dimerizing, whereas a staggered lattice, like TiOCl, cannot satisfy equal atomic spacing for every atom for a given dimer length. This gives rise to a frustration of the lattice energy.

lattice energy along the chain (recall equation 1.11). However, in TiOCl neighboring chains are shifted by a $b/2$ with respect to eachother, therefore the lattice energy of the neighboring chains will also be a competing factor. The lattice energy along the chain is still the dominant energy, since it corresponds to nearest neighbor Ti-Ti pairs, but at high enough temperatures the next nearest neighbor lattice energy will frustrate the dimerization (see figure 3-26). The lattice relieves this frustration by inserting periodic defects, or solitons. From the Jacobi elliptic function model of the solitons, we can see that at 92 K, when the incommensurate peaks first appear, the solitons are spaced closely together, and the modulation is nearly sinusoidal. This is the temperature where the next nearest neighbor lattice energy has its strongest influence. As the temperature is decreased the soliton spacing increases gradually (as given by the inverse of the incommensurate wavevectors). This is reflected in the q-dependence of I_3/I_1 compared to the expected soliton behavior in figure 3-25. The solitons are separated by regions of nearly perfect dimerized lattice. The first order phase transition can be understood in terms of the domains (delineated by shading in figure 3-24) which are dimerized out of phase with respect to eachother. In order for the lattice to become fully dimerized, the sign of the dimerization has to change in half of the domains, corresponding to an instantaneous change in entropy, consistent with a first order transition. Buried in the middle of this understanding is the implication that the lattice dimerizes wants to dimerize at 92 K, meaning T_{SP} is actually at T_{c_2}, rather than T_{c_1}. So we can now label T_{c_2}=92 K as the transition into an incommensurate spin-Peierls state, and T_{c_1}=65 K as the incommensurate to commensurate transition temperature. So far we have been labelling this as a spin-Peierls transition, but in the next section, we will examine the phonon dynamics above the transition temperature to see if there is any evidence of spin-phonon coupling leading up to T_{c_2}.

3.4 Inelastic X-ray Study of the Lattice Dynamics

Our understanding of the incommensurate modulation of the Ti atoms has illuminated some possible interactions present in the dimerized state. To further elucidate the nature of the phase transition at T_{c_2}, we can raise the temperature above the transition and investigate the lattice dynamics leading up to the distortion. In section 3.4.3 we will see that the typical scenario for a structural phase transition is the softening of a zone boundary phonon having a vibrational pattern resembling the static distortion. As the transition temperature is approached, the mode vibrates slower and slower until at the critical temperature, it becomes frozen into the low temperature distortion.

3.4.1 Basic Concepts of Lattice Vibrations

A Coupled Harmonic Oscillator

In the simplest approximation, atoms in a lattice can be modelled as being held together by a series of interconnected springs. Therefore, characterizing lattice vibrations reduces to finding the interatomic "spring constants". A simple model to understand how this can be done is the coupled harmonic oscillator shown in figure 3-27a. Two masses are connected to each other by a spring, then each mass is connected to a wall by additional springs. For simplicity we will assume all both masses have mass, m, and the springs labelled $i = 1, 2, 3$ have spring constant k_i. We will only consider the 1D problem, meaning the masses are confined to move only along the x-direction, as indicated in the diagram. If we balance the forces using Newton's law

$$F_1 = m_1\ddot{x}_1 + k_1 x_1 - k_2(x2 - x1) \tag{3.22}$$

$$F_2 = m_2\ddot{x}_2 + k_3 x_2 + k_2(x2 - x1), \tag{3.23}$$

which we can write in matrix form:

$$\begin{pmatrix} m_1\ddot{x}_1 \\ m_2\ddot{x}_2 \end{pmatrix} = -\begin{pmatrix} k_1 + k_2 & -k_2 \\ k_3 & k_2 + k_3 \end{pmatrix} \begin{pmatrix} x_1 \\ x_2 \end{pmatrix}, \tag{3.24}$$

which can be written

$$M\ddot{\vec{X}} = K\vec{X} \tag{3.25}$$

If we compare equation 3.27 with the analogous expression for a single mass on a spring

$$m\ddot{x} = kx, \tag{3.26}$$

we see that the matrix, K, contains the force constant information about the system. If we assume harmonic solutions $x_i = e^{i\omega t}$, then equation 3.27 becomes

$$-\begin{pmatrix} m_1\omega^2 x_1 \\ m_2\omega^2 x_2 \end{pmatrix} = -\begin{pmatrix} k_1 + k_2 & -k_2 \\ -k_3 & k_2 + k_3 \end{pmatrix} \begin{pmatrix} x_1 \\ x_2 \end{pmatrix}. \tag{3.27}$$

Bringing all terms together and dividing by the mass,

$$\begin{pmatrix} \frac{k_1+k_2}{m_1} - \omega^2 & -\frac{k_2}{m_1} \\ \frac{k_3}{m_2} & \frac{k_2+k_3}{m_2} - \omega^2 \end{pmatrix} \begin{pmatrix} x_1 \\ x_2 \end{pmatrix} = 0, \tag{3.28}$$

From this we see that the frequency is the eigenvalue of the force constant matrix. Therefore, we need to take the determinant of the find the energy eigenvalues. For simplicity, let's consider that all spring constants are k and both masses are m, then equation 3.28 becomes

$$\begin{pmatrix} \frac{2k}{m} - \omega^2 & -\frac{k}{m} \\ \frac{k}{m} & \frac{2k}{m} - \omega^2 \end{pmatrix} \begin{pmatrix} x_1 \\ x_2 \end{pmatrix} = 0,$$

Which after taking the determinant, we find that

$$\omega = \sqrt{\frac{2k}{m} \pm \frac{k}{m}} \tag{3.29}$$

The associated eigenvectors are:

$$\omega_0 = \sqrt{\frac{k}{m}} \begin{pmatrix} 1 \\ 1 \end{pmatrix}; \quad \omega_0 = \sqrt{\frac{3k}{m}}, \begin{pmatrix} 1 \\ -1 \end{pmatrix}. \tag{3.30}$$

Figures 3-27b),c) show the vibrations associated with the eigenvectors in 3.30. In this example, only modes confined along x have been considered, or the so called "longitudinal" modes. We could have just as easily followed the same procedure for

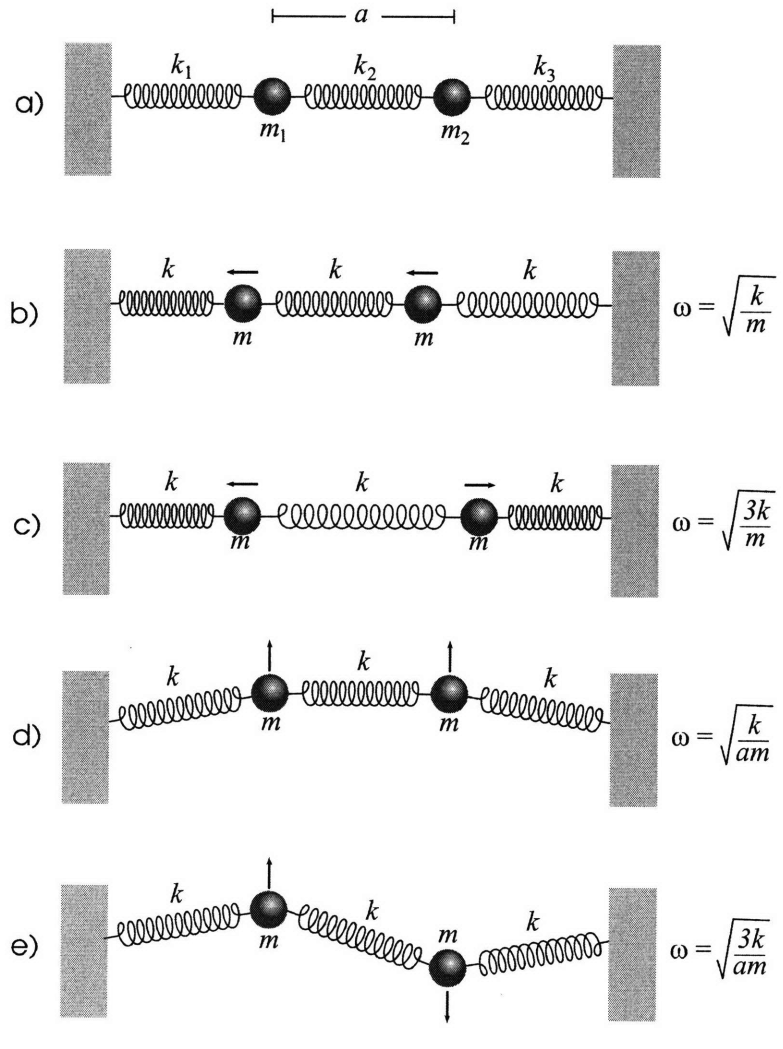

Figure 3-27: a) Example of a coupled harmonic oscillator: mass 1, is connected to a wall by spring 1, and to mass 2 by spring 2. Mass 2 is connected to a wall by spring 3, and to mass 1 by spring 2. The masses of are m_1 and m_2 respectively. In b)-e), the masses and spring constants have been set to be equal. Figures b),c) show the longitudinal normal modes, and d),e) show the transverse normal modes.

a displacement along y or z, or "transverse" modes. However, since the atom in a transverse mode is displaced perpendicular to the chain direction, a displacement y will only stretch the spring out by an amount $ay/\sqrt{y^2+a^2}$ which for $y << a$ is y/a. So if we scale the spring constant k by a giving $k_\perp = k_{||}/a$, then the derivation is identical to that of the longitudinal modes. The transverse frequencies and eigenvectors are

$$\omega_\perp = \sqrt{\frac{k}{am}}, \begin{pmatrix} 1 \\ 1 \end{pmatrix}; \quad \omega_\perp = \sqrt{\frac{3k}{am}}, \begin{pmatrix} 1 \\ -1 \end{pmatrix} \tag{3.31}$$

Since the system is isotropic about the chain axis, the two orthogonal transverse normal modes will have the same energy. It turns out that these are the only normal modes for the system. There are two atoms with three vibrational directions, for a total of 6 normal modes. In a sense we "cheated" by guessing the good directions, but any arbitrary displacement $\vec{u}$ can be broken down into $u_{||} + u\perp$, then we see that the components can be derived independently, as we have just done.

Linear Chain Model

If we now consider that m$_1$ and m$_2$ are neighboring masses in a periodic chain with indices m$_1$ = m$_i$, m$_2$=m$_{i\pm1}$, and displacements u^μ, then for nearest neighbor interaction, equation 3.22 generalizes to

$$m_i\ddot{u}_i^\mu = -\, k_1(u_i^\mu - u_{i-1}^\mu) - k_2(u_i^\mu - u_{i+1}^\mu) \tag{3.32}$$

$$= -\, (k_1 + k_2)u_i^\mu + k_1 u_{i-1}^\mu + k_2 u_{i+1}^\mu \tag{3.33}$$

$$m_{i+1}\ddot{u}_{i+1}^\mu = -\, k_2(u_{i+1}^\mu - u_i^\mu) - k_1(u_{i+1}^\mu - u_{i+2}^\mu) \tag{3.34}$$

$$= -\, (k_1 + k_2)u_{i+1}^\mu + k_2 u_i^\mu + k_1 u_{i+2}^\mu \tag{3.35}$$

Unlike the coupled oscillator problem, solutions to equation 3.32 will have the form $u^\mu(x_i) = \xi_i e^{i(qx_i - \omega t)}$, which is the equation for a wave having deformation ξ_i travelling with wave vector q and frequency ω. For a periodic chain with atomic spacing a,

$x_i = na$, therefore substituting $u_i^\mu(x_i)$ into equation 3.32 gives

$$-m_i\xi_i\omega^2 = -\xi_i(k_1+k_2) + (k_1e^{-i2qa}+k_2)\xi_{i+1} \tag{3.36}$$

$$-m_{i+1}\xi_{i+1}\omega^2 = (k_2+k_1e^{i2qa})\xi_i - (k_1+k_2)\xi_{i+1}e^{iqa}. \tag{3.37}$$

where the common factors $e^{i\omega t}$ have been divided out, and the periodicity, $m_{i+2} = m_i$ results in $\xi_{i\pm 2} = \xi_i e^{\pm i2qa}$. As before, we can write this in matrix form. For simplicity, we can denote the two non-equivalent sites $i, i+1$ with $1, 2$.

$$\omega^2 \begin{pmatrix} m_1\xi_1 \\ m_2\xi_2 \end{pmatrix} = \begin{pmatrix} k_1+k_2 & -(k_1e^{-i2qa}+k_2) \\ -(k_1e^{i2qa}+k_2) & k_1+k_2 \end{pmatrix} \begin{pmatrix} \xi_1 \\ \xi_2 \end{pmatrix} \tag{3.38}$$

Again, if we let both masses be m and both spring constants be k, then both equations in 3.36 simplify to the following energy equation

$$\omega = 2\sqrt{\frac{k}{m}}\left|\sin\left(\frac{qa}{2}\right)\right|. \tag{3.39}$$

The energy is now a function of q, which disperses linearly at $q = 0$, with the slope gradually decreasing as $q \longrightarrow \pi$. This is quite intuitively understood if we think of q in terms of the wavelength $\lambda = 2a\pi/q$. So $q = 0$ corresponds to a $\lambda = \infty$, which is essentially a uniform translation of the entire block of material. For very long wavelengths, it isn't surprising that the energy required to change λ by $\delta\lambda$ is just proportional to $\delta\lambda$. At $q = \pi$, $\lambda = 2a$, which is corresponds to a 2 atom wavelength. There can be no shorter wavelength excitation than this, therefore it requires more energy to change the wavelength by the same amount $d\lambda$, if $\lambda = 2a - \delta\lambda$. Modes which disperse linearly at $q = 0$ are known as acoustic modes. If instead we consider the more general solution of equation 3.38, where either the masses or spring constants aren't equal (both are equivalent since $\omega \propto \sqrt{k/m}$), then we find for the eigenvalues (after a little algebra)[41]:

$$\omega^2 = k_1 + k_2 \pm \sqrt{k_1^2 + k_2^2 + 2k_1k_2\cos 2qa} \tag{3.40}$$

There are now two energy eigenvalues. This is a fundamental property of normal modes. For N atoms with d degrees of freedom, there will be dN normal modes. In this case, the motion is constrained along one direction, so $d = 1$, and there are 2N atoms, meaning there should be 2N normal modes. However, recall that for every M unitcells, there are M q-points, therefore, at each q, we expect N/M=2 (M=N/2) branches. So the number of atoms in the unitcell determine the number of branches,

The plots of the two calculated phonon branches as a function of q are shown in figure 3-28c. One of the dispersion curves resembles the acoustic mode for the monatomic chain in figure 3-28b, but the other does not disperse to zero at $q = 0$,

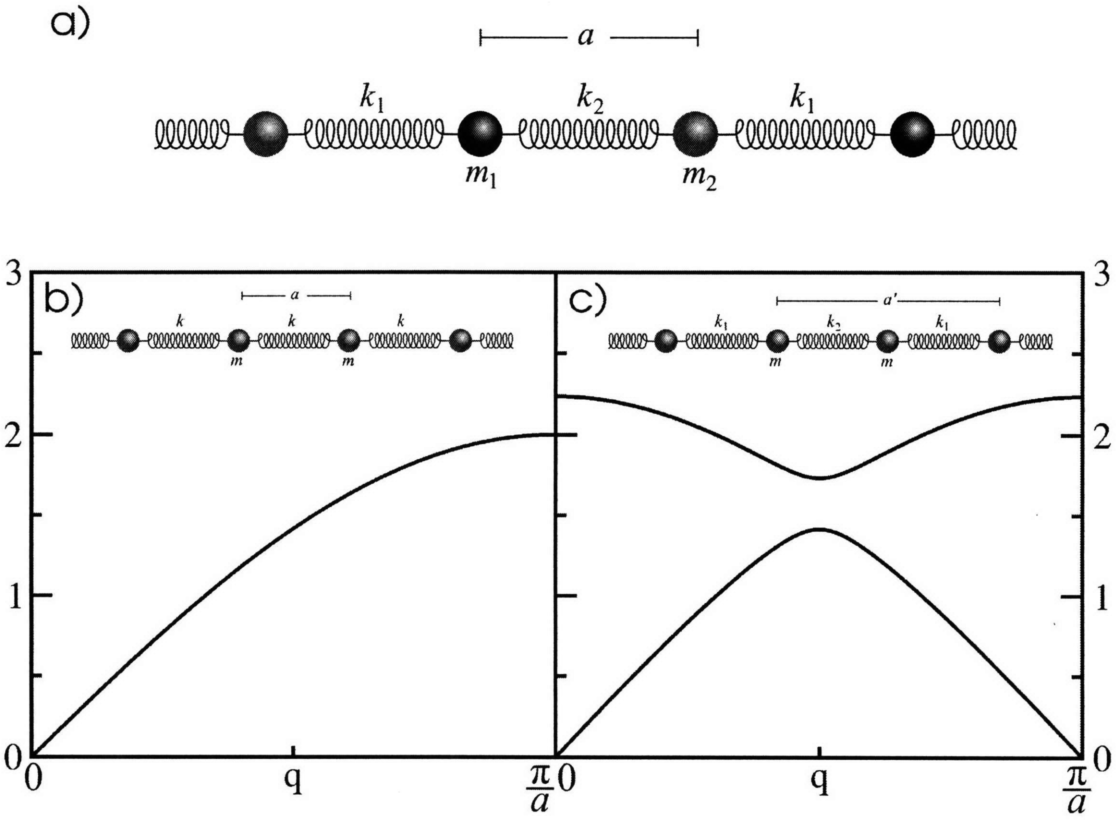

Figure 3-28: a) Example in figure 3-27 extended to a linear chain of N atoms. b) Energy dispersion for equal masses and spring constants. This "acoustic" dispersion is characterized by a linear slope at $q = 0$. c) Energy dispersion curves from equation 3.40, with $k_2 = 1.5k_1$. There are now two branches, one acoustic and one which does not disperse to $\omega = 0$ for $q = 0$. This upper mode is known as the "optical" mode. Notice that the periodicity of the dispersion has changed by a factor of 2, due to the doubling of the periodic unit on the chain (as indicated by a').

rather it levels off at some finite value. While we do not show it here, the eigenvector ξ_i for this mode indicates that the atoms are vibrating against each other, much like the zone boundary acoustic mode for the monatomic case. We also see that the period of the dispersion is half that for the monatomic chain. This is because we used the interatomic spacing as a reference distance, where the minimum periodic unit is actually $a' = 2a$, as indicated in the cartoon of figure 3-28c. This doubling of the unit cell, results in half the periodicity in reciprocal space.

Phonons in Higher Dimensions

Returning to the general coupled oscillator in Figure 1a, we can write down the total potential energy of the system

$$U = \frac{1}{2}k_1x_1^2 + \frac{1}{2}k_2(x_2 - x_1)^2 + \frac{1}{2}k_3x_2^2. \tag{3.41}$$

If we differentiate once with respect to each variable

$$\frac{\partial U}{\partial x_1} = k_1x_1 - k_2(x_2 - x_1) \tag{3.42}$$
$$\frac{\partial U}{\partial x_2} = k_3x_2 + k_2(x_2 - x_1) \tag{3.43}$$
$$\tag{3.44}$$

we recover the two force equations 3.22. If we differentiate again

$$\frac{\partial^2 U}{\partial x_1^2} = (k_1 + k_2) \quad \frac{\partial^2 U}{\partial x_2 \partial x_1} = -k_2 \tag{3.45}$$
$$\frac{\partial^2 U}{\partial x_2^2} = (k_2 + k_3) \quad \frac{\partial^2 U}{\partial x_2 \partial x_1} = -k_3 \tag{3.46}$$
$$\tag{3.47}$$

only the force constants remain, and they are identical to the matrix elements in equation 3.27. This leads to a more general formulation of equation 3.27

$$\begin{pmatrix} m_1\ddot{x}_1 \\ m_2\ddot{x}_2 \end{pmatrix} = - \begin{pmatrix} \frac{\partial^2 U}{\partial x_1^2} & \frac{\partial^2 U}{\partial x_2 x_1} \\ \frac{\partial^2 U}{\partial x_1 x_2} & \frac{\partial^2 U}{\partial x_2^2} \end{pmatrix} \begin{pmatrix} x_1 \\ x_2 \end{pmatrix} = D^{xx}_{x_1,x_2} \begin{pmatrix} x_1 \\ x_2 \end{pmatrix}, \tag{3.48}$$

where $D^{xx}_{x_1,x_2}(x)$ is the force constant matrix. It may seem that we made simple expression, like 3.27, more complicated. However, If we compare equation 3.27 with equation 3.38, then we see that this method for calculating the force constants will carry over into the chain of atoms. In fact, even into three dimensions this the force constant matrix $D^{\alpha\beta}_{\mu\nu}(\vec{R})$ is generally applicable to calculate the force constant due due to displacing atoms μ and ν along directions α and β respectively. It turns out that the 3D analog to equation 3.32 using $D^{\alpha\beta}_{\mu\nu}(\vec{R})$ is[63][64]

$$M_\mu \ddot{\vec{u}}(\vec{R}) = \sum_{\alpha\beta\mu\nu} D^{\alpha\beta}_{\mu\nu}(\vec{R})(u^\alpha_\mu - u^\beta_\nu) \tag{3.49}$$

Equation 3.49 is solved in much the manner as equation 3.32, by assuming wave solutions

$$\mathbf{u}(\vec{R},t) = \frac{1}{\sqrt{M_\mu}} \xi_s(\vec{k}) e^{i(\vec{q}\cdot\vec{R}-\omega t)}, \tag{3.50}$$

where $\xi^i_s(\vec{k})$ is now tensor indicating the displacement of all of the atoms in mode s at wave-vector k. Not surprisingly, there is no closed form analytical solution, but in principle, this solutions to this differential equation will be of the form[41]

$$\omega^2 \xi_s = \tilde{D}^{\alpha\beta}_{\mu\nu}(\vec{q})\xi_s$$

where

$$\tilde{D}^{\alpha\beta}_{\mu\nu}(\vec{q}) = \frac{\partial^2 U}{\partial u^{*\alpha}_\mu(\vec{q}) \partial u^\beta_\nu(\vec{q})} \tag{3.51}$$

is known as the *dynamical matrix*[65]. Using the dynamical matrix, the expression for the phonon eigenvalues $\omega(\vec{q})$ is

$$det \left| \frac{1}{\sqrt{M_i M_j}} \tilde{D}^{\alpha\beta}_{\mu\nu}(\vec{q}) - \omega^2(\vec{q}) \right| = 0. \tag{3.52}$$

3.4.2 Lattice Dynamical Calculations in the Harmonic Approximation

As mentioned, it is not generally possible to calculate the dynamical matrix for most real crystalline systems analytically. However, calculation of the dynamical and/or force constant matrices lend themselves to numerical techniques, especially with the advancement of computer technologies in recent decades.

Shell Model

The start of any dynamical matrix calculation is a means to calculate the total energy of a system of atoms brought together into a lattice. One of the simpler energy calculation schemes is the so-called shell model. The shell model treats each atom as a positively charged core attached to a negatively charged shell by a spring with constant k_{cs}. To model the interatomic forces, an empirical potential model is used, which is then optimized to fit the system at hand. While there are dozens of implementations of this technique, the one used in this work was the General Utility Lattice Program (GULP), available free of charge for academic use from [66].

Two common potentials used for short-range interactions are the Lennard-Jones and Buckingham potentials [67]. Both potentials are plotted in figure 3-29. The Buckingham force tends to be more widely applicable to real systems, and it is more justifiable theoretically due to the exponential decay of short-range interactions[67]. However, it becomes non-physical $V(r) \rightarrow \infty$ for $r \rightarrow 0$. Values of A, ρ, and C are tabulated for numerous atomic pairs[1], which can then be used either as is, or as the starting point for a potential optimization in a shell model calculation. The

---

[1] See for example reference [68].

Lennard-Jones potential is also widespread due to its ease of use in computation[69]. As mentioned earlier, these are only two commonly used potentials. In general, any potential model can be used as long as it is appropriate to the system.

Once a suitable set of potentials is found, they must be optimized and tested. In GULP, it is possible to perform a least squared type of fitting of the potential parameters for the various atomic pairs placed in a unit cell. Once the parameters have been optimized, it is necessary to test the quality of the cell potential by calculating the equilibrium structure (relaxing the cell). This is also done through a steepest descent approach. Usually the high symmetry positions are held fixed, and everything else is adjusted to minimized the forces. Once the forces have been minimized, then it is possible to use this energy model to calculated the phonon modes. Since the models being used in this case are real space models, the force constants can be calculated directly using 3.49. As we have seen in the previous section, the phonon modes are just the eigenvalues of the force constant matrix.

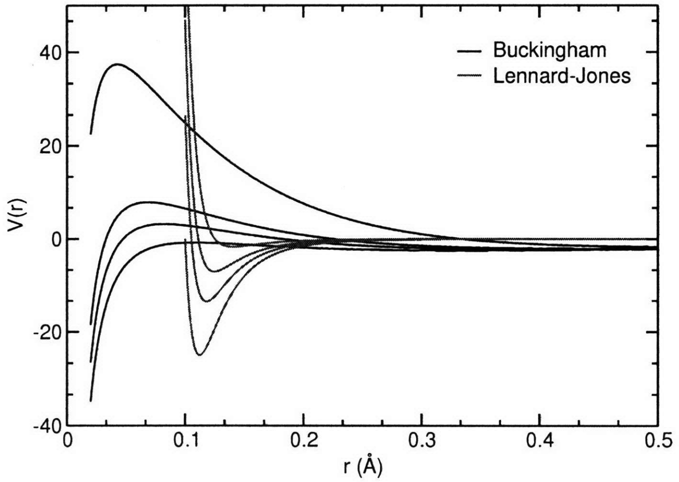

Figure 3-29: Buckingham $V(r) = Ae^{\frac{r}{\rho}} - \frac{C}{r^6}$, and Lennard-Jones (6-12): $V(r) = \frac{A}{r^6} - \frac{B}{r^12}$. The various curves show different ratios of A/C ($\rho = 0.1$) for Buckingham, and A/B for Lennard-Jones. As each of these ratios increases, the potential becomes more repulsive.

Density Functional Theory and Linear Response Perturbation Theory

In section 3.4.2, we saw that it was possible to calculate the phonons based on the second derivatives of an empirically determined potential model of the lattice. This can be very useful to reproduce experimentally observed dispersion curves, and even estimate some material properties (like elastic constants), but one must alway question the validity of these results since they are in essence based on a fictitious model of the lattice. The ideal model would be to take the exact atomic potentials, calculate how these potentials change upon placing them in a periodic lattice with other atomic potentials, then from this calculate the phonons. While this solution isn't yet a possibility with current computing capacities, a few concepts from solid state theory greatly aid in reducing computation time.

The first simplification allows for the use of the orthogonal plane wave (OPW) basis set, which is convenient for computation. For metals this basis set works fine as is, but for systems with tightly bound electrons, the high plane-wave cut-off energy would make computation cumbersome. However, if we realize that the bonding is mostly between valence electrons, then a potential which includes detailed information

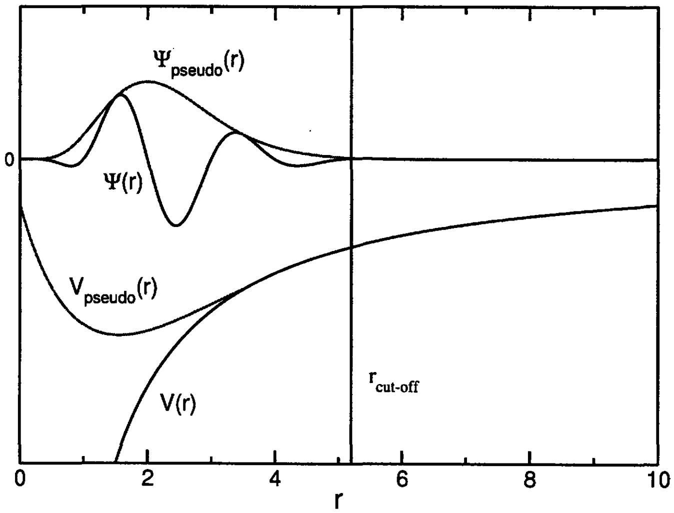

Figure 3-30: The Pseudopotential approximates the high energy, quickly oscillating core wavefunction with a slowly varying wavefunction, which is orthogonal to the core states, resulting in a weak enough potential to allow calculation using nearly free electron states. The cut-off radius, is a distance above which the pseudopotential and real potential match.

about the rapidly oscillating core wavefunctions is unnecessary so it is possible to replace these with a weaker potential, which is sufficient to provide the net potential influence of the core, yet weak enough to allow a nearly free electron calculation with reasonable cut-off energies[41].

Now that we have justified the use of pseudopotentials, we need to know how to calculated the ground state. This turns out to be non-trivial, but a recent theory, known as Density Functional Theory has made the numerical calculation of ground state energies from input pseudopotentials a reality. It is well beyond the scope of this work to discuss the details of Density functional theory. The theory is based on a theorem which states that the ground state charge density is unique, in the sense that two different potentials cannot yield the same ground state charge density. Essentially it is a variational technique, which minimizes the energy by finding the electron density corresponding to the potential V(r)[65]. The advantage of this is that the charge density is given by only 3 variables, in contrast to the $3N_{electrons}$ variables required to characterize the wavefunction. For our purpose of this work, it is a tool used by a piece of software used to extract the energy from the input pseudopotentials. The interested reader is directed to the works of Hohenberg and Kohn[70],Parr and Yang[71], and Dreizler and Gross [72] for the theoretical details.

In this work density functional theory was used to numerically calculate the phonon eigenvalues and eigenvectors. The code used was the open source Plane Wave Self Consistent Field (PWSCF), part of the Quantum Espresso package, available on-line at [73]. While there are numerous techniques to calculate phonons once a total energy calculation is available [64][63], PWSCF calculates the dynamical matrix $\tilde{D}^{\alpha\beta}_{\mu\nu}(\vec{q})$ over a suitable q-point grid in reciprocal space. From that point it is possible to Fourier transform $\tilde{D}^{\alpha\beta}_{\mu\nu}(\vec{q})$ to get the force constant matrix $\tilde{D}^{\alpha\beta}_{\mu\nu}(\vec{R})$, which can then be used to calculate the phonons at any arbitrary q-vector. The method utilized by PWSCF to calculate the dynamical matrix is known as Density Functional Perturbation Theory. The main idea is to solve the equation[65]

$$\frac{\partial^2 E(\mathbf{R})}{\partial \mathbf{R}_I \mathbf{R}_J} = \int \frac{\partial n_{\mathbf{R}}(\mathbf{r})}{\partial \mathbf{R}_J} \frac{\partial V_{\mathbf{R}}(\mathbf{r})}{\partial \mathbf{R}_I} dr + \int n_{\mathbf{R}}(\mathbf{r}) \frac{\partial^2 V_{\mathbf{R}}(\mathbf{r})}{\partial \mathbf{R}_I \partial \mathbf{R}_J} dr + \frac{\partial^2 E_N(\mathbf{R})}{\partial \mathbf{R}_I \partial \mathbf{R}_J}, \tag{3.53}$$

where $\mathbf{R}_J$ are nuclear coordinates, $V_{\mathbf{R}}(\mathbf{r})$ is the electron-nucleus interaction $n_{\mathbf{R}}(\mathbf{r})$ is the electron charge density, and $E_N(\mathbf{R})$ is the energy of the nuclear configuration. Equation 3.53 results from a combination of the Hellmann Feyman theorem with the Born-Oppenheimer Hamiltonian[65]. The important features of this result are that first of all, the force constant calculation requires calculating the electron charge density $n(\mathbf{R})$, as well as the first derivative of $n(\mathbf{R})$ with respect to changes in the nuclear configuration. This first derivative is the linear response from which the technique gets its name. Equation 3.53 is solved in the scope of DFT, the details of which will not be discussed. The interested reader is directed to a nice Review of Modern Physics article by Baroni *et. al.*[65] as well as reference [74].

In section 3.4.5 we will see an example of a shell model calculation applied to TiOCl, which is then compared to measured phonon dispersion curves. Then chapter () will explore DFPT in an attempt to improve upon the shell model calculated dispersion curves. That discussion will include examples and details about running PWSCF.

3.4.3 Structural Phase Transitions

The Damped Harmonic Oscillator Response Function

An inelastic x-ray experiment measures directly the dynamical structure factor, $S(Q,\omega)$, which, from the fluctuation-dissipation theorem, is given by

$$S(Q,\omega) = [n(\omega) + 1]\ \chi''(Q,\omega). \tag{3.54}$$

In general $\chi''(Q,\omega)$ quantifies the linear response of a system to an external perturbation. In the case of x-ray scattering from a lattice of atoms, this perturbation is the oscillating field of an incident photon, triggering an oscillatory response from the atomic lattice. The frequency and direction of each atomic oscillation is dependent on the curvature of the potential surface in the vicinity of the atom. From a detailed lattice vibration study, it is therefore possible to infer the the forces acting on the atoms in a lattice.

The exact calculation of the change in potential due to the displacement from equilibrium of a single atom is overwhelming, so to simplify, the lattice potential can be expanded in terms of the atomic displacements. Since at equilibrium, the linear term must be zero, the lowest order approximation is the quadratic term, leaving

$$U_{\alpha,\beta} \approx U_0 + \sum_{\alpha,\beta,\mu,\nu} \frac{d^2U}{du^\nu_\alpha du^\mu_\beta}(\vec{u}^\mu_\alpha - \vec{u}^\nu_\beta)^2 + O(\vec{u}^\mu_\alpha - \vec{u}^\nu_\beta)^3, \tag{3.55}$$

where μ, ν label atoms, and α, β are Cartesian coordinates. The starting point for modelling lattice dynamics is to neglect terms higher than 2nd order in $(\vec{u}^\mu_\alpha - \vec{u}^\nu_\beta)$. This is known as the harmonic approximation. In this approximation, the atomic response to an incident phonon with frequency ω is simply a damped harmonic oscillator given by

$$\chi'' = \frac{A(\Gamma\omega)}{(\omega^2 - \omega_0^2)^2 + \Gamma^2\omega^2}, \tag{3.56}$$

where Γ is the damping constant, and ω_o is the harmonic frequency. Plots of equation 3.56 for different relative values of Γ, ω_0 are shown in figure 3-31. For the case of small damping (figure 3-31a), i.e. $\Gamma << \omega_0$, equation 3.56 is sharply peaked with a FWHM, Γ, centered on $\pm\omega_0$. For strong damping, the peak is no longer at ω_0. The position of the peak is ω_1, defined by

$$\omega_1^2 = \omega_0^2 - \frac{\Gamma^2}{4} \tag{3.57}$$

which is shifted down from ω_0 as in figure 3-31b. Equation 3.57 only has a real solution for $\Gamma < 2\omega_0$. In the so-called over-damped region where $\Gamma > 2\omega_0$, ω_1 is purely imaginary, and χ'' is peaked at $\omega = 0$ (figure 3-31c). Of course what is measured is $S(Q, \omega)$, which according to equation 3.54 is related to $\chi''(Q, \omega)$ the Bose factor $n(\omega) + 1$. Since both $\chi''(Q, \omega)$ and $n(\omega) + 1$ are odd, the product, $S(Q, \omega)$, is even, with different weighting on the positive and negative energy sides to take into account the increased probability of creating a phonon ($\omega > 0$) versus destroying one ($\omega < 0$).

If a phonon mode is under-damped, then equation 3.56 can be used directly to fit

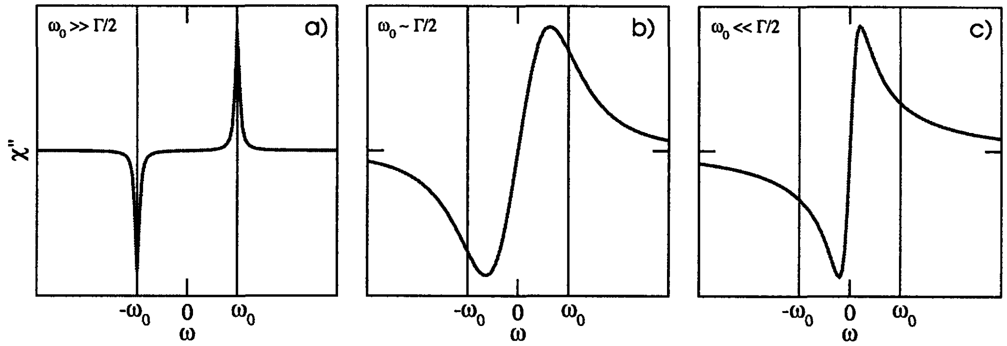

Figure 3-31: Plot of damped harmonic oscillator response function for a) under-damped, b) strongly damped, and c) over-damped cases

the lineshape. However, when the phonon becomes over-damped ω_1 (the peak center) is purely imaginary, and the two well defined peaks at $\pm\omega_1$ become a single peak centered about $\omega = 0$. Because of this, Γ, ω_0 are no longer well defined quantities. Useful information can be extracted, however, by expanding $S(Q,\omega)$ for $2\omega_0 << \Gamma$. In this limit equation 3.56 becomes [75]

$$S(Q,\omega) \approx \frac{k_B T}{\hbar\omega_0^2} \frac{A\gamma}{\omega^2 + \gamma^2}, \tag{3.58}$$

where $\gamma = \omega_0^2/\Gamma$, and the high temperature limit of $n(\omega) + 1$ ($k_B T >> \hbar\omega_0$) has been used. The latter approximation is justified by the argument that usually $\omega_0 \approx 0$ for an over-damped mode, but in general this need not be the case. For our purposes, however, this approximation is sufficient.

Spectral Correlation Function

Equation 3.56 is a very general and widely applicable response function for many different types of excitations. A fit to this equation provides valuable information about the energy, width and amplitude of an excitation. In the case of a phonon, In the harmonic approximation, these fitted parameters are well defined, and can be calculated for a given lattice. When the the fitted values from an observed phonon deviate significantly from the calculated values based on harmonic lattice potential, then anharmonic corrections must be taken into account.

Generally, anharmonicity is introduced by some weak interaction, which can be treated quantum mechanically using time dependent second order perturbation theory. This will add an additional term to the (undamped) harmonic phonon correlation function $1/(\omega^2 - \Omega_0^2)$.

$$A(\omega) = \frac{1}{\pi}\Im\left[\frac{1}{\omega^2 - \Omega_0^2 - \Pi(q,\omega)}\right], \tag{3.59}$$

where Ω_0 is the harmonic or bare phonon frequency, and $\Pi(q,\omega)$ is the polarizability, or self-energy. As was the case for the response function in equation. 3.56, for a given phonon mode, one obtains $S(Q,\omega)$ from $A(\omega)$, by

$$S(Q,\omega) = |F(q)|^2 \left[1 + n(\omega)\right] A(\omega), \tag{3.60}$$

where $F(q)$ is the atomic form factor. It was our purpose at the offset of this section to derive a "better" description of the scattering process from a phonon, so in some limit of equation 3.59 we should recover equation. 3.56. First we can see that by setting $\Pi(q,\omega) = 0$, equation 3.59 is identical to equation 3.56 for $\Gamma = 0$, indicating that $\Pi(q,\omega)$ must contain information about the damping. Since $\Pi(\omega)$ is the only term which is complex, it can be broken into real and imaginary parts,

$$\Pi(q,\omega) = \Re\left[\Pi(q,\omega)\right] + i\Im\left[\Pi(q,\omega)\right]. \tag{3.61}$$

Using this in equation 3.59,

$$A_\mu(\omega) = \frac{1}{\pi}\frac{\Im\left[\Pi(q,\omega)\right]}{(\omega^2 - \Omega_\mu^2 - \Re\left[\Pi(q,\omega)\right])^2 + \Im\left[\Pi(q,\omega)\right]^2}. \tag{3.62}$$

If we then make the substitutions

$$\Re\left[\Pi(q,\omega)\right] = \omega_0(q,\omega)^2 - \Omega(q)_\mu^2 \tag{3.63}$$

$$\Im\left[\Pi(q,\omega)\right] = \omega\Gamma(q,\omega), \tag{3.64}$$

We recover the damped harmonic oscillator response, equation 3.56. At this point it is appropriate to point out that what in equation 3.59, $\omega_0 = \sqrt{\Omega_\mu^2 + \Re\Pi}$. So this illustrates that it is still possible to use equation 3.56 to model the response of a system with anharmonic contributions, however, ω_0 now takes on the role of a "quasi-harmonic" frequency, and quantifies the deviation from the true harmonic frequency due to anharmonic interactions.

Soft-Mode Picture of Structural Phase Transitions

The study of the lattice dynamics of structural phase transitions is quite unified in that most fit into what is known as the "soft-mode" picture. In this picture the frequency, ω_0 of a phonon mode softens toward zero as the transition temperature is approached until the mode becomes frozen into the new structure. Some famous materials which exhibit nearly textbook soft-mode behavior are $SrTiO_3$, $KMnF_3$, $KTaO_2$ [76][77][78].

The real question at hand is what drives the structural phase transition? The driving force in the soft mode picture can clearly be seen from equations 3.59 and 3.63. From equation 3.63, it is evident that turning on $\Pi(q, \omega)$, will cause a shift in ω_0 toward $\omega = 0$. Turning on $\Pi(q, \omega)$ can also cause a change in the phonon damping, but it isn't necessary. Even if Π is completely real (recall from 3.63 that the damping comes from the imaginary part), ω_0 can still soften to zero.

Because in a real system, there are interactions which damp the lattice vibrations, if ω_0 softens to zero, then it will pass into the over-damped regime, where $\omega_0 < \Gamma/2$, where Γ is the damping constant defined in section 3.4.3. Recall in the damped regime, it is no longer possible to independently determine Γ from ω_0. However, integrating equation 3.58 over ω gives a value proportional to the integrated intensity of our experimental peak,

$$I = A\frac{k_B T}{\hbar\omega_0^2}, \tag{3.65}$$

where A is a proportionality constant. If we plot T/I vs. T, from equation 3.65 we can see that it should be linear, with the slope proportional to ω_0^2. In other words

[78],

$$(\hbar\omega_0^2) = A(T - T_c), \tag{3.66}$$

where T_c is the critical temperature at which the structural phase transition occurs.

This was the scenario predicted by Cross and Fisher for the lattice dimerization in TTFCuBDT[22]. Through detailed studies of diffuse x-ray scattering on this and other materials, many characteristics about the phonons driving the phase transition were deduced[29]. It wasn't until the discovery of the inorganic spin-Peierls compound was discovered that detailed, systematic studies of the phonon dynamics and symmetries via neutron scattering were possible[28].

3.4.4 Cross-Fisher Polarizability

One of the most often cited theoretical study of the spin-Peierls transition was that of Cross and Fisher (CF) in 1979. The theories up to that point were static theories which treated both the phonons and the spin-system adiabatically, using mean field theory. For the phonons this is reasonable, but for the spin system in 1D, fluctuations make this a poor approximation[22]. Cross and Fisher improved on this by calculating the spin correlations weakly coupled to a lattice distortion, while still treating the phonons adiabatically with mean-field. From the spin-lattice correlation function, they calculated a polarizability or self-energy $\Pi(q, \omega)$ for the weak coupling limit. For the purpose of this work, it a phenomenological discussion of their end result is sufficient. The reader is directed to the original work of CF in reference [22] for the theoretical details.

The CF approach starts with the Heisenberg Hamiltonian for non-interacting chains with nearest neighbor antiferromagnetic coupling

$$H_s = \sum_l J(l, l+1)\mathbf{S}_l \cdot \mathbf{S}_{l+1}. \tag{3.67}$$

The idea is to derive how the spin-coupling constant, J, changes with small lattice distortions, i.e. phonons. To first order in atomic displacement, J is given by

$$J(l,l+1) = J + \frac{1}{\sqrt{N}}\sum_{q} g(q)Q(q)e^{iq}\left(1-e^{iql}\right), \tag{3.68}$$

where $Q(q)$ is the phonon normal mode coordinate, and $g(q)$ is a weakly q-dependent coupling of the spin to the lattice distortion. The spin-phonon interaction generates the phonon self-energy, $\Pi(q,\omega)$ given by

$$\Pi_{CF}(q,\omega) = |g(q)(1-e^{iq}|^2 \int dt e^{i\omega t}\sum_{l} e^{-iql} \times -i\Theta(t)\langle[\mathbf{S}_l\cdot\mathbf{S}_{l+1},\mathbf{S}_0\cdot\mathbf{S}_1]\rangle. \tag{3.69}$$

The final step is to calculate the dimer-dimer correlation, which CF do using bosonization. It is also possible to calculate the dimer-dimer correlation by conformal field theory[79], which yields an identical result in the long wavelength limit. After working out the details of the dimer-dimer correlation, the CF self energy becomes

$$\begin{aligned}\Pi_{CF}(q,\omega) = -0.37\,&|(1-e^{iqs})g(q)|^2 \\ &\times I_1\left(\frac{\omega+c(q-2k_f)}{2\pi T}\right)\times I_1\left(\frac{\omega-c(q-2k_f)}{2\pi T}\right)\frac{1}{T},\end{aligned} \tag{3.70}$$

where

$$I_1(k) = \frac{1}{2\pi}\int_0^{\infty} e^{ikx}(\sinh x)^{-1/2}dx = \frac{1}{\sqrt{8\pi}}\frac{\Gamma\left(\frac{1}{4}+\frac{1}{2}ik\right)}{\Gamma\left(\frac{3}{4}+\frac{1}{2}ik\right)}, \tag{3.71}$$

$2k_f = \pi/s$ is the zone center (for the half-filled band), and c is the spin-wave velocity, which, from the Bethe Ansatz for a linear spin-1/2 chain, is $c = \pi Js/2$, where s is the atomic spacing. Figure 3-39 in section 3.4.5 shows plots of equation 3.70 as a function of ω, evaluated at different values of q. The details of these various lineshapes will be discussed in detail with special relevance to the implications on fitting real phonon data.

By rewriting the definition of $\Re[\Pi(q,\omega)]$ in equation 3.63, CF defines the spin-Peierls phase transition temperature, T_c,

$$\omega_o^2 = \Omega_\mu^2 + \Pi_{CF}(q=2k_F,\omega\to 0, T=T_c) = 0. \tag{3.72}$$

At $\omega = 0$, Π_{CF} is completely real, so equation 3.72 is identical to setting $\omega_0 = 0$ in equation 3.63, with $\Pi = \Pi_{CF}(q, \omega)$. Solving equation 3.72 for g we get,

$$g = \frac{\Omega_0}{4}\sqrt{5\pi T_c}, \tag{3.73}$$

making T_c the temperature at which $\omega_0 \to 0$.

The self energy in equation 3.70 can be used together with equation 3.59 to estimate the anharmonic correction to the frequency of the phonon mode which modulates the lattice dimerization. In section 3.4.5 this analysis will be applied to a soft phonon observed in TiOCl using inelastic x-ray scattering.

3.4.5 Lattice Dynamics in TiOCl

The starting point for our study of the lattice dynamics in TiOCl is first to identify a phonon which changes upon approaching T_{SP}. If such a phonon is found, then the temperature dependence can be tested against the CF theory in order to ascertain whether or not this is a reasonable theoretical model for this system. Thus far the only work on the lattice dynamics for TiOCl has been Raman and IR measurements of the zone center optical modes [80] [81]. No evidence for a soft mode was indicated. These techniques are only sensitive to modes having specific symmetries, and the wavelength used is much greater than the interatomic spacing, limiting the accessible range in reciprocal space to a small region near the zone center. Due to the small sample size inelastic neutron scattering is problematic, hence the optimal tool to probe phonons away from the zone center is meV resolution inelastic x-ray scattering (IXS).

This section summarizes our experiments at SRI-3IC of the Advanced Photon Source at Argonne National Lab. The setup of the beamline was identical to that described in section 2.6. The only difference has to do with the temperature stability of the monochromator. Section 2.6 states that the monochromator temperature is maintained constant by cryo-cooling. This wasn't the case for our experiment. The temperature was left to float which resulted in a 2-3 meV fluctuation in the zero of energy over the course of several hours. This was corrected by a Fortran script which compared the relative temperatures measured at various points in the monochromator and analyzer from which the energy shift was calculated. This shift was then subtracted from the measured energy values. All of the "raw" data shown in this section have been corrected for temperature drifts and normalized to the monitor. The position of the quasi-elastic peak (≈ 0) is evidence for the effectiveness of the correction.

Two different samples, Sample 1 and Sample 2 consisting of co-aligned crystals with total thickness of 20 μm and 40 μm respectively, and a mosaic spread of about 2-3 degrees, were mounted in transmission geometry with an incident photon energy of 21.3 keV. In transmission, the number of scattering planes and absorption length are competing factors in the scattered intensity, the maximum being about 1 attenuation length, which for 21.3 keV, was $\approx 400\mu m$. Our sample thickness was well below the scattering length where the scattering intensity roughly scales with the thickness, therefore, the scattering intensity from sample 2 was approximately twice that of sample 1.

Since the the soft phonon is expected to be polarized in a manner similar to the commensurate distortion, we began the investigation on the longitudinal phonons along the (0 K 0) direction (where the commensurate peak was observed). The data were measured on different runs using different samples. The samples used in the first and second runs were samples 1 & 2 respectively (see above). There were a few modifications to the beamline between the two runs. One of the modifications which affected our measurement significantly was the removal of a Ge-111 crystal used to deflect the beam in order to enable access to higher scattering angles. This crystal is illustrated schematically in 2-19, and described in the text of section 2.6. The end result of this modification was that for a large portion of our data, we were only able to scan a fraction of the Brillouin Zone (BZ), namely from 1.5 to 1.78 in r.l.u. along K, where 1 to 2 represents 1 full BZ. We did try reaching the zone center at near 1 (i.e. 0 1 0), but this is not an allowed Bragg reflection, therefore the phonon scattering intensity is effectively zero. When the Ge crystal was available, we were able to access a range in K from about 1 to 2.8 r.l.u, which crosses the BZ center at 2.

Figure 3-32a shows energy scans for different values of reduced momentum transfer, measured $q = 2 - K$, at $T = 100K$ and $T = 300K$, with a constant offset added for clarity. In addition the datasets for $T = 100K, q = 0.05, 0.1$ have been scaled for better comparison with the other lower intensity datasets. To quantify the phonon behavior, the data were fit to the harmonic oscillator response function, which was discussed in 3.4.3 In order to extract information about the intrinsic peak width, we convoluted our fitting function with the instrumental resolution function [44]

$$R(\omega) = I_o \left\{ \frac{2\eta}{\pi\gamma} \left[1 + 4 \left(\frac{\omega}{\gamma} \right)^2 \right]^{-1} + (1 - \eta) \frac{2}{\gamma} \left(\frac{\ln 2}{\pi} \right)^{1/2} \right.$$
$$\left. \times \exp \left[-4 \ln 2 \left(\frac{\omega}{\gamma} \right)^2 \right] \right\},$$

where γ is the FWHM, I_o is the integrated intensity, ω is the energy, and η is a mixing parameter. The parameters $\eta = 0.46$ and $\gamma = 2.29(3)$ were determined by fitting the resolution function to an energy transfer scan from a Plexiglas sample which isotropically scatters within a bandwidth of zero energy transfer much less than the spectrometer resolution (see section 2.6). Another source of instrumental broadening comes from scanning a finite resolution width in q through a sloped dispersion curve (figure 3-33). If the energy width is a delta function then the width due to a finite δQ passing through a slope dE/dq will be $\delta E = dE/dq\delta Q$. The Q-resolution of the spectrometer is primarily determined by a slit cut in the mask placed over the face of the analyzer. Since the beam is $100\mu m$ width μrad divergence, and the slit is 4 cm wide, the resolution function in Q is simply a rectangle of width δQ. To estimate δQ, we need need to calculate the angle of the slit opening. The analyzer is at a distance of 5.8 m from the sample, therefore the angle is $\alpha = \arctan(.02/5.8) = 0.198^o = 0.0035rad$. The Q resolution can be calculated by differentiating Bragg's

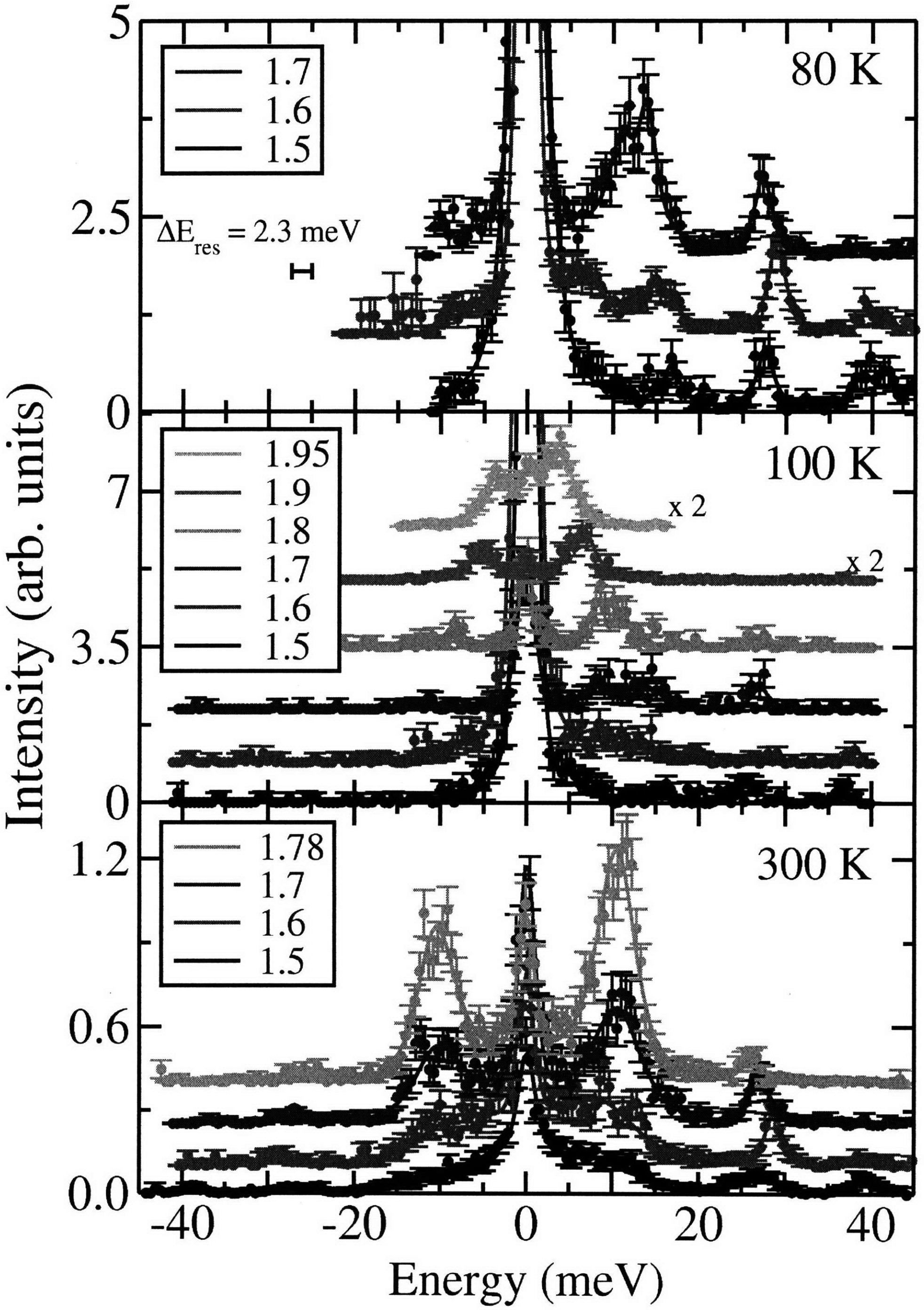

Figure 3-32: Raw IXS data measured along the (0 K 0) direction as a function of $q = (02 - \xi 0)$ for T = 80 K, T = 100 K, T=300 K. The 100 K datasets at q=0.05 and q=0.1 have been scaled by the indicated factors, and a constant offset has been added to the data for clarity. The lines are fits to equation 3.56 convoluted with the resolution function (see text).

law, $Q = 2k \sin\theta$.

$$\begin{aligned}\delta Q =& 2dk \sin\theta + 2k\cos\theta\delta\theta \\ =& \frac{2\pi}{hc}\delta E \sin\theta + \frac{4\pi}{hc} E\cos\theta\delta\theta \\ =& \frac{2\pi}{hc}E\left(\frac{\delta E}{E}\sin\theta + 2\cos\theta\delta\theta\right),\end{aligned}$$

where h and c are Planck's constant and the velocity of light respectively. The ratio $\delta E/E \sim meV/keV \sim 10^{-6}$ much smaller than $\delta\theta$ so the first term can be neglected, leaving

$$\delta Q \approx \frac{4\pi E}{hc}\cos\theta\delta\theta \approx 1.013E\delta\theta, \tag{3.74}$$

where the approximation $\cos\theta \approx 1$ has been used since the maximum scattering angle attainable is $2\theta = 18^o$ corresponding to $\cos(9^o) = .98$. The prefactor 1.013 is $4\pi/hc$ in $(keV\text{Å})^{-1}$. Using $E = 21.3keV$ and $d\theta = 0.0035$ we find $\delta Q \approx .075\text{Å}^{-1} = .04$ r.l.u along K. Convoluting the dispersion curve with the energy width corresponds to scanning along the diagonal of the resolution rectangle (see figure 3-33), with length

$$\delta E' = \sqrt{\delta E^2 + (dE/dQ)^2\delta Q^2}. \tag{3.75}$$

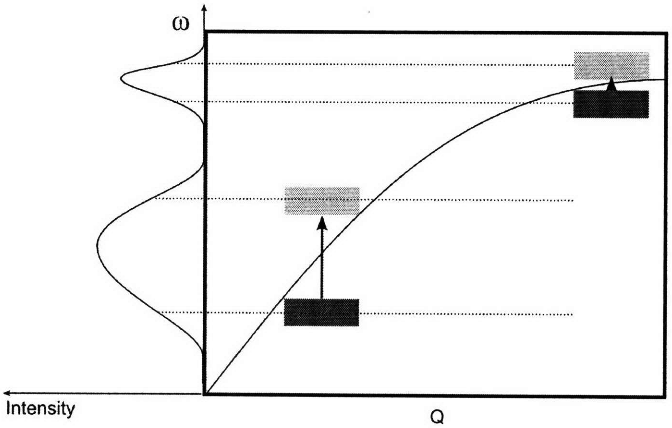

Figure 3-33: Illustration of how passing a resolution function with finite width in Q through a sloped dispersion curve will broaden the observed peak in energy. For the sector 3 beamline the rectangular resolution function shown is a good estimate (see text).

The slope of the dispersion curve $dE/dQ(q)$ was estimated from non-convoluted fits to the peak positions. The calculated $\delta E'(q)$ was then substituted into γ of the resolution function. Putting everything together, the function used to fit the data was

$$S(Q,\omega) = A_0 R(\omega', q) + R(\omega') * \left([n(\omega') + 1] \sum_i^{\#peaks} \frac{A_i \Gamma_i \omega'}{(\omega'^2 - \omega_{0i}^2)^2 + \Gamma_i^2 \omega'^2} \right), \quad \omega' \equiv \omega - \omega_c, \tag{3.76}$$

where $*$ is the convolution operator, and ω_c is a fitted parameter to correct any systematic energy shifts.

The fitted peak positions are plotted in figure 3-34 along with calculated dispersion curves for phonons having vibrational symmetries compatible with our scattering geometry. The phonon curves were calculated using the GULP[66] lattice dynamics software (see section 3.4.1). The main idea behind the shell model calculation is to find a phenomenological potential which models the strong short-range interactions resulting from the overlap of neighboring electron clouds in close proximity[69]. The validity of a potential model can be tested by letting the program calculate the resulting equilibrium structure. With no potentials defined (i.e. only coulomb interactions) the atoms were too tightly bound, resulting small lattice parameters, especially along the c-direction. The four Buckingham potential interactions served to add a repulsive force to spread the atoms out. The additional interaction is a three-body interaction between neighboring Ti and Cl atoms. It is simply a harmonic expression which penalizes deviation from a defined angle. This interaction was used with an angle of 90^o for $Ti - Cl - Ti$ bonding to favor the octahedral coordination shown in figure 1-4b. It turned out that these were the only potentials required to settle the system into an equilibrium structure nearly identical to the experimental unit cell of ref[48]. (see table 3.1). The final test for having the proper atomic environment is to perform the lattice dynamical calculation. If the atoms have settled into a saddle point, then this will manifest itself as a negative eigenvalue of one or more of the normal modes. The potential environment in table 3.1 yielded all positive eigenvalues for all q values. While there are other parameters which go into the calculation, they are not given

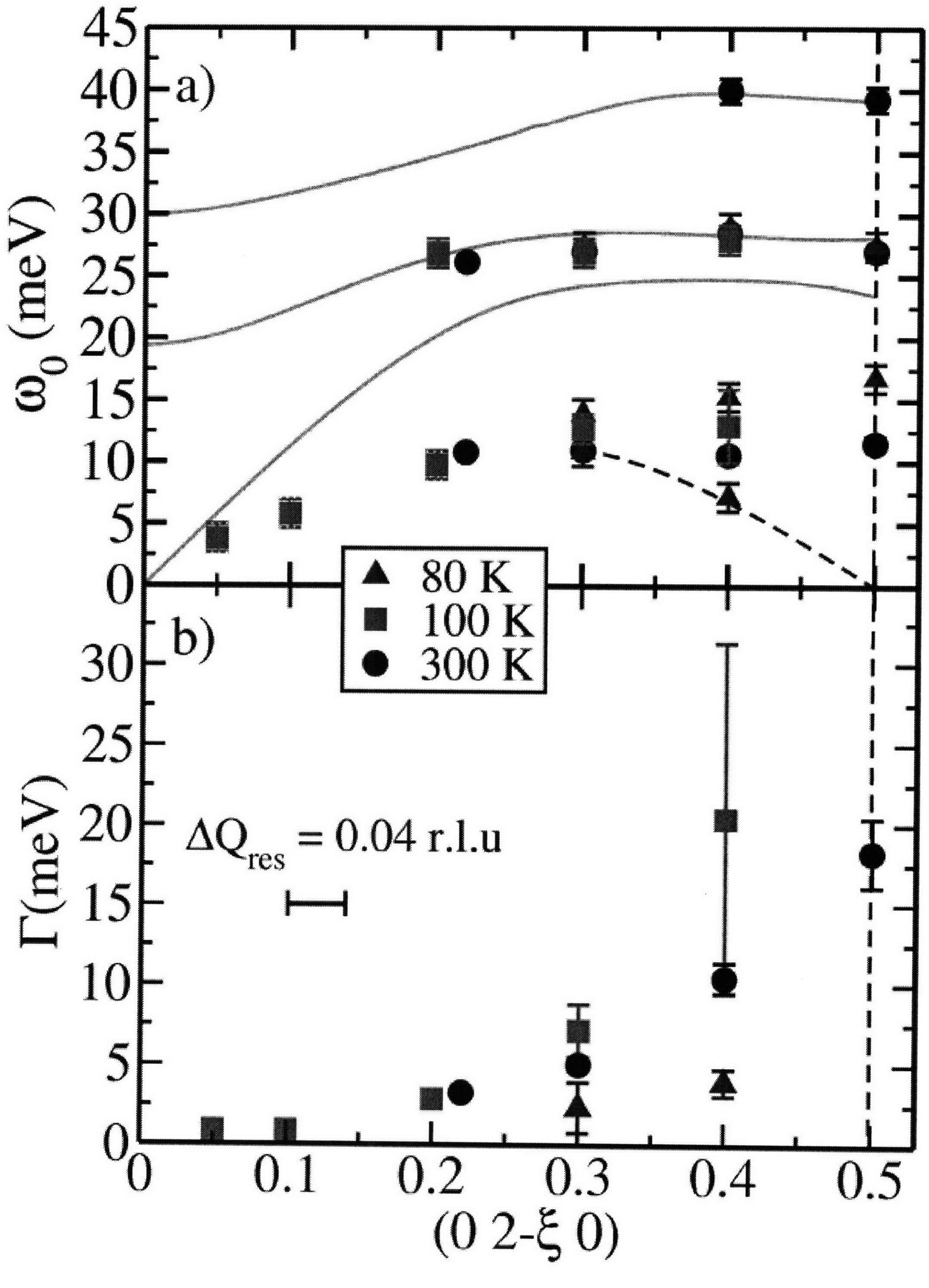

Figure 3-34: Fitted peak center and width for the data in figure 3-32. The solid lines are phonon dispersions with the allowed vibrational symmetry for scattering in the (0 K 0) direction calculated using a shell model (see 3.4.1). The dashed line is a guide to the eye.

Buckingham $Ae^{\frac{r}{\rho}}-\frac{C}{r^6}$

Bond Pair	A (eV)	ρ (Å)	C(ev Å^6)
Ti-O	2524.38	0.29	0
Ti-Cl	2541.81	0.29	0
Cl-Cl	8029.88	0.33	237.7
Cl-O	8286.91	0.26	62.2

Three Body $\frac{1}{2}k_2(\theta-\theta_0)^2+\frac{1}{6}k_3(\theta-\theta_0)^3+\frac{1}{24}k_4(\theta-\theta_0)^4$

Atoms	k_1(ev/rad^2)	θ_0	(k_3=k_4=0)
Cl-Ti-Cl	20.4	90	

Lattice Parameters

Lattice par.	Experimental	Calculated
a(Å)	3.786	3.784
b(Å)	3.361	3.368
c(Å)	8.045	8.045

Atomic Positions

Atoms	Experimental	Calculated
Ti (core)	0.8807	0.8814
O (core)	0.9446	0.9586
Cl (core)	0.6680	0.6661
Ti (shell)	0.8807	0.8794
O (shell)	0.9446	0.9600
Cl (shell)	0.6680	0.7041

Table 3.1: Parameters used in shell model calculation of the phonon dispersion curves in figure 3-32

here, since the tabulated values were used. These include the core-shell spring constants for each of the atoms, and the effective charge. The values for these were taken from reference [68][2]. The shell model succeeds at predicting the nearly dispersionless optical modes at 28 meV and 40 meV. However, there is some inconsistency with the two lower energy modes. Since both modes disperse away from E=0 as $q \longrightarrow 0$, they are acoustic modes. Following standard phonon dispersion properties, the lower and higher energy modes are transverse and acoustic modes respectively. However, observing a transverse mode shouldn't be possible in out scattering geometry which only selects modes polarized along the (0 K 0) direction, that is, we are only measuring longitudinal modes. Some light can be shed on the problem by looking at the calculated eigenvectors for the two phonons. The normal mode eigenvector components are shown in figure 3-35 along a picture of the unit cell with arrows indicating the approximate relative direction and magnitude of the vibrations. The observation is that while the polarizations are primarily parallel to b and c for the 11.3 meV and 3.2 meV modes respectively, there is a small component in the orthogonal direction. Since the $\vec{\xi_i} \cdot \vec{Q}$ term in the inelastic cross-section selects out only those components parallel to the b-axis. For the 3.2 meV mode these point in opposite directions, and

---

[2] The meanings of these parameters are discussed in section 3.4.1

will therefore cancel when the coherent sum is invoked. We can therefore predict the observed modes by explicitly performing the dynamical structure calculation for the eigenvalues and eigenvectors given by the shell model calculation. Figure 3-36 models all of the 100 K and 300 K scans shown in figure 3-32. From this we can clearly see only the three modes associated with the calculated dispersion curves in figure 3-32. In addition to the q-dependence at 80 K, 100 K, 300 K, the temperature dependence of the phonon spectrum at (0 1.5 0) ($q = 0.5$) was measured. Figure 3-37a contains energy scans as at different temperatures offset from each other for clarity. It appears from these data that the acoustic mode which broadens for $q- > 0.5$ (figure 3-34b) softens upon cooling. Fits to the data revealed that at T=200 K, the mode becomes overdamped, meaning Γ and ω_0 could no longer be uniquely determined. However, in section 3.4.3, the damped oscillator model was expanded in the overdamped limit, and we saw that while it isn't possible to fit ω_0 directly, the integrated intensity is

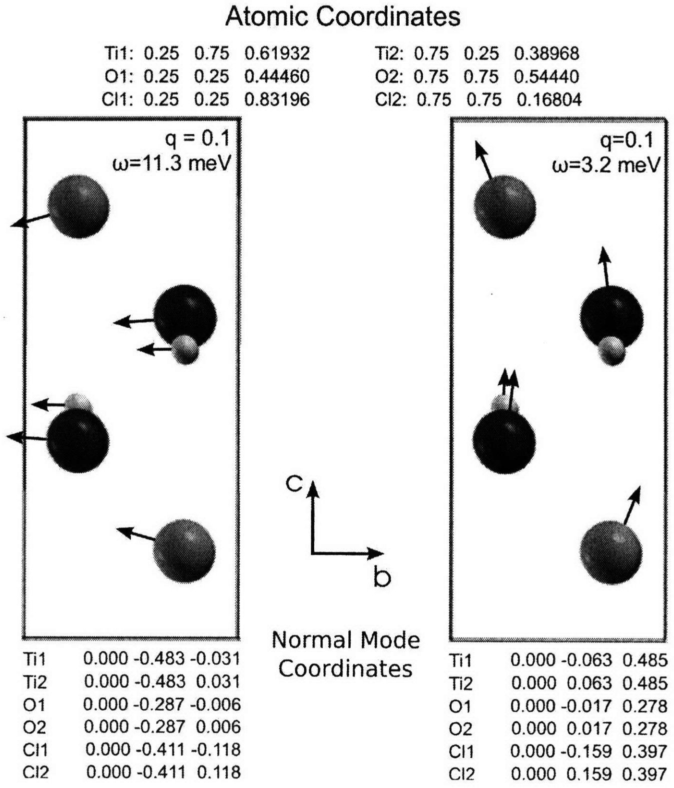

Figure 3-35: Diagram showing the atomic motions associated with the two acoustic mode vibrations calculated to be present along the (0 K 0) direction.

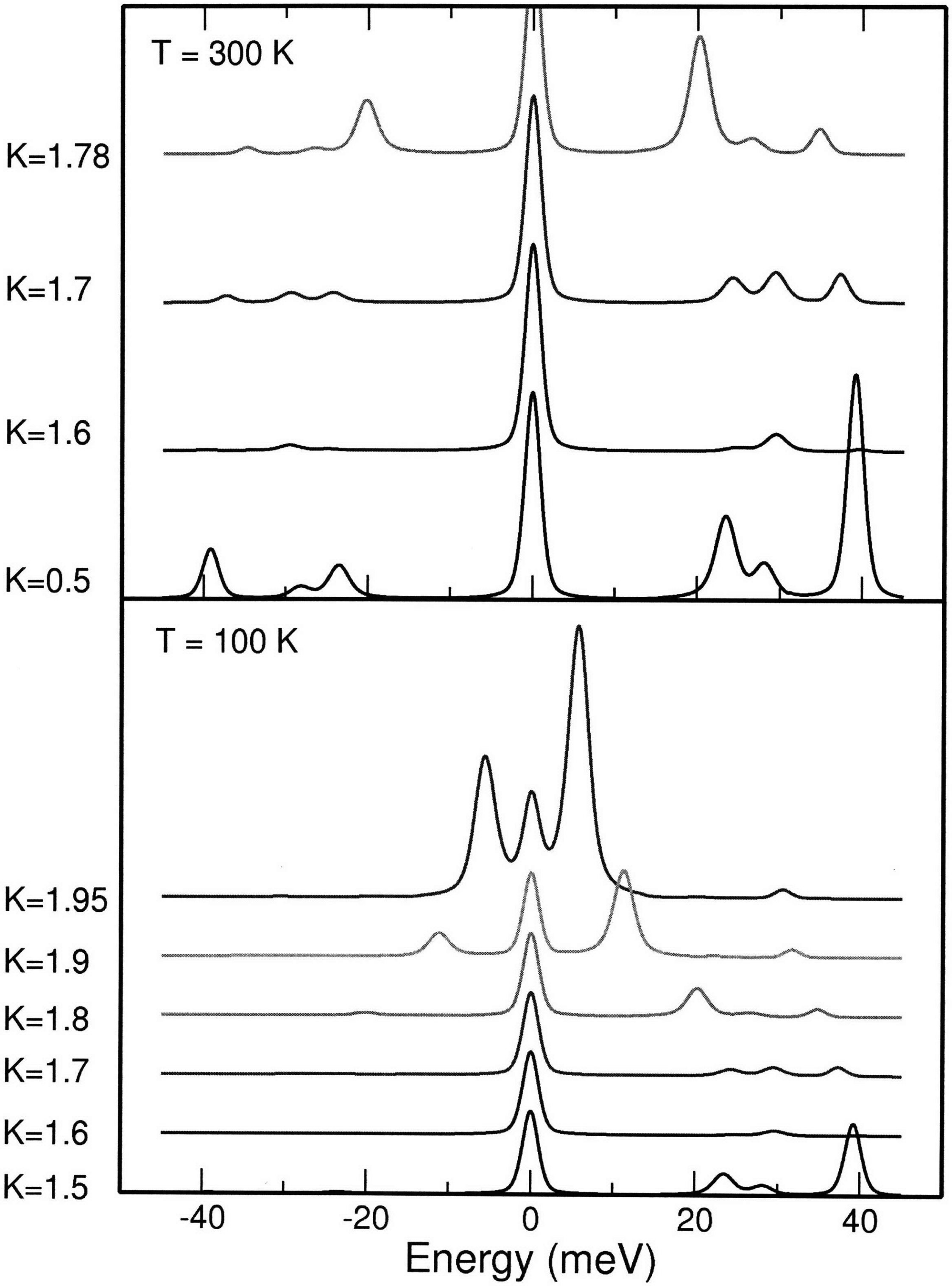

Figure 3-36: Plot of the dynamic structure factor for all of the observed modes. The peak positions and intensities were extracted from the shell model calculation.

proportional to T/ω_0^2. Therefore a plot of T/I should be proportional to ω_0^2. Mean field theory predicts that

$$\omega_0^2 = A(T - T_c), \tag{3.77}$$

where T_c is the temperature of the structural transition, and A is a temperature independent proportionality constant. Figure 3-37b shows a line joining T/I for 100 K, 150 K extended to higher and lower temperatures. I would like to emphasize that this is not a fit. We didn't find a least squares fit justified in this case for two reasons. First of all, from the error bars, we know the 100 K, and 150 K values for T/I better than for 200 K and 300 K. In addition to this, since Γ is only slightly greater than $2\omega_0$, at these temperatures, it is not clear if those data points are in the correct limit for the expansion 3.58. For 300 K, the mode is underdamped, so clearly it equation 3.58 does not apply, as indicated by its large deviation from the linear behavior. With these considerations in mind we can see at the x-intercept of the line is near T_{c_2}. The exact value is 88.5 K, is within error of 92 K. The final temperature dependence ω_0^2/Γ is a value which results from fitting to equation 3.58. The temperature dependence of this is shown in figure 3-37c. While the significance of this value isn't obvious, it is remarkable to note that it also tends toward zero around T_{c_2}. The important conclusion to be made from the temperature dependence of two independent peak parameters point to a transition temperature of T_{c_2}, not T_{c_1}. This observation substantiates our model of the incommensurate structure as being a small modulation of dimer pairs, since as far as the phonons are concerned the structural transition occurs at T_{c_2}. If this is true then the phonon which is softening should have a vibration pattern consistent with the dimerized structure. The shell model calculation indicates that at $q = 0.5$, the longitudinal mode becomes degenerate with the transverse mode polarized along c. There exists, therefore, an infinite number linear combinations of b and c polarizations which will have the same energy[69]. This is illustrated in figure 3-38 by showing half of the atoms vibrating along b, and half along c. Since we are only measuring the b-component, we can ignore the c-vibrations. If we do this, then all eigenvectors will point along the same direction in

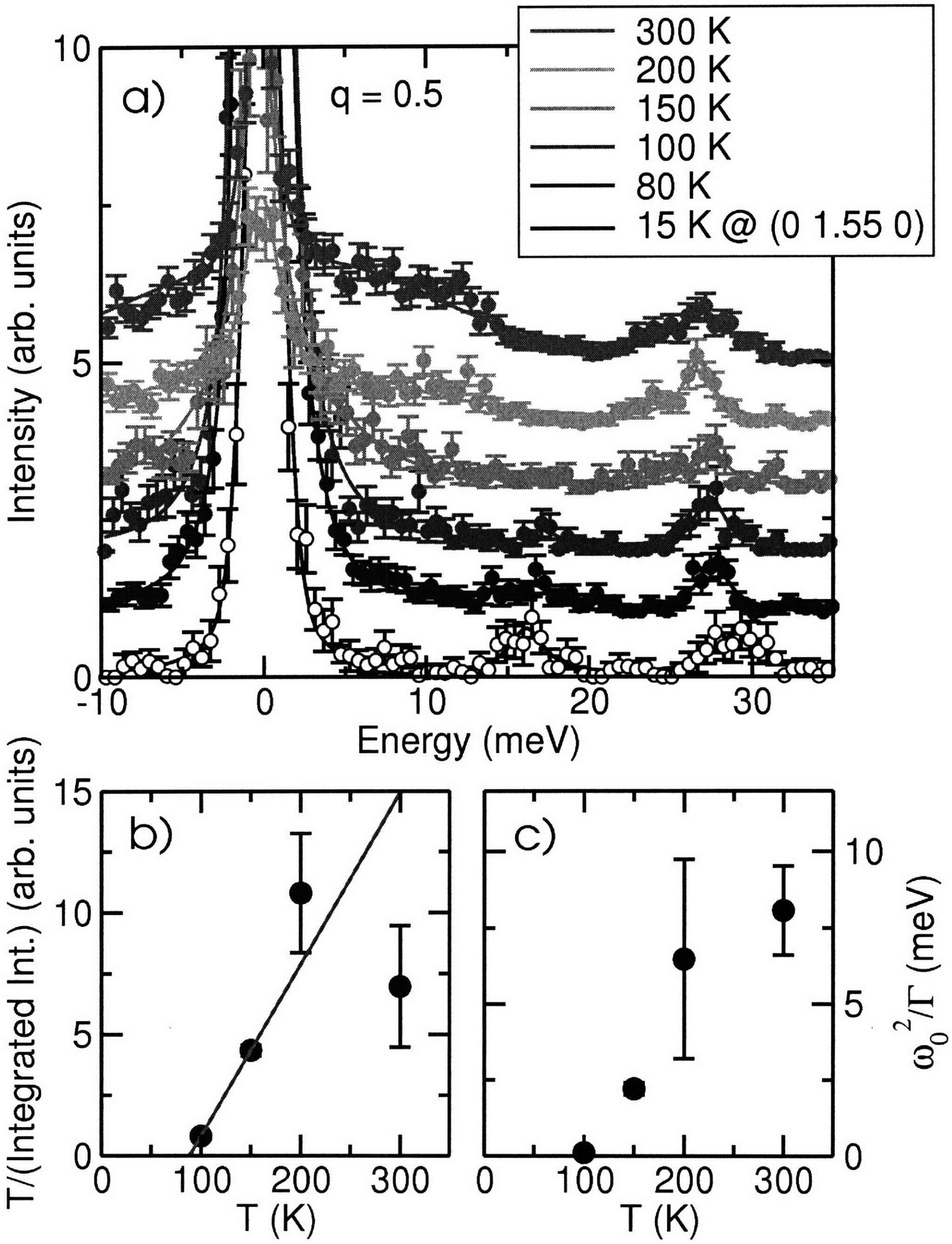

Figure 3-37: a)Energy scans measured at Q=(0,1.5,0) for different temperatures. The acoustic mode shows a clear softening, and as a result becomes overdamped. The plot in b) is the temperature dependence of T/I, a value proportional to ω_0^2 for the overdamped mode with a line draw through the 100 K, 150 K points indicating a T_c of 88.5 K (see text). The temperature dependence of ω_0^2/Γ, a parameter independent of T/I which also tends to zero around 100 K. This implies that the spin-Peierls transition occurs at 92 K, rather than 65 K, consistent with our model of the incommensurately modulated dimer pairs.

b. It isn't obvious from one unitcell that this has the form of the lattice distortion. However, we need to take into account that this is a zone boundary phonon, which corresponds to a vibration with wavelength 2b. In other words, atoms in neighboring unit cells vibrate out of phase with each other. This out of phase vibration is visualized in figure 3-38. Based on the arrows drawn, the zone boundary acoustic mode frozen at its maximum distortion is a dimerized lattice along b. Therefore, based on the vibrational symmetry, treating this mode as the soft mode driving the transition is justified.

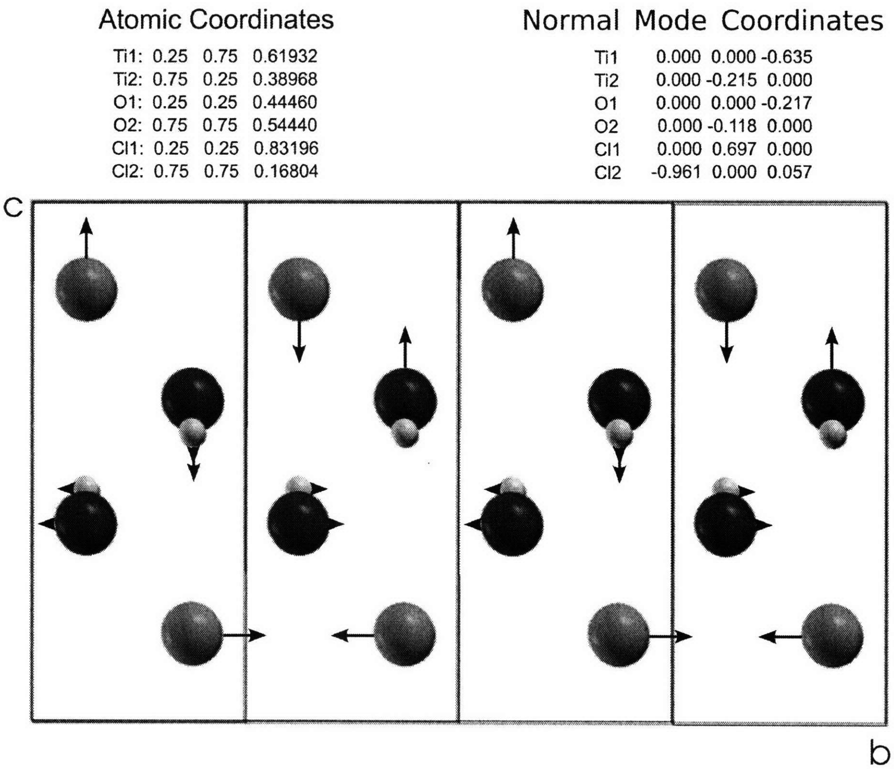
Atomic Coordinates

Ti1:	0.25	0.75	0.61932
Ti2:	0.75	0.25	0.38968
O1:	0.25	0.25	0.44460
O2:	0.75	0.75	0.54440
Cl1:	0.25	0.25	0.83196
Cl2:	0.75	0.75	0.16804

Normal Mode Coordinates

Ti1	0.000	0.000	-0.635
Ti2	0.000	-0.215	0.000
O1	0.000	0.000	-0.217
O2	0.000	-0.118	0.000
Cl1	0.000	0.697	0.000
Cl2	-0.961	0.000	0.057

Figure 3-38: Eigenvector of the zone boundary acoustic mode. At the zone boundary, the b and c acoustic modes are degenerate, meaning there is an infinite number of linear combinations of the b and c polarizations. This is illustrated by showing half of the atoms with one polarization and half with the orthogonal polarization. However since it is a zone boundary mode, the center of mass of the vibration has to be the shared edge of two neighboring unit cells. Therefore, the atom in one unit cell must vibrate completely out of phase with its counterpart in the neighboring unit cell.

3.4.6 Spin-Phonon Coupling in TiOCl

Our fits to the damped harmonic oscillator seem to suggest that the longitudinal acoustic mode along the (0 K 0) is strongly damped, and perhaps even softened at T=300 K. The temperature dependence of the fitted peak parameters also imply that $\omega \rightarrow 0$ at T_{c_2}. Section 3.4.3 discussed how information about microscopic interactions driving a structural phase transition can be acquired by inserting an anharmonic correction term to the harmonic oscillator response function. This correction comes in as the polarizability, $\Pi(q, \omega)$. In section 3.4.4 an explicit $\Pi(q, \omega)$ for the coupling of a phonon to the electron spin was presented. The next round of fitting was then performed to test the validity of the Cross & Fisher model for our system, and if applicable, extract a value for the spin-phonon coupling. The energy range was truncated to the range -20meV$\leq$Ele20meV, so that only the acoustic mode was fitted. The function used to fit the data was

$$S(q, \omega) = [n(\omega) + 1] \cdot \Im \left[\frac{A}{\omega^2 - \Omega_0^2 - 2\Pi_{CF}} \right], \tag{3.78}$$

where Π_{CF} is defined in section 3.4.4, and A is a scaling factors related to the peak amplitude. Since it doesn't affect the physics of Cross & Fisher it be omitted from the remaining discussion. Note, however, that all fits have A as an adjustable parameter. At the zone boundary, $\Pi_{CF}(q, \omega)$ reduces to

$$\Pi(q, \omega) = -0.74 g^2 I_1 \left(\frac{\omega}{2\pi T} \right), \tag{3.79}$$

therefor the only adjustable parameters are the spin-phonon coupling, g, the bare phonon frequency, Ω_0. From equation 3.79 we can see that g quantifies the magnitude of the CF anharmonicity. Since g is real, it will scale both real and imaginary parts of $\Pi_{CF}(q, \omega)$, which from equations 3.63 means it will affect both the peak width and the shift of ω_0 from Ω_0. Figure 3-39 contains the CF function for various input parameters and independent variables. Panels a,b show the real and imaginary parts of $\Pi(\omega)$ at the zone boundary, and $T = 300K$. For this g = 80, 160 meV$^{3/2}$ the

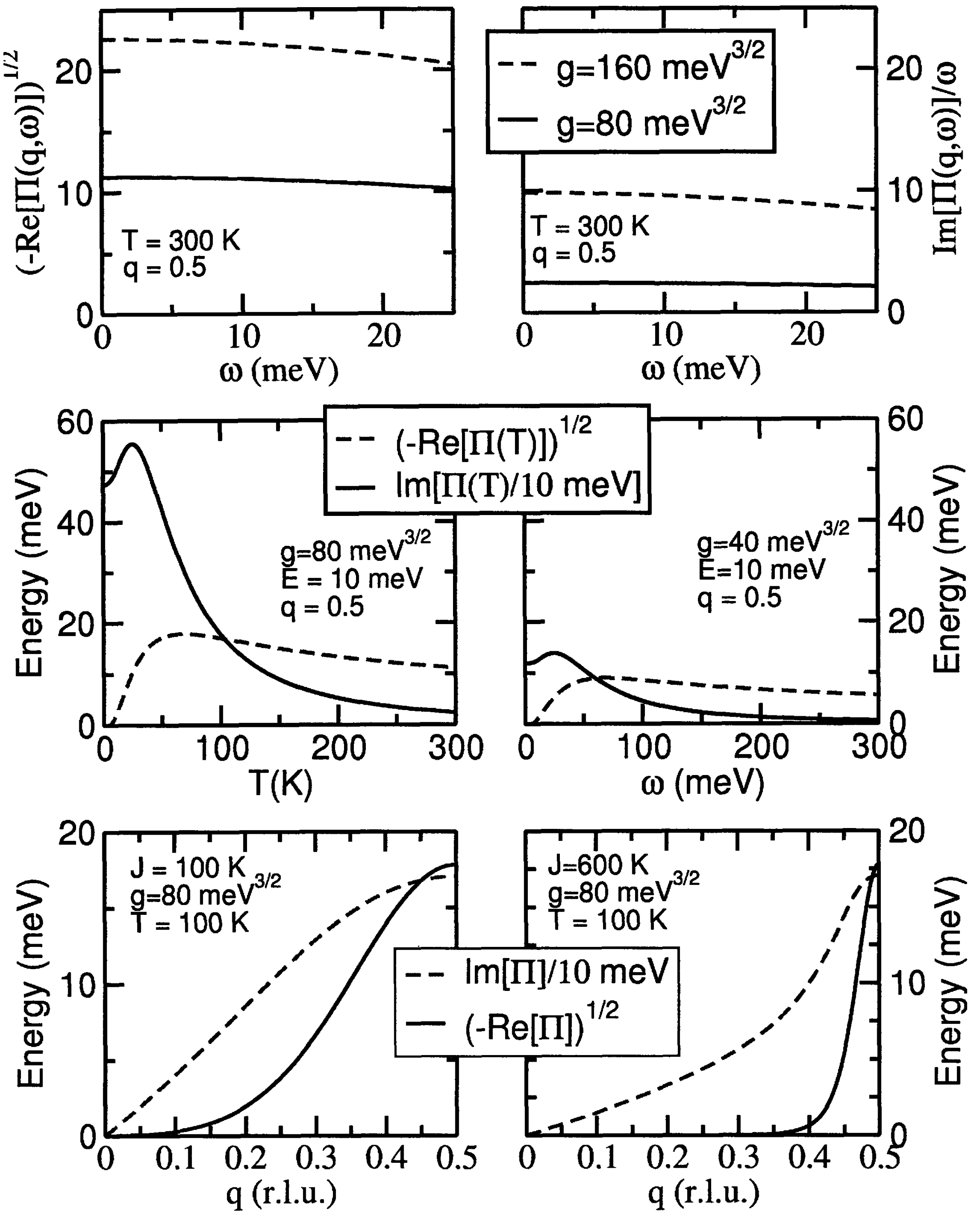

Figure 3-39: Survey of the dependence of $\Pi_{CF}(q,\omega)$ on the various parameters. All panels are comparing $\sqrt{-\Re[\Pi]}$ with $\Im[\Pi]/\omega$, which from equation 3.63 is equivalent to comparing the width with the shift from Ω_0. Panel a),b) contain the real and imaginary parts of $\Pi_{CF}(\omega)$ at different g values, for q=0.5, and T=300K. Panels c),d) compare the temperature dependence for two different values of g. Finally, e),f) show the dependence of $\Pi(q)$ on J.

ratio of the shift to the broadening is ~ 2. Panels c),d) show how Π_{CF} varies with temperature for two different values of g. Both parts vary slowly at high T, gradually increasing for decreasing temperature. The damping ($\Im[\Pi]/\omega$) fraction only becomes significant for low temperature, the exact range of which depends on g. The final set of plots shown in panels e),f) show the q-dependent of Π_{CF} for different values of J. For large J, $\Pi_{CF}(q)$ is sharply peaked about $q = 0.5$, but as J decreases, $\Pi_{CF}(q)$ broadens. This means that for a given q value, lowering J, will effectively increase Π_{CF}. Since g also affects the magnitude of Π_{CF}, J,g are not independent parameters, which is problematic for fitting. However, since $\Pi_{CF}(q = 0.5, \omega)$ is independent of J, and g is roughly q-independent, g can be determined at $q = 0.5$, then fixed for the $q \neq 0.5$ fits.

In our initial analysis, we wanted to let the fits determine the values for all of the adjustable parameters, which we could then compare to known values giving us a measure of the validity of the theory for this system. However, this required special care in order that all parameters were uniquely determined. In the previous paragraph, we concluded that g must be fitted at the zone boundary so that it doesn't interfere with J. From figure 3-32, there are 4 datasets at $q = 0.5$ with $T >$T$_{c_2}$. However, only one of those is underdamped, which we learned in section 3.4.3 is necessary to uniquely determine Ω_0,g which are related to (ω_0,Γ) through equation 3.63. So the 300 K dataset was fitted first to determine g and Ω_0. However, both of these are expected to be temperature independent, therefore, they should be determined for the remaining temperatures at $q = 0.5$. However, we found that the 300K value for g resulted in very poor fits. Rather than one broad peak at $\omega = 0$, we had two well defined peaks well away from zero. Since we know that $\Pi_{CF}(q, \omega)$ affects the position more than the broadening, we can conclude from this that g from 300 K is too large. Good fits were recovered allowing g to vary, width Ω_0 fixed as a function of temperature. Once g was determined for a given temperature, the q dependence could then be fitted letting Ω_0, J, vary with g fixed at the $q = 0.5$ value. From figure 3-32, there are two datasets as a function of q, with $T >$T$_{c_2}$, namely 100 K and 300 K. The q-dependent fits for both temperatures yielded the same value of $J = 200K$.

Since the q-dependence of J was very subtle, we were able to fix this parameter as well, leaving only $\Omega_0(q)$ to fit. Figure 3-41 summarizes the results of this fitting procedure. The fitted values $\Omega_0(q)$ shown in figure 3-41a agree better with the calculated harmonic dispersion, than the fitted values for ω_0 if figure 3-34a. Therefore one might conclude that our system is well described by the theory of Cross & Fisher. However, the dispersion of Ω_0 is only part of the story. In order to obtain good fits at all temperatures, g was allowed to vary with Ω_0 fixed. This resulted in a temperature dependent g. Equation 3.73 gives an explicit form for g in terms of $\Omega_0(q = 0.5)$ and T_c. Using our fitted value of 27 meV for Ω_0 gives $g_{Cross-Fisher} = 75$ meV$^3/2$. Figure 3-41b shows the ratio of the fitted value for g to the one just calculated using equation 3.73. A noteworthy observation is that no information about T_c was explicitly or implicitly provided during the fitting procedure, and $g/g_{Cross-Fisher} -> 1$ around T_{c_2}.

From equation 3.63it is also possible to calculate ω_0 from Ω_0, which according to 3.72 should go to zero at the transition temperature. Using the fitted values for $\Re[\Pi(q = 0.5, \omega)]$, along with the fitted value for $\Omega_0(q = 0.5)$, we see in figure 3-41c that the transition temperature according to CF is $\sim$ 98 K. An additional check which can be made is to fix g at $g_{Cross-Fisher}$, then calculate the temperature dependence

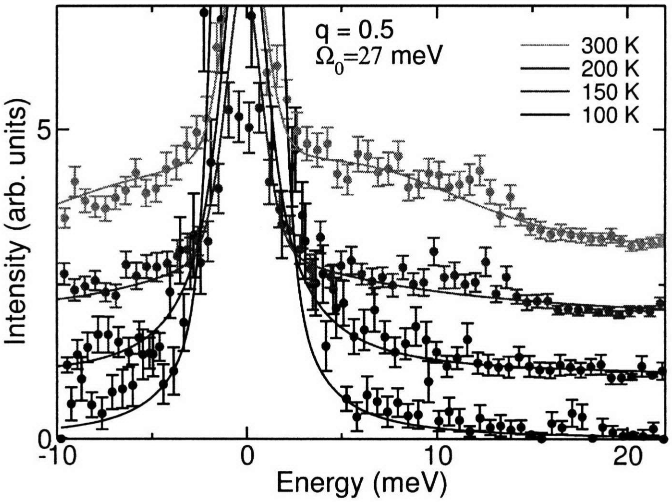

Figure 3-40: Raw data and fits to eq. at different temperatures. An offset has been added for clarity.

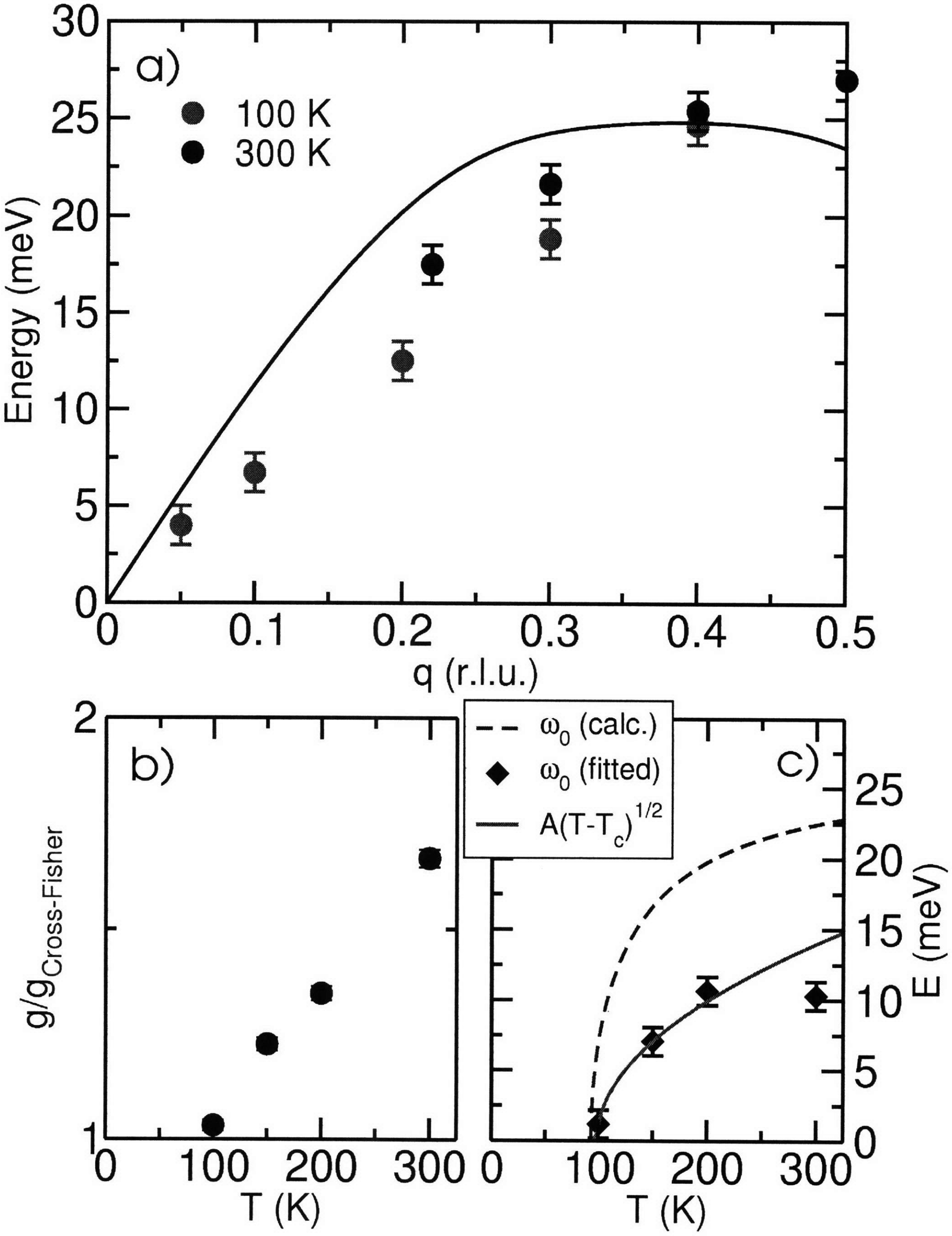

Figure 3-41: a) Fitted values for the harmonic frequency of the longitudinal acoustic mode as a function of q at $T = 100K$ and $T = 300K$, along with the harmonic dispersion expected from the shell model calculation. b) The ratio of the fitted g to g calculated using equation 3.73 (see text). The value of Ω_0 used was the 300 K, q=0.5 value from panel a). c) Plot of ω_0 values deduced from Ω_0 using equation 3.72), along with the expected ω_0 using g fixed at the value given by equation 3.73. The line through the deduced ω_0 points is a fit to A$\sqrt{T-T_c}$ help quantify T_c. The fitted result is $T_c = 98K$.

of ω_0, shown by the dashed line in figure 3-41c. The line through the data in figure 3-41c is $A\sqrt{T-T_c}$, which was used to extract our estimate of T_c.

In addition to having a temperature dependent g, the fits for $q \neq 0.5$ yielded a J of 200 K, which is a factor of 3 lower than that reported by reference [4]. By comparing the dependence of Π_{CF} on g, and J, we can see that both affect the broadening of the peak. The fitted values for g, J are consistent with increasing the broadening for $q \neq 0.5$ and $T \to 300K$. If we constrain J to be 600 K (nearly the value from [4]), then the fits for $q \neq 0.5$ significantly deviate from the measured lineshape. Essentially the peaks are delta functions centered about $\pm\omega_0$, which isn't well defined since the fit didn't converge. At q=0.5, Π_{CF} is independent of J, but g defines the broadening. If we constrain g to be $g_{Cross-Fisher}$ then again, two nearly delta function peaks appear at $\pm\omega_0$. A good fit is recovered for T=150 K, and of course T = 100 K. In a sense, this gives a range of applicability for Π_{CF}. Apparently it only contributes significantly for $q \approx 0.5$, which we may have guessed from figures3-39e,f, and for $T \to T_c$, which is also suggested in figures 3-39c,d. This leads us to conclude that there is some additional interaction which is causing significant broadening and perhaps even a softening at T=300 K.

If we use $\Omega_0(0.5) = 23meV$ from the shell model calculation, then good fits are obtained using $g = g_{Cross-Fisher} = 64meV^{3/2}$, but only for 100 K and 150 K. For 200 K, and 300 K, the peaks are at the right position, but they are about a factor of 2 too narrow. From this we can conclude that while CF predicts the correct softening (since the peak positions were correct), the broadening of our observed peak is not completely accounted for by CF.

The final conclusion from this analysis, is that the Cross & Fisher theory is applicable to the 150 K and 100 K datasets. However, assuming no value for T_c $\Pi_{CF}(q,\omega)$ converged on a value close to T_{c_2} for the transition temperature. In the scope of the spin-Peierls systems, it seems that TiOCl is the first inorganic spin-Peierls system to exhibit classic Cross & Fisher type phonon softening. Since we determined that 300 K is outside of the realm of applicability of the theory to TiOCl, the fitted value of Ω_0 at that temperature must be questioned. The predicted harmonic frequency (from the shell model) is slightly lower than this, and since it yielded good fits for 100 K and 150 K, using $g = g_{CrossFisher}$, it is reasonable to assume Ω_0 is close to this value. Using this in 1.12, we see that $\Omega_0/T_c = 2.9$, which is greater than 2.2, so according to [82] TiOCl should be anti-adiabatic, like $CuGeO_3$. However, a more recent theory by Dobry et. al. takes into account the dynamics of the transverse phonons due to inter-chain interactions, and they predict that for certain values of $\omega_\perp/T_{SP}$, the cut-off between adiabatic and anti-adiabatic can be raised to as high as 3[32]. The transverse phonon corresponding to the inter-chain interaction could either be the one polarized along a or c, since the chains are offset in both directions. In any case, we didn't measure the transverse phonons, but from the shell model calculation we predict that E for the a-transverse mode is $\sim 6.5meV$, and the c-transverse mode is of course degenerate with the longitudinal. Of these two the larger $\omega_\perp/T_{SP}$ value is obtained for the c-transverse mode, which we already know is 2.9. This corresponds to 2.7 for the adiabatic anti-adiabatic cut-off for the longitudinal mode. This is an upper bound, and the lower a-transverse mode energy will could likely raise this value as high as 3. In any case, these numbers are based on a shell model of the phonons which works well for the observed optical phonons, but does not for the acoustic phonons. At this point, we have no way to determine if the shell model is wrong or if the what we measure is a renormalized phonon frequency due to anharmonic corrections.

To conclude the discussion of the spin-phonon coupling, I present a section of a table from reference [29] which summarizes spin-phonon coupling constants for various spin-Peierls materials. I have added the newly measure value for TiOCl.

3.5 Conclusions

We have taken a long experimental journey from speculation of a spin-Peierls transition through the various experimental techniques used to piece together the story behind the transitions reported in the susceptibility by Seidel et. al. [4]. The story started with two unknown apparent phase transitions in the susceptibility, at T_{c_1}=65

K and T$_{c_2}$=92 K. From the earliest susceptibility measurements, we observed a hysteresis at T$_{c_1}$, thought at the time to be the spin-Peierls transition temperature. This already set TiOCl apart from its spin-Peierls counterparts. We later found a superlattice peak consistent with the doubling of the unitcell along b. The integrated intensity of the peak exhibited a hysteresis comparable to that of the susceptibility. So T$_{c_1}$ had proven to be a very interesting transition temperature, but it wasn't until the discovery of an incommensurate state, with an onset at 92 K that we realized the origin of T$_{c_2}$. However it wasn't until we found a suitable model for the incommensurate modulation, which was a modulation of dimer pairs, that we realized that the dimerization, and therefore the spin-Peierls transition temperature occurred at T$_{c_2}$, not $_{,}$ Then a detailed study of the lattice dynamics above T$_{c_2}$ showed the softening of the zone boundary longitudinal acoustic phonon at (0 1.5 0). The phonon was already soft, and very strongly damped at room temperature. Upon cooling the damping increased, and the phonon softened further, until reaching 0 at around 90 K. We had at this point an independent verification that the structural phase transition associated with the zone boundary LA mode along b (the vibrational pattern of which is a dimerization), occurs at T$_{c_2}$. We then turned to the theory of Cross & Fisher to find an origin of the phonon softening in the spin-phonon coupling. Our fits to this theory show good agreement over a narrow temperature and q regime. From this we could conclude that the Cross & Fisher theory only had limited applicability to our system, but additional interactions need to be considered to account for the significant broadening well above T$_{c_2}$. Comparing to past systems we find that

Material	T_c (K)	T_c^{MF}	J/k_B (K)	α/k_B (K)
TiOCl	92 K	150	660	226
$CuGeO_3$	14.3	60	160	190
$(BCPTTF)_2PF_6$	36	100	330	100-125
$(TMTTF)_2PF_6$	19	80	420	90-110
$MEM(TCNQ)_2$	18	40	106	60-90

Table 3.2: Spin-Peierls critical temperature T_c, J, and spin-phonon coupling α for various spin-Peierls materials (from reference [29]) along with the new values for TiOCl

TiOCl is the first inorganic compound to exhibit a soft-mode spin-Peierls transition, similar to those believed to occur in the organic compounds. We concluded with a comparison of the ratio of the bare phonon frequency to the spin peierls transition temperature, to determine whether the spin-Peierls transition in TiOCl falls into the so-called adiabatic or anti-adiabatic regime, characterized by the presence or absence of phonon softening leading up to the spin Peierls transition. The important ratio is that of the bare phonon frequency to the spin-Peierls transition temperature, which for TiOCl we found is near the cut-off, but on the anti-adiabatic side, meaning no phonon softening is expected. However, a novel theory which considers the effects of inter-chain coupling on the spin-Peierls transition temperature, it was found that low energy modes perpendicular to the chain can facilitate mode softening of the spin-Peierls mode. Taking this into account places TiOCl into the adiabatic regime, which is both a tribute to the new theory and it makes TiOCl an interesting playground for future studies of the phonons associated with the spin-Peierls transition.

Bibliography

[1] Michael Karbach and Gerhard Müller. *cond-mat/9809161*, 1998.

[2] Michael Karbach, Kun Hu, and Gerhard Müller. *cond-mat/9809163*, 1998.

[3] I. A. Zaliznyak, H. Woo, T. G. Perring, C. L. Broholm, C. D. Frost, and H. Takagi. *Phys. Rev. Let.*, 93:087202, 2004.

[4] Alexander Seidel, Chris A. Marianetti, F. C. Chou, Gerbrand Ceder, and Patrick A. Lee. S=1/2 chians and spin-peierls transition in tiocl. *Phys. Rev. B*, 67:020405, 2003.

[5] T. Nakano and H. Fukuyama. Solitons and spin-peierls systems and applications to polyacetylene. *J. Phys. Soc. Jap.*, 49(5):1679, 1980.

[6] W.L. McMillan. Theory of discommensurations and the commensurate-incommensurate charge-density-wave phase transition. *Phys. Rev. B*, 14:1496, 1976.

[7] Young Lee. *Neutron Scattering Study of the Magnetism and Structural Phases of Superconducting* $La_2CuO_{4+\delta}$. PhD thesis, Massachusetts Institute of Technology, 1993.

[8] H. Bethe. Zur theorie der metalle. eigenwerte und eigenfunktionen der linearen atomkette. *Z. Phys.*, 71:205, 1931.

[9] L. Hulthén.

[10] Charles Kittel. *Introduction to Solid State Physics.* John Wiley & Sons, Inc., Hoboken, NJ, seventh edition, 1996.

[11] J. des Cloizeaux and J. J. Pearson. Spin-wave spectrum of the antiferromagnetic linear chain. *Phys. Rev.*, 128:2131, 1962.

[12] R. J. Birgeneau and G. Shirane. *Physics Today*, 31(12):32, 1978.

[13] G. Mueller, H. Thomas, H. Beck, and J. C. Bonner. *Phys. Rev. B*, 24(3):1429, 1981.

[14] A. H. Bougourzi, M. Couture, and M. Kacir. *Phys. Rev. B*, 54(18):R12669, 1996.

[15] C. Gros and R. Werner. Dynamics of the peierls-active phonon modes in cugeo$_3$. *Phys. Rev. B*, 58:R14677, 1999.

[16] D. A. Tennant, T. G. Perring, R. A. Cowley, and S. E. Nagler. *Phys. Rev. B*, 70:4003, 1993.

[17] K. Ishida, Y. Kitoaka, Y. Tokunaga, S. Matsumoto, and K. Asayama. *Phys. Rev. B*, 53:2827, 1996.

[18] D. E. Moncton, R. J. Birgeneau, L. V. Interrante, and F. Wudl. *Phys. Rev. Lett.*, 39:507, 1977.

[19] I. S. Jacobs, J. W. Bray, Jr. H. R. Hart, L. V. Interrante, J. S. Kasper, G. D. Watkins, D. E. Prober, and J. C. Bonner. *Phys. Rev. B*, 14:3036, 1976.

[20] H. M. McConnell and R. Lynden-Bell. b. *J. Chem. Phys.*, (36):2393, 1962.

[21] E. Pytte. Peierls instability in heisenberg chains. *Phys. Rev. B*, 10:4637, 1974.

[22] M. C. Cross and Daniel S. Fisher. A new theory of the spin-peierls transition with special relevance to the experiments on ttfcubdt. *Phys. Rev. B*, 19:402, 1979.

[23] Masashi Hase, Ichiro Terasaki, and Kunimitsu Uchinokura. Observation of the spin-peierls transition in linear cu^{2+} (spin-1/2) chains in an inorganic compound cugeo$_3$. *Phys. Rev. Letters*, 70:3651, 1993.

[24] M. Nishi, O. Fujita, and J. Akimitsu. Neutron-scattering study on the spin-peierls transition in a quasi-one-dimensional magnet cugeo$_3$. *Phys. Rev. B*, 50:6508, 1994.

[25] L. P. Regnault, M. Aïn, B. Hennion, G. Dhalenne, and A. Revcolevschi. Inelastic-neutron-scattering investigation of the spin-peierls system cugeo$_3$. *Phys. Rev. B*, 53:5579, 1996.

[26] K. Hirota, G. Shirane, Q. J. Harris, Q. Feng, R. J. Birgeneau, M. Hase, and K. Uchinokura. Characterization of the structural and magnetic fluctuations near the spin-peierls transition in cuge0$_3$. *Phys. Rev. B*, 52:15412, 1995.

[27] J. E. Lorenzo, K. Hirota, G. Shirane, J. M. Tranquada, M. Hase, K. Uchinokura, H. Kojima, I. Tanaka, and Y. Shibuya. Characterization of the structural and magnetic fluctuations near the spin-peierls transition in cuge0$_3$. *Phys. Rev. B*, 50:1278, 1994.

[28] M. Braden, W. Reichardt, B. Hennion, G. Dhalenne, and A. Revcolevschi. Lattice dynamics of cugeo$_3$: Inelastic neutron scattering and model calculations. *Phys. Rev. B*, 66:214417, 2002.

[29] J. P. Pouget. Microscopic interactions in cugeo$_3$ and organic spin-peierls systems deduced from their pretransitional lattice fluctuations. *Eur. Phys. J. B*, 20:321, 2001.

[30] M. Holicki and H. Fehske. Magnetoelastic excitations in spin-peierls systems. *Phys. Rev. B*, 63:174417, 2001.

[31] R. Citro, E. Orignac, and T. Giamarchi. Adiabatic-antiadiabatic crossover in a spin-peierls chain. *Phys. Rev. B*, 72:024434, 2005.

[32] A. Dobry, D. C. Cabra, and G. L. Rossini. Theory of spin-peierls transition beyond the adiabatic approximation. *Phys. Rev. B*, 75:045122, 2007.

[33] M. Hoinkis, M. Sing, J. Schäfer, M. Klemm, S. Horn, H. Benthien, E. Jeckelmann, T. Saha-Dasgupta, L. Pisani, R. Valenti, and R. Claessen. Electronic structure of the spin-1/2 quantum magnet tiocl. *Phys. Rev. B*, 72:125127, 2005.

[34] J. C. Bonner and M. E. Fisher. b. *Phys. Rev.*, 135:A640, 1967.

[35] Jens Als-Nielsen and Des McMorrow. *Elements of Modern X-ray Physics.* John Wiley & Sons Ltd., West Sussex, England, 1 edition, 2001.

[36] David J. Griffiths. *Introduction to Electrodynamics.* Simon & Schuster Company, Upper Saddle River, NJ, 2 edition, 1989.

[37] http://www.nsls.bnl.gov/organization/accelerator/xray.htm.

[38] Aps insertion devices. http://www.aps.anl.gov/About/APS_Overview/Insertion_Devices/.

[39] Kwange-Je Kim. Characteristics of synchrotron radiation. In *AIP Conference Proceedings*, volume 184, pages 565–632. American Institute of Physics, 1989.

[40] W.R. Busing and H.A. Levy. *Acta Crystallography*, 22:457, 1967.

[41] N. Ashcroft and D. Mermin. *Solid State Physics.* Saunders College Publishing, 1 edition, 1976.

[42] D. Cromer and J. Mann. *Acta Crystallography A*, 24:321, 1968.

[43] B.E. Warren. *X-ray Diffraction.* General Publishing Company, Ltd., Toronto, Ontario, second edition, 1990.

[44] H. Sinn, E. E. Alp, A. Alatas, J. Barraza, G. Bortel, E. Burkel, D. Shu, W. Sturhahn, J.P. Sutter, T.S. Toellner, and J. Zhao. An inelastic x-ray spectrometer wiht 2.2 mev energy resolution. *Nuclear Instruments and Methods in Physics Research A*, 467:1545, 2001.

[45] T. M. Mooney, T. Toellner, W. Sturhahn, E. E. Alp, and S. D. Shastri. High resolution large-angular-acceptance monochrometer for hard x-rays. *Nuclear Instruments and Methods in Physics Research A*, 347:348, 1994.

[46] W. G. Jenks, I. M. Thomas, and Jr. J. P. Wikswo. Squids. In *Encyclopedia of Applied Physics*, volume 19, pages 457–468. VCH Publishers, Inc., 1997.

[47] *PPMS, Hardware and Options Manual.*

[48] H. Schäfer, F. Wartenpfurl, and E. Weise. *Z. Anorg. Alleg. Chem.*, 295:268, 1958.

[49] H. He, P. Bourges, Y. Sidis, C. Ulrich, L. P. Regnault, S. Pailhés, N. S. Berzigiarova, N. N. Kolesnikov, and B. Keimer. Magnetic resonance mode in the single-layer hightemperature superconductor $tl_2ba_2cuo_{6+\delta}$. *Science*, 295:1045, 2002.

[50] R. J. J. Visser, S. Oostra, C. Vettier, and J. Voiron. Determination of the spin-peierls distortion in n-methyl-n-ethyl-morphonlinium ditetracyanoquinodimethanide [mem(tcnq)$_2$]: Neurton diffraction study at 6 k. *Phys. Rev. B*, 28:2074, 1983.

[51] D. C. Johnston, R. K. Kremer, M. Troyer, X. Wang, and A. Kl umper. Thermodynamics of spin s=1/2 antiferromagnetic uniform and alternating-exchange heisenberg chains. *Phys. Rev. B*, 61:9558, 2000.

[52] Eric Weisstein. Wolfram math world : Square wave. World Wide Web http://mathworld.wolfram.com/SquareWave.html, March 4 2007.

[53] M. Fujita and K. Machida. Spin-peierls transitions in magnetic fields - thermodynamic properties of a soliton lattice state. *J. Phys. Soc. Jap.*, 53(12):4395, 1984.

[54] V. Kiryukhin, B. Keimer, J. P. Hill, and A. Vigliante. Soliton lattice in pure and diluted $cugeo_3$. *Phys. Rev. Let.*, 76:4608, 1996.

[55] W. P. Su, J. R. Schrieffer, and A. J. Heeger. *Phys. Rev. Lett.*, 42:1698, 1979.

[56] V. Kiryukhin, B. Keimer, and D. E. Moncton. *Phys. Rev. Lett.*, 42:1669, 1995.

[57] B. Horowitz. Soliton lattice in polyacetylene, spin-peierls systems and two-dimensional sine-gordon systems. *Phys. Rev. Lett.*, 46:742, 1981.

[58] Eric Weisstein. Wolfram math world : Jacobi elliptic functions. World Wide Web http://mathworld.wolfram.com/JacobiEllipticFunctions.html, March 4 2007.

[59] No Author. Wikipedia: Jacobi's elliptic functions. World Wide Web http://en.wikipedia.org/wiki/Jacobi's_elliptic_functions, March 15 2007.

[60] M. Shaz, S. v. Smaalen, L. Palatinus, M. Hoinkis, M. Klemm, S. Horn, and R. Claessen. Spin-peierls transition in tiocl. *Phys. Rev. B*, 71:100405, 2005.

[61] R. J. Christianson, Y. J. Wang, S. C. LaMarra, R. J. Birgeneau, V. Kiryiukhin, T. Masuda, I. Tsukada, K. Uchinokura, and B. Keimer. X-ray study of the incommensurate phase in mg-doped cugeo$_3$. *Phys. Rev. B*, 66:174105, 2002.

[62] T. Imai and F. C. Chou. Novel spin-gap behavior in layered s=1/2 quantum spin system tiocl. *cond-mat/0301425*, 2003.

[63] Eric J. Wu. *Applications of lattice dynamics theory: Calculating vibrational entropy in alloys and dielectric losses in ceramics.* PhD thesis, Massachusetts Institute of Technology, 2002.

[64] Axel van de Walle. *The effect of Lattice Vibrations of Substitutional Alloy Thermodynamics.* PhD thesis, Massachusetts Institute of Technology, 2000.

[65] S. Baroni, S. de Gironcoli, and A. D. Corso. *Rev. Mod. Phys.*, 73:515, 2001.

[66] J. D. Gale and A. L. Rohl. *Mol. Simul.*, 29:291, 2003.

[67] J. D. Gale. *J. Chem. Soc. Faraday Trans.*, 93(4):629, 1997.

[68] G. V. Lewis and C. R. A. Catlow. *J. Phys. C*, 18:1149, 1985.

[69] J. Gale and A.L. Rhol. General utility lattice program. http://www.ivec.org/GULP/.

[70] P. Hohenberg and W. Kohn. *Phys. Rev.*, 136:B864, 1964.

[71] R. G. Parr and W. Yang. *Density Functional Theory of Atoms and Molecules.* Oxford University Press, New York, 1989.

[72] R. M. Dreizler and E. K. U. Gross. Density functional theory.

[73] S. de Gironcoli P. Giannozzi S. Baroni, A. Dal Corso. Plane wave self consistent field.

[74] P. Giannozzi and S. Baroni. Density-functional perturbation theory. In S. Yip, editor, *Handbook of Materials Modeling.* Springer, 2005.

[75] G. Shirane, S.M. Shapiro, and J. M. Tranquada. *Neutron Scattering with a Triple-Axis Spectrometer.* Cambridge University Press, Cambridge, UK, 2002.

[76] G. Shirane, J. D. Axe, and J. Harada. Inelastic neutron scattering from single domain batio$_3$. *Phys. Rev. B*, 2:3651, 1976.

[77] S. M. Shapiro, J. D. Axe, and C. Shirane. Critical neutron scattering in srtio$_3$ adn kmnf$_3$. *Phys. Rev. B*, 6:4332, 1972.

[78] G. Shirane. Neutron scattering studies of structural phase transistions at brookhaven. *Reviews of Modern Physics*, 46:437, 1974.

[79] P. Ghaemi. Private communication.

[80] P. Lemmens, K. Y. Choi, G. Caimi, L. Degiorgi, N. N. Kovaleva, A. Seidel, and F. C. Chou. Giant phonon anomalies in the pseudo-gap phase of tiocl. *cond-mat/0307502*, 2003.

[81] G. Caimi. Infrared optical properties of the spin-1/2 quantum magnet tiocl. *Phys. Rev. B*, 69:125108, 2004.

[82] E. Orignac and R. Chitra. Mean field theory of the spin-peierls transition. *Phys. Rev. B*, 70:214436, 2004.